Computer Methods in Applied Mechanics and Engineering 461 (2026) 119218

Contents lists available at ScienceDirect

Comput. Methods Appl. Mech. Engrg.

journal homepage: www.elsevier.com/locate/cma

A stochastic finite-strain crystal plasticity model with continuum dislocation dynamics

Sing-Huei Lee [a,b,*], Adrian Asmund Fessler [a], Katrin Schulz [a,b,*]

[a] Karlsruhe Institute of Technology (KIT), Institute for Applied Materials (IAM), Karlsruhe, Germany
[b] Karlsruhe University of Applied Sciences (HKA), Karlsruhe, Germany

ARTICLE INFO

Dataset link: https://gitlab.kit.edu/kit/mpp

Keywords:
Continuum dislocation dynamics
Crystal plasticity
Finite deformation
Polycrystals
Stochastic microstructures

ABSTRACT

A stochastic finite-deformation continuum dislocation dynamics–crystal plasticity (CDD–CP) framework is developed for simulating the coupled evolution of dislocation microstructures and macroscopic mechanical response in heterogeneous crystalline materials. The formulation couples finite-strain crystal plasticity with higher-dimensional CDD transport equations for total dislocation density, geometrically necessary dislocation density, and curvature density, with stochastic initial dislocation fields, source distributions, grain morphologies, and crystallographic orientations as inputs. A consistent algorithmic tangent enables robust Newton-based solution under strongly heterogeneous stochastic fields, and the CDD equations are discretized by a nodal discontinuous Galerkin method with diagonally implicit Runge–Kutta time integration.

The framework is assessed in single-slip simple shear, single-crystal tension, and polycrystalline tension, and compared with a small-deformation CDD–CP formulation. Single-slip simulations capture three distinct regimes governed by the competition between dislocation multiplication and boundary escape. The Frank–Read source term acts as a continuum simplification for physical multiplication, admitting natural extensions to annihilation, cross-slip, and junction reactions within the same mathematical structure. In single crystals, finite-deformation effects are modest macroscopically but drive additional slip-system activation through lattice rotation. In polycrystals, grain-boundary constraints cause the two formulations to diverge immediately at the onset of plastic flow, providing a first quantitative assessment of this difference in a transport-based CDD–CP setting. The exponential-map plastic update outperforms backward-Euler in robustness under the chosen time-stepping strategy. An ensemble of 64 stochastic polycrystalline simulations demonstrates measurable realization-to-realization variability in both macroscopic response and dislocation microstructure, constituting a first step toward uncertainty-aware dislocation-based crystal plasticity.

1. Introduction

Crystalline materials develop pronounced microstructural heterogeneity across multiple length scales. At the micro-scale, dislocations organize into cells and walls [1–3], and at larger scales, polycrystalline aggregates consist of grains with different geometries and crystallographic orientations [4]. These microstructural features govern slip activation, lattice rotation, and kinematic incompatibilities at grain interfaces, and must therefore be accounted for in predictive models of plastic deformation.

* Corresponding authors.
E-mail addresses: sing-huei.lee@kit.edu (S.-H. Lee), katrin.schulz@kit.edu (K. Schulz).

https://doi.org/10.1016/j.cma.2026.119218
Received 2 April 2026; Received in revised form 5 June 2026; Accepted 30 June 2026
Available online 10 July 2026

Discrete simulation methods, such as molecular dynamics and discrete dislocation dynamics, resolve dislocation interactions with high fidelity [5–7], but their computational cost restricts them to limited spatial and temporal scales and makes large statistical studies difficult. Continuum crystal plasticity (CP) provides a tractable alternative and has become the standard framework for modeling anisotropic plastic deformation in crystalline solids [8–11]. Dislocation-density-based CP formulations describe hardening through local evolution laws, for example in the spirit of the Kocks–Mecking model [12], using statistically stored and geometrically necessary dislocation (GND) densities [13–15], enabling large-scale simulations of polycrystalline aggregates. However, in these models dislocation densities enter only as local internal variables, evolving independently of the microstructural state at neighboring material points. As a direct consequence, such models lack an intrinsic length scale and cannot reproduce phenomena governed by nonlocal dislocation interactions, including pile-up at grain boundaries, size-dependent strengthening, and the emergence of heterogeneous dislocation structures [16]. Furthermore, dislocation multiplication is typically treated in a slip-system-wise phenomenological manner, which cannot capture the cross-slip and glissile junction reactions that couple slip systems and drive density increase on otherwise inactive systems [17]. Their spatial redistribution is represented, at best, through phenomenological gradient terms, and the kinematics of dislocation transport are not resolved explicitly.

Beyond phenomenological hardening laws, a physically grounded continuum representation of dislocations can be built on the dislocation-density tensor introduced by Nye and Kröner [18,19]. Transport-based continuum models were subsequently developed in several directions. Field dislocation mechanics and mesoscale field dislocation mechanics, developed by Acharya and co-workers, use the Nye tensor or excess dislocation density as a central state variable and couple its transport to the mechanical fields [20–22]. Their formulations provide a strong mechanical treatment of incompatibility, internal stress, and finite deformation, and have demonstrated pattern formation, size effects, and orientation effects. Evaluating the total dislocation density within this framework requires closure assumptions for the statistically stored dislocation content, which is not fully represented by the Nye tensor alone [22]. Other transport-based theories use scalar or vector-valued dislocation-density variables. Statistical continuum dislocation models by Groma, Zaiser, and co-workers describe the kinetic evolution of dislocation densities and their correlations in reduced settings [23–25]. El-Azab and co-workers further developed scalar-density and vector-density formulations, including slip-system-based transport models and finite-deformation implementations [26–28]. In parallel, Hochrainer and co-workers developed higher-dimensional, orientation-resolved continuum dislocation dynamics (CDD), in which the dislocation state on each slip system is described by the total dislocation density, the geometrically necessary dislocation density vector, and the curvature density, all evolved through coupled hyperbolic transport equations derived from the kinematics of moving dislocation lines [29–32]. This framework provides a systematic reduction of the full orientation-dependent dislocation distribution to its leading-order moments, enabling physically consistent descriptions of loop expansion, GND accumulation, and curvature-driven multiplication [33]. Beyond these transport-based CDD approaches, several coupled frameworks have further integrated dislocation transport directly into crystal plasticity finite-element formulations. Reuber and co-workers introduced an advection term for the dislocation density evolution within the DAMASK platform, rendering the constitutive model nonlocal and enabling quantitative predictions of dislocation redistribution around stress concentrators [34]. Luscher and co-workers coupled continuum dislocation transport with nonlinear thermoelasticity and crystal plasticity for application to shock loading conditions, demonstrating the role of dislocation pile-up and transport under extreme dynamic loading [16].

The present work follows the higher-dimensional CDD framework. In this setting, the dislocation-density and curvature fields satisfy hyperbolic transport equations on the slip systems, while the macroscopic mechanical response is obtained from an elliptic force-balance problem. The resulting CDD–CP formulation can represent dislocation fluxes, pile-ups, and transport-driven heterogeneous dislocation-density patterns that lie beyond the scope of local dislocation-density CP models. Several coupled CDD–CP frameworks have been proposed previously [35–37], establishing the theoretical basis of the coupled approach. However, existing demonstrations have largely been limited to simplified settings, such as single-slip configurations, two-dimensional geometries, or single crystals subjected to prescribed stochastic external stress fields. Large-scale simulations of stochastic polycrystalline microstructures, in which dislocation transport interacts with spatially varying lattice orientation, grain-boundary constraints, heterogeneous slip activity, and stochastic initial dislocation distributions and source arrangements, are still lacking.

In this work, we develop a stochastic finite-deformation CDD–CP framework for finite-element simulations of heterogeneous crystalline microstructures with randomly distributed initial dislocation densities, dislocation sources, grain morphologies, and crystallographic orientations. The formulation resolves dislocation transport in stochastic polycrystals while consistently accounting for finite kinematics and lattice rotation. For the macroscopic force-balance problem, a consistent algorithmic tangent is derived for the finite-strain equilibrium equations, enabling robust Newton-based solution with a continuous Galerkin finite-element discretization. The CDD transport equations are discretized by a high-order nodal discontinuous Galerkin method in strong form and integrated in time by a diagonally implicit Runge–Kutta scheme, which alleviates the Courant–Friedrichs–Lewy time-step restriction associated with explicit methods while preserving second-order accuracy. Both solvers are implemented within the `MPI`-parallel finite-element library `M++` [38,39], which provides scalable solvers for elliptic and hyperbolic problems alongside algorithmic infrastructure for large-scale full-field uncertainty quantification, including multilevel Monte Carlo and stochastic gradient descent methods [40–43]. The present ensemble study therefore serves as a natural first step toward applying these uncertainty quantification methodologies to dislocation-based crystal-plasticity simulations with uncertain microstructure and material parameters. In addition, we systematically compare the finite-deformation formulation with the small-deformation CDD–CP formulation of [36] in single-slip, single-crystal, and polycrystalline simulations to assess the role of finite kinematics in dislocation-driven plasticity.

The main contributions of this work are as follows. We first formulate and implement a finite-deformation CDD–CP framework that couples finite-strain mechanical equilibrium with slip-system-wise CDD transport in stochastic heterogeneous microstructures. We then use single-slip, single-crystal, and polycrystalline simulations to show how stochastic source activity, lattice rotation, and

grain-boundary constraints control the differences between small- and finite-deformation CDD–CP responses. We further assess the robustness of local plastic updates, showing the practical advantage of the exponential-map update for the present time-stepping strategy. Finally, we demonstrate polycrystalline ensemble simulations, establishing a basis for future uncertainty-aware studies of stochastic dislocation-based plasticity.

2. Methodology

The mathematical model and numerical solution procedure are organized as follows. In Section 2.1, we introduce the governing equations of the finite-strain elasto-viscoplastic model coupled with CDD, including the plastic flow rule, the dislocation source term, and the two local time-integration schemes for the plastic deformation gradient. The numerical discretization of the macroscopic elliptic force-balance problem by a continuous Galerkin (CG) finite-element method and its Newton solution strategy are described in Section 2.2. The derivation of the consistent algorithmic tangent operator, required for the Newton-based solution of the macroscopic force-balance problem, is detailed in Appendix A. The discretization of the microscopic hyperbolic CDD transport equations by a nodal discontinuous Galerkin (DG) method and their time integration by a diagonally implicit Runge–Kutta scheme are presented in Section 2.3. Finally, Section 2.4 summarizes the overall computational structure of the coupled CDD–CP simulation and the sequential coupling strategy between the two subproblems.

2.1. Finite-deformation Elasto-Viscoplastic CDD–CP model

We consider a bounded polyhedral reference domain $V_0 \subset \mathbb{R}^3$ in the reference configuration. Its boundary ∂V_0 is decomposed into a displacement (Dirichlet) part $\Gamma_d \subset \partial V_0$ and a traction (Neumann) part $\Gamma_t \subset \partial V_0$, such that $\Gamma_d \cup \Gamma_t = \partial V_0$ and $\Gamma_d \cap \Gamma_t = \emptyset$. Let $\mathbf{n} \in \mathbb{R}^3$ denote the outward unit normal on Γ_t. The strong form of force equilibrium reads as an elliptic PDE

$$\mathrm{Div}_0\, \mathbf{P}(\mathbf{F}(\mathbf{u})) + \mathbf{b}_0 = \mathbf{0} \quad \text{in } V_0, \qquad \mathbf{P}(\mathbf{F}(\mathbf{u}))\,\mathbf{n} = \mathbf{t}_0 \quad \text{on } \Gamma_t, \quad \text{and} \quad \mathbf{u} = \bar{\mathbf{u}} \quad \text{on } \Gamma_d, \tag{1}$$

where $\mathbf{P} : V_0 \to \mathbb{R}^{3\times3}$ denotes the first Piola–Kirchhoff stress tensor, $\mathbf{b}_0 : V_0 \to \mathbb{R}^3$ is the body force per unit reference volume, $\mathbf{t}_0 : \Gamma_t \to \mathbb{R}^3$ is the prescribed traction, and $\bar{\mathbf{u}} : \Gamma_d \to \mathbb{R}^3$ is the prescribed displacement. The deformation gradient $\mathbf{F} : V_0 \to \mathbb{R}^{3\times3}$ is given by $\mathbf{F} = \mathbf{I} + \nabla_0 \mathbf{u}$, where $\mathbf{I}$ is the second-order identity tensor and $\nabla_0(\cdot)$ denotes the reference gradient (see, e.g., [44, Ch. 4]).

We employ the multiplicative decomposition of the deformation gradient in the finite-strain elastoplasticity framework [45],

$$\mathbf{F} = \mathbf{F}_e \mathbf{F}_p,$$

where $\mathbf{F}_e, \mathbf{F}_p : V_0 \times (0,T] \to \mathbb{R}^{3\times3}$ denote the elastic and plastic parts of the deformation gradient, respectively. All stress, strain, and internal-variable fields introduced in the following depend on both position $\mathbf{X} \in V_0$ and time $t \in (0,T]$, where $\mathbf{X}$ denotes the position of reference frame. For brevity, these arguments are suppressed throughout. Following the derivation in [46, Eq. (3.47)], the first Piola–Kirchhoff stress is defined as

$$\mathbf{P}(\mathbf{F}(\mathbf{u})) = \mathbf{F}_e(\mathbf{u})\,\mathbf{S}_e(\mathbf{u})\,\mathbf{F}_p(\mathbf{u})^{-\mathsf{T}}, \tag{2}$$

where $\mathbf{S}_e : V_0 \to \mathbb{R}^{3\times3}$ is the elastic second Piola–Kirchhoff stress.

The constitutive law for $\mathbf{S}_e$, expressed in terms of the elastic Green–Lagrange strain $\mathbf{E}_e : V_0 \to \mathbb{R}^{3\times3}$, is [47, Ch. 5.3.1]

$$\mathbf{S}_e = \mathbb{C} : \mathbf{E}_e, \quad \text{with} \quad \mathbf{E}_e = \tfrac{1}{2}(\mathbf{F}_e^{\mathsf{T}}\mathbf{F}_e - \mathbf{I}), \tag{3}$$

where $\mathbb{C} : V_0 \times (0,T] \to \mathbb{R}^{3\times3\times3\times3}$ is the fourth-order elasticity tensor in the sample frame, which is in general time-dependent due to the evolving lattice rotation, and $:$ denotes the standard double contraction. Hence, $\mathbf{P}$ depends on $\mathbf{F}$ and $\mathbf{F}_p$ through $\mathbf{F}_e = \mathbf{F}\mathbf{F}_p^{-1}$ and on $\mathbb{C}$ through the elastic law Eq. (3).

For cubic anisotropy, the reference elasticity tensor $\mathbb{C}_0$, expressed in the unrotated crystal lattice frame, is given by

$$(\mathbb{C}_0)_{ijkl} = \begin{cases} C_{11}, & i=j=k=l, \\ C_{12}, & i=j\neq k=l, \\ C_{44}, & i=k\neq j=l \text{ or } i=l\neq j=k, \\ 0, & \text{otherwise}, \end{cases}$$

using standard Voigt-symmetric index notation. Here, C_{11}, C_{12}, and C_{44} are the independent elastic constants of the cubic crystal [48].

For the isotropic benchmark simulations, we use the corresponding isotropic elasticity tensor

$$(\mathbb{C}_0)_{ijkl} = \lambda\,\delta_{ij}\delta_{kl} + \mu\left(\delta_{ik}\delta_{jl} + \delta_{il}\delta_{jk}\right),$$

where λ and μ are the Lamé parameters computed from the prescribed Young's modulus E and Poisson's ratio ν [44, Eq. 2.262]. Since $\mathbb{C}_0$ is rotation-invariant in the isotropic case, no orientation-dependent stiffness rotation is applied and $\mathbb{C} = \mathbb{C}_0$ throughout.

For simulations with cubic anisotropy, the initial lattice-to-sample orientation is described by a crystal rotation field $\mathbf{R}_0 : V_0 \to \mathrm{SO}(3)$, where SO(3) denotes the group of proper orthogonal 3×3 rotation matrices. In the present discretization, $\mathbf{R}_0$ is piecewise constant on each grain, and is therefore constant over all finite elements in the same grain. It is parameterized by the Tait–Bryan Euler angles $\boldsymbol{\xi} = (\theta, \phi, \omega)$ through

$$\mathbf{R}_0(\boldsymbol{\xi}) = \mathbf{R}_z(\omega)\,\mathbf{R}_y(\phi)\,\mathbf{R}_x(\theta), \tag{4}$$

where $\mathbf{R}_x$, $\mathbf{R}_y$, and $\mathbf{R}_z$ are given by

$$\mathbf{R}_x(\theta)=\begin{bmatrix}1 & 0 & 0\\ 0 & \cos\theta & -\sin\theta\\ 0 & \sin\theta & \cos\theta\end{bmatrix},\quad \mathbf{R}_y(\phi)=\begin{bmatrix}\cos\phi & 0 & \sin\phi\\ 0 & 1 & 0\\ -\sin\phi & 0 & \cos\phi\end{bmatrix},\quad \mathbf{R}_z(\omega)=\begin{bmatrix}\cos\omega & -\sin\omega & 0\\ \sin\omega & \cos\omega & 0\\ 0 & 0 & 1\end{bmatrix}.$$

We take $\theta,\omega\in[0,2\pi)$ and $\phi\in(-\frac{\pi}{2},\frac{\pi}{2})$ to avoid the gimbal singularity, cf. [49, Ch. 5.8] and [50, Eq. (17.110)]. These angles define the initial crystallographic orientation.

During loading, the lattice undergoes an additional elastic rotation. We extract the elastic lattice rotation field $\mathbf{Q}: V_0\to \mathrm{SO}(3)$, which is likewise treated as piecewise constant on each element, from the polar decomposition of the elastic deformation gradient, see [51, Sec. 3.1.6],

$$\mathbf{F}_\mathrm{e}=\mathbf{Q}\,\mathbf{U},\qquad \text{with}\qquad \mathbf{Q}^\top\mathbf{Q}=\mathbf{I},\ \ \mathbf{U}=\mathbf{U}^\top\succ 0, \tag{5}$$

where $\mathbf{U}: V_0\to\mathbb{R}^{3\times3}$ is the right stretch tensor. The current lattice-to-sample rotation is then defined by

$$\mathbf{R}_t=\mathbf{Q}\,\mathbf{R}_0,$$

where $\mathbf{R}_t$ captures both the initial crystallographic orientation $\mathbf{R}_0$ and the elastic lattice rotation $\mathbf{Q}$ accumulated during loading. Since $\mathbf{Q}$ evolves with deformation, $\mathbf{R}_t$ is time-dependent, and the sample-frame elasticity tensor $\mathbb{C}$ is obtained from $\mathbb{C}_0$ by

$$\mathbb{C}_{ijkl}=R_{t,ip}\,R_{t,jq}\,R_{t,kr}\,R_{t,ls}\,(\mathbb{C}_0)_{pqrs}, \tag{6}$$

which replaces the earlier generic $\mathbb{C}$ in Eq. (3). Equivalently, Eq. (3) may be written explicitly as

$$\mathbf{S}_\mathrm{e}=\mathbf{R}_t\Big[\mathbb{C}_0:\big(\mathbf{R}_t^\top\mathbf{E}_\mathrm{e}\,\mathbf{R}_t\big)\Big]\mathbf{R}_t^\top.$$

Thus, the constitutive response accounts for both the initial crystallographic orientation and the deformation-induced lattice rotation.

For evaluating the stress–strain response, we employ the Cauchy stress $\boldsymbol{\sigma}: V_0\to\mathbb{R}^{3\times3}$ and the total logarithmic strain $\boldsymbol{\varepsilon}_{\log}: V_0\to\mathbb{R}^{3\times3}$. The Cauchy stress is expressed in terms of the elastic deformation gradient $\mathbf{F}_\mathrm{e}$ as

$$\boldsymbol{\sigma}=\frac{1}{J_\mathrm{e}}\mathbf{F}_\mathrm{e}\,\mathbf{S}_\mathrm{e}\,\mathbf{F}_\mathrm{e}^\top,$$

where $J_\mathrm{e}=\det(\mathbf{F}_\mathrm{e})$. The total logarithmic strain is defined as

$$\boldsymbol{\varepsilon}_{\log}=\tfrac{1}{2}\ln(\mathbf{C}),\qquad \mathbf{C}=\mathbf{F}^\top\mathbf{F},$$

with $\mathbf{C}: V_0\to\mathbb{R}^{3\times3}$ the right Cauchy–Green tensor.

We model the evolution of the plastic deformation gradient $\mathbf{F}_\mathrm{p}$ by coupling it to dislocation kinematics obtained from solving a CDD problem, following the higher-dimensional CDD transport equations introduced by [30,31].

Let $S'\in\mathbb{N}$ denote the number of slip systems, and for each $s\in\{1,\dots,S'\}$ let $\mathbf{b}^s: V_0\to\mathbb{R}^3$ be the Burgers vector with magnitude $b^s:=\|\mathbf{b}^s\|$ and unit slip direction $\mathbf{d}_0^s:=\mathbf{b}^s/b^s$. Together with the slip-plane normal $\mathbf{m}_0^s$, we form the orthonormal reference slip-system triad $\{\mathbf{d}_0^s,\mathbf{l}_0^s,\mathbf{m}_0^s\}$, where $\mathbf{l}_0^s:=\mathbf{m}_0^s\times\mathbf{d}_0^s$ is the in-plane edge line direction in the reference configuration. During deformation, the lattice undergoes an elastic rotation $\mathbf{Q}$ (see Eq. (5)), and the slip-system basis rotates accordingly to its current configuration,

$$\mathbf{d}_t^s=\mathbf{R}_t\,\mathbf{d}_0^s,\qquad \mathbf{m}_t^s=\mathbf{R}_t\,\mathbf{m}_0^s,\qquad \mathbf{l}_t^s=\mathbf{R}_t\,\mathbf{l}_0^s.$$

We note that $\{\mathbf{d}_0^s,\mathbf{l}_0^s,\mathbf{m}_0^s\}$ and $\{\mathbf{d}_t^s,\mathbf{l}_t^s,\mathbf{m}_t^s\}$ are fixed bases that define the slip-system geometry, and they should not be confused with the local line direction of a general dislocation segment, which is orientation-dependent in the higher-dimensional CDD description [31, Eq. (12)]. The Schmid tensor in the current configuration is then

$$\mathbf{M}_t^s:=\mathbf{d}_t^s\otimes\mathbf{m}_t^s=\mathbf{R}_t\,\mathbf{M}_0^s\,\mathbf{R}_t^\top,\quad \text{with}\quad \mathbf{M}_0^s:=\mathbf{d}_0^s\otimes\mathbf{m}_0^s.$$

Under the multiplicative decomposition, the plastic deformation gradient evolves according to the plastic velocity gradient $\mathbf{L}_\mathrm{p}: V_0\to\mathbb{R}^{3\times3}$. Then

$$\dot{\mathbf{F}}_\mathrm{p}=\mathbf{L}_\mathrm{p}\,\mathbf{F}_\mathrm{p},\qquad \mathbf{L}_\mathrm{p}=\sum_{s=1}^{S'}\dot\gamma^s\,\mathbf{M}_t^s,$$

where $\dot\gamma^s: V_0\to\mathbb{R}$ is the slip rate on slip system s. The slip rate is related to dislocation kinematics via Orowan's relation,

$$\dot\gamma^s=v^s\,b^s\,\rho^s, \tag{7}$$

where $v^s: V_0\to\mathbb{R}$ is the (signed) glide velocity and $\rho^s: V_0\to\mathbb{R}$ is the total dislocation line length per unit volume on slip system s. To compute ρ^s and v^s, we introduce the CDD state variables and the dislocation velocity law.

In the higher-dimensional CDD formulation [30,31], the dislocation state on each slip system s is described by three reduced fields, namely the total dislocation density ρ^s, the GND density vector $\boldsymbol{\kappa}^s: V_0\to\mathbb{R}^3$ with $\|\boldsymbol{\kappa}^s\|\le\rho^s$, and the curvature density $q^s: V_0\to\mathbb{R}$. Here ρ^s is the zeroth orientation moment of the underlying dislocation line distribution, $\boldsymbol{\kappa}^s$ is its first moment and measures the net signed excess of dislocation line directions whose Burgers content does not cancel inside the averaging volume, and q^s is the orientation-averaged curvature density that enters the density evolution as a line-length production term.

The remaining dislocation content, which contributes to density and hardening but carries no net Burgers vector, is the statistically stored dislocation (SSD) density,

$$\rho^s_{\mathrm{SSD}} := \rho^s - \|\boldsymbol{\kappa}^s\|.$$

To separate screw and edge contributions to the GND content, the GND vector is decomposed into components along the current slip-system basis,

$$\boldsymbol{\kappa}^s = \kappa^s_{\mathrm{screw}}\,\mathbf{d}^s_t + \kappa^s_{\mathrm{edge}}\,\mathbf{l}^s_t,$$

where $\kappa^s_{\mathrm{screw}}$ and κ^s_{edge} denote the net signed screw and edge excess densities, respectively. This decomposition does not restrict the model to pure screw and edge segments, as curved and mixed-character dislocations are represented through the underlying line-orientation distribution and its reduced alignment-tensor moments. For further detail, see [32].

The dislocation glide velocity is modeled as overdamped (linear-viscous) glide [52],

$$v^s = \frac{b^s}{B}\left\langle |\tau^s| - \tau^s_{\mathrm{y}}\right\rangle \mathrm{sign}(\tau^s), \tag{8}$$

where B is the drag coefficient and $\langle x\rangle = \max(x, 0)$. The resolved shear stress

$$\tau^s = \tau^s_{\mathrm{ext}} + \tau^s_{\mathrm{int}} \tag{9}$$

consists of an external part given by the Schmid projection,

$$\tau^s_{\mathrm{ext}} = \mathbf{S}_{\mathrm{e}} : \mathbf{M}^s_t \quad (\text{equivalently } \mathbf{S}_{\mathrm{e}} : \mathrm{sym}(\mathbf{M}^s_t),\ \text{since } \mathbf{S}_{\mathrm{e}} \text{ is symmetric}),$$

and an internal part τ^s_{int} collecting long-range mean-field and short-range back stresses [53–55]. The slip resistance follows Taylor hardening [56],

$$\tau^s_{\mathrm{y}} = a\,\mu\,b^s\,\sqrt{\rho^s}, \tag{10}$$

where a is a material parameter and μ is the shear modulus.

The evolution of the dislocation state $(\rho^s, \boldsymbol{\kappa}^s, q^s)$ is governed by the CDD system derived in [30,31], which takes the form of a coupled system of hyperbolic transport PDEs,

$$\partial_t \rho^s = -\nabla\cdot\left(v^s \boldsymbol{\kappa}^s_{\perp}\right) + v^s q^s, \tag{11a}$$

$$\partial_t \boldsymbol{\kappa}^s = \nabla\times\left(\rho^s v^s \mathbf{m}^s_t\right), \tag{11b}$$

$$\partial_t q^s = -\nabla\cdot\left(\frac{q^s}{\rho^s}\,\boldsymbol{\kappa}^s_{\perp}\,v^s + \mathbf{A}^s\nabla v^s\right) + \partial_t q^s_{\mathrm{FR}}, \tag{11c}$$

where $\boldsymbol{\kappa}^s_{\perp} = \boldsymbol{\kappa}^s \times \mathbf{m}^s_t$. The second-order alignment tensor $\mathbf{A}^s$ is taken from the simplified form derived in [36,57],

$$\mathbf{A}^s = \frac{1}{2\|\boldsymbol{\kappa}^s\|^2}\left((\rho^s + \|\boldsymbol{\kappa}^s\|)\,\boldsymbol{\kappa}^s\otimes\boldsymbol{\kappa}^s + (\rho^s - \|\boldsymbol{\kappa}^s\|)\,\boldsymbol{\kappa}^s_{\perp}\otimes\boldsymbol{\kappa}^s_{\perp}\right),$$

regularized for $\|\boldsymbol{\kappa}^s\| \approx 0$ to avoid division by zero. The source term $\partial_t q^s_{\mathrm{FR}}$ accounts for loop generation by Frank–Read (FR) nucleation [33,58,59].

Following [33, Eq. (40)], the FR nucleation contribution to the curvature-density production rate is

$$\partial_t q^s_{\mathrm{FR}} = 2\pi\, n^s_{\mathrm{FR}}\, f^s_{\mathrm{FR}}. \tag{12}$$

Here $n^s_{\mathrm{FR}} : V_0 \to \mathbb{R}$ denotes the volumetric density of FR sources and $f^s_{\mathrm{FR}} : V_0 \to \mathbb{R}$ is the loop emission frequency. The emission frequency is obtained from the nucleation time $t^s_{\mathrm{FR}} : V_0 \to \mathbb{R}$,

$$f^s_{\mathrm{FR}} = \frac{1}{t^s_{\mathrm{FR}}}, \qquad t^s_{\mathrm{FR}} = c_{\mathrm{FR}}\,\frac{l^s_{\mathrm{FR}}}{2\,v^s_{\mathrm{FR}}}, \tag{13}$$

where c_{FR} is a dimensionless constant [33]. Consistent with Eq. (8), the characteristic bow-out speed $v^s_{\mathrm{FR}} : V_0 \to \mathbb{R}$ is modeled as

$$v^s_{\mathrm{FR}} = \frac{b^s}{B}\left\langle |\tau^s| - \tau^s_{\mathrm{y}} - \tau^s_{\mathrm{FR}}\right\rangle,$$

where τ^s_{FR} is an additional activation threshold for source operation. Using an averaged line-tension approximation [58], we take

$$\tau^s_{\mathrm{FR}} = \frac{0.5\,\mu\,(b^s)^2}{b^s l^s_{\mathrm{FR}}}.$$

Combining Eqs. (12) and (13) yields

$$\partial_t q^s_{\mathrm{FR}} = \frac{4\pi}{c_{\mathrm{FR}}}\,n^s_{\mathrm{FR}}\,\frac{v^s_{\mathrm{FR}}}{l^s_{\mathrm{FR}}}.$$

We prescribe $l^s_{\mathrm{FR}} = l_{\mathrm{FR}}$ as a constant for all slip systems for the estimation of the activation stress and initialize n^s_{FR} as a spatially random field drawn from a uniform distribution, held fixed in time. The FR source term $\partial_t q^s_{\mathrm{FR}}$ is the only explicit source

mechanism included in the present implementation, retained here to examine how the amount and spatial distribution of dislocation sources affect the hyperbolic CDD system Eq. (11). The present simulations should therefore be interpreted as transport-driven CDD simulations with a simplified Frank–Read-type multiplication term rather than as a complete dislocation reaction-kinetics model. More physical descriptions of dislocation multiplication would incorporate additional source and sink contributions representing annihilation, cross-slip, glissile junction formation, lock formation, and forest interactions, as derived in [6,17,33,60,61]. In such models, the multiplication rate is no longer governed by a fixed source population with prescribed lengths and locations, but emerges from the local dislocation reaction kinetics and may take a form that bears little structural resemblance to the FR bow-out picture used here. These extensions are left for future work.

With $\dot{\gamma}^s$ determined from Orowan's relation Eq. (7) and the CDD-driven dislocation evolution from Eq. (11), it remains to specify how $\mathbf{F}_\mathrm{p}$ is advanced in time. For a time step $\triangle t$ and $\mathbf{L}_\mathrm{p}^{n+1} = \sum_s \dot{\gamma}^{s,n+1}\mathbf{M}_t^s$ evaluated at t^{n+1}, we update $\mathbf{F}_\mathrm{p}$ locally by either backward-Euler (BE) or an exponential-map (EXP),

$$\mathbf{F}_\mathrm{p}^{n+1} = \left(\mathbf{I} - \triangle t\, \mathbf{L}_\mathrm{p}^{n+1}\right)^{-1} \mathbf{F}_\mathrm{p}^{n}, \tag{14a}$$

$$\mathbf{F}_\mathrm{p}^{n+1} = \exp\left(\triangle t\, \mathbf{L}_\mathrm{p}^{n+1}\right) \mathbf{F}_\mathrm{p}^{n}. \tag{14b}$$

Both are consistent with $\dot{\mathbf{F}}_\mathrm{p} = \mathbf{L}_\mathrm{p}\mathbf{F}_\mathrm{p}$. The backward-Euler update is computationally cheaper but does not exactly preserve rotations or plastic volume. When $\operatorname{tr}\mathbf{L}_\mathrm{p} = 0$, an isochoric projection is applied following [62, Sec. 8.3.2].

We next compare the present CDD-driven constitutive model to the classical framework of associative viscoplasticity, following [62, Sec. 2.7]. For each slip system s, we define the overstress function

$$h^s(\mathbf{S}_\mathrm{e}, \rho^s) := |\tau^s| - \tau_\mathrm{y}^s(\rho^s),$$

together with the Perzyna-type viscosity function

$$g(h^s) := \langle h^s \rangle = \max(h^s, 0).$$

Combining Eqs. (7) and (8) then gives the flow rule of our CDD–CP model,

$$\dot{\gamma}^s = \frac{(b^s)^2\rho^s}{B}\, g\left(h^s(\mathbf{S}_\mathrm{e}, \rho^s)\right)\ \operatorname{sign}(\tau^s).$$

This has the structure of a slip-system-wise Perzyna overstress law with associative flow direction, since

$$\frac{\partial h^s}{\partial \mathbf{S}_\mathrm{e}} = \operatorname{sign}(\tau^s)\, \mathbf{M}_t^s.$$

The corresponding effective viscosity of the rate-dependent model is

$$\eta^s = \frac{B}{(b^s)^2\rho^s},$$

and is therefore governed by the dislocation density. In particular, larger ρ^s and smaller B (that is, smaller η^s) lead to faster relaxation and a response closer to rate-independent plasticity, whereas smaller ρ^s and larger B yield stronger rate regularization.

Accordingly, the finite-strain plastic flow rule of the CDD–CP model can be written as

$$\mathbf{L}_\mathrm{p} = \sum_{s=1}^{S'} \dot{\gamma}^s\, \mathbf{M}_t^s = \sum_{s=1}^{S'} \underbrace{\frac{1}{\eta^s}}_{\frac{(b^s)^2\rho^s}{B}} \underbrace{g\left(h^s(\mathbf{S}_\mathrm{e}, \rho^s)\right)}_{\text{Perzyna overstress}} \underbrace{\frac{\partial h^s}{\partial \mathbf{S}_\mathrm{e}}}_{\operatorname{sign}(\tau^s)\,\mathbf{M}_t^s}.$$

Hence, the model may be interpreted as a multi-surface associative Perzyna viscoplasticity formulation in which the overstress function is $g(h^s) = \langle h^s \rangle$ and the flow direction is given by $\partial h^s/\partial \mathbf{S}_\mathrm{e} = \operatorname{sign}(\tau^s)\,\mathbf{M}_t^s$, cf. [62, Box 2.3].

2.2. Numerical solution for the elliptic force equilibrium problem

To solve the macro-scale force-balance problem (Eq. (1)), we first introduce the solution and test spaces

$$\mathbf{U}_0 := \{\, \mathbf{u} \in H^1(V_0;\mathbb{R}^3) : \mathbf{u} = \bar{\mathbf{u}} \text{ on } \Gamma_\mathrm{d} \,\}, \qquad \mathcal{W}_0 := \{\, \mathbf{w} \in H^1(V_0;\mathbb{R}^3) : \mathbf{w} = \mathbf{0} \text{ on } \Gamma_\mathrm{d} \,\},$$

where $H^1(V_0;\mathbb{R}^3)$ denotes the usual Sobolev space of square-integrable vector-valued functions with square-integrable first weak derivatives. Taking a virtual displacement $\mathbf{w} \in \mathcal{W}_0$, multiplying Eq. (1) by $\mathbf{w}$, and integrating over V_0 yields the following weak (virtual work) formulation of the force equilibrium problem.

Problem 2.1. We seek $\mathbf{u} \in \mathbf{U}_0$ such that

$$\int_{V_0} \mathbf{P}(\mathbf{F}(\mathbf{u})) : \nabla_0 \mathbf{w}\, \mathrm{d}V_0 = \int_{V_0} \mathbf{b}_0 \cdot \mathbf{w}\, \mathrm{d}V_0 + \int_{\Gamma_\mathrm{t}} \mathbf{t}_0 \cdot \mathbf{w}\, \mathrm{d}A_0 \qquad \forall\, \mathbf{w} \in \mathcal{W}_0. \tag{15}$$

We now describe the spatial discretization used to solve Problem 2.1. The loading process is parameterized by a pseudo-time variable with discrete time levels $0 = t_0 < t_1 < \cdots < t_{N_t} = T$, where N_t denotes the total number of time steps and T the final loading time. For each time step t_n, let $V_\ell \subset H^1(V_0; \mathbb{R}^3)$ be a conforming finite-element space constructed componentwise from scalar shape functions $\{\varphi_j\}_{j=1}^{n_\ell}$, where n_ℓ denotes the number of scalar basis functions. The displacement field is approximated by

$$\mathbf{u}_\ell = \sum_{j=1}^{n_\ell} \varphi_j \, \mathbf{d}_j,$$

where $\mathbf{d}_j \in \mathbb{R}^3$ are the nodal displacement vectors. We employ three-dimensional isoparametric H^1-conforming finite elements, for example trilinear hexahedra. For node i and Cartesian direction $\alpha \in \{1, 2, 3\}$ (corresponding to the x-, y-, and z-directions, respectively), we choose the test function $\mathbf{w}_\ell = \varphi_i \, \mathbf{e}_\alpha$, where $\mathbf{e}_\alpha$ denotes the αth Cartesian unit vector, so that

$$\nabla_0 \mathbf{w}_\ell = (\nabla_0 \varphi_i) \otimes \mathbf{e}_\alpha.$$

The corresponding discrete deformation gradient is

$$\mathbf{F}(\mathbf{u}_\ell) = \mathbf{I} + \nabla_0 \mathbf{u}_\ell, \qquad \nabla_0 \mathbf{u}_\ell = \sum_{j=1}^{n_\ell} (\nabla_0 \varphi_j) \otimes \mathbf{d}_j.$$

Dirichlet boundary conditions on Γ_d are imposed by defining the discrete trial and test spaces

$$U_\ell(t_n) := \{\mathbf{u}_\ell \in V_\ell \mid \mathbf{u}_\ell = \bar{\mathbf{u}}(\cdot, t_n) \text{ on } \Gamma_\mathrm{d}\}, \qquad W_\ell^0 := \{\mathbf{w}_\ell \in V_\ell \mid \mathbf{w}_\ell = \mathbf{0} \text{ on } \Gamma_\mathrm{d}\}.$$

The weak problem (15) at time t_n is thus reduced to a finite-dimensional nonlinear system: find $\mathbf{u}_\ell^n \in U_\ell(t_n)$ such that the global residual $\mathbf{r}(\mathbf{u}_\ell^n)$ vanishes.

The residual is obtained by testing the weak form with the basis functions of W_ℓ^0. In particular, for node i and Cartesian direction α, we choose $\mathbf{w}_\ell = \varphi_i \, \mathbf{e}_\alpha$, which gives the componentwise internal and external force contributions

$$f_{i\alpha}^{\mathrm{int}}(\mathbf{u}_\ell) := \int_{V_0} \mathbf{P}\big(\mathbf{F}(\mathbf{u}_\ell)\big) : \big[(\nabla_0 \varphi_i) \otimes \mathbf{e}_\alpha\big] \, \mathrm{d}V_0, \tag{16}$$

$$f_{i\alpha}^{\mathrm{ext}} := \int_{V_0} (\mathbf{b}_0 \cdot \mathbf{e}_\alpha) \, \varphi_i \, \mathrm{d}V_0 + \int_{\Gamma_\mathrm{t}} (\mathbf{t}_0 \cdot \mathbf{e}_\alpha) \, \varphi_i \, \mathrm{d}A_0. \tag{17}$$

The discrete residual component is then

$$r_{i\alpha}(\mathbf{u}_\ell) := f_{i\alpha}^{\mathrm{int}}(\mathbf{u}_\ell) - f_{i\alpha}^{\mathrm{ext}}.$$

Stacking all components yields the global residual vector

$$\boxed{\mathbf{r}(\mathbf{u}_\ell) = \int_{V_0} \mathbf{P}\big(\mathbf{F}(\mathbf{u}_\ell)\big) : \nabla_0 \boldsymbol{\varphi} \, \mathrm{d}V_0 - \mathbf{f}_{\mathrm{ext}}} \tag{18}$$

where $\nabla_0 \boldsymbol{\varphi}$ collects all basis-function gradients and $\mathbf{f}_{\mathrm{ext}}$ assembles the body-force and traction contributions.

We solve the nonlinear system $\mathbf{r}(\mathbf{u}_\ell) = \mathbf{0}$ by a Newton method with backtracking line search, following [44, Ch. 2.2.6]. The algorithm is summarized in Algorithm 1. At global Newton iteration k_{glb}, we assemble the Jacobian matrix $\mathbf{J}(\mathbf{u}_\ell) = \partial \mathbf{r}(\mathbf{u}_\ell)/\partial \mathbf{u}_\ell$ and compute the Newton increment $\Delta \mathbf{u}_\ell^{k_{\mathrm{glb}}}$ from

$$\mathbf{J}(\mathbf{u}_\ell^{k_{\mathrm{glb}}}) \, \Delta \mathbf{u}_\ell^{k_{\mathrm{glb}}} = \mathbf{r}(\mathbf{u}_\ell^{k_{\mathrm{glb}}}) \tag{19}$$

using a linear solver such as GMRES [63]. The iterate is then updated according to

$$\mathbf{u}_\ell^{k_{\mathrm{glb}}+1} = \mathbf{u}_\ell^{k_{\mathrm{glb}}} - \lambda \, \Delta \mathbf{u}_\ell^{k_{\mathrm{glb}}},$$

where the step length $\lambda \in (0, 1]$ is determined by backtracking. More precisely, starting from $\lambda = 1$, we repeatedly halve λ until

$$\|\mathbf{r}(\mathbf{u}_\ell^{k_{\mathrm{glb}}+1})\| < \|\mathbf{r}(\mathbf{u}_\ell^{k_{\mathrm{glb}}})\|.$$

The iteration is terminated once the norm of the global residual falls below a prescribed tolerance.

To assemble $\mathbf{J}(\mathbf{u}_\ell)$, let $\Delta \mathbf{u}_\ell = \sum_j \varphi_j \, \Delta \mathbf{d}_j$ be an arbitrary displacement increment. Then

$$\Delta \mathbf{F} = \nabla_0 \, \Delta \mathbf{u}_\ell = \sum_j (\nabla_0 \varphi_j) \otimes \Delta \mathbf{d}_j.$$

Linearization of the constitutive response gives

$$\Delta \mathbf{P} = \mathbb{A}_{\mathrm{alg}} : \Delta \mathbf{F}, \qquad \mathbb{A}_{\mathrm{alg}} := \frac{\partial \mathbf{P}}{\partial \mathbf{F}},$$

where $\mathbb{A}_{\mathrm{alg}}$ denotes the fully consistent algorithmic tangent. The global Jacobian therefore reads

$$\boxed{\mathbf{J}(\mathbf{u}_\ell) = \frac{\partial \mathbf{r}(\mathbf{u}_\ell)}{\partial \mathbf{u}_\ell} = \int_{V_0} \left(\mathbb{A}_{\mathrm{alg}} : \frac{\partial \mathbf{F}(\mathbf{u}_\ell)}{\partial \mathbf{u}_\ell} \right) : \nabla_0 \boldsymbol{\varphi} \, \mathrm{d}V_0} \tag{20}$$

Algorithm 1: Newton's iterative method with backtracking line search

Input: assembler for $\mathbf{r}(\mathbf{u}_\ell)$ and $\mathbf{J}(\mathbf{u}_\ell)$, initial guess $\mathbf{u}_\ell$, maximum iterations $k_{\mathrm{glb,max}}$, tolerance parameters $\epsilon_{\mathrm{glb,abs}}$, $\epsilon_{\mathrm{glb,rel}}$, maximum line-search steps $k_{\mathrm{ls,max}}$, time step t_n
Output: approximate solution $\mathbf{u}_\ell$

```
Initialize (u_ℓ)   // use the converged solution from t_{n-1} as initial guess and impose u_ℓ = ū(t_n) on Γ_d
r ← Residual(u_ℓ)                                                    // Eq. (18), see Algorithm 3
ϵ ← ϵ_glb,abs + ϵ_glb,rel ‖r‖
for k_glb ← 0 to k_glb,max − 1 do
    if ‖r‖ < ϵ then
        break
    J ← Jacobian(u_ℓ)                                                // Eq. (20), see Algorithm 5
    Δu_ℓ ← SolveLinear(J, r)                                         // solve Eq. (19) by GMRES
    λ ← 1
    for k_ls ← 0 to k_ls,max do
        u_ℓ^trial ← u_ℓ − λ Δu_ℓ
        r^trial ← Residual(u_ℓ^trial)                                // Eq. (18), see Algorithm 3
        if ‖r^trial‖ < ‖r‖ then
            break
        λ ← λ/2                                                      // backtracking line search
    u_ℓ ← u_ℓ^trial
    r ← r^trial
return u_ℓ
```

where $\partial\mathbf{F}/\partial\mathbf{u}_\ell$ denotes the linear map $\Delta\mathbf{u}_\ell \mapsto \Delta\mathbf{F} = \nabla_0 \Delta\mathbf{u}_\ell$. After discretization with the basis of W_ℓ^0, this variational expression yields the assembled Jacobian matrix $\mathbf{J}(\mathbf{u}_\ell)$.

The derivation of the fully consistent tangent $\mathbb{A}_{\mathrm{alg}}$, as well as the corresponding local constitutive update, is detailed in Appendix A. The assembly procedures for $\mathbf{r}(\mathbf{u}_\ell)$ and $\mathbf{J}(\mathbf{u}_\ell)$ used in Algorithm 1 are given in Algorithms 3 and 5, respectively.

2.3. Numerical solution for the hyperbolic CDD transport problem

To solve the micro-scale CDD problem (Eq. (11)), we rewrite the balance laws in conservative form. For each slip system $s \in \{1, \dots, S'\}$, we collect the CDD state variables into

$$\boldsymbol{Q}^s := \left(\rho^s, \kappa^s_{\mathrm{screw}}, \kappa^s_{\mathrm{edge}}, q^s\right)^{\mathsf{T}} \in \mathbb{R}^4.$$

The global state vector is then $\boldsymbol{Q} = (\boldsymbol{Q}^s)_{s=1}^{S'}$, with pointwise state dimension $n_Q = 4S'$. Throughout this subsection, ∇ and $\nabla\cdot$ denote the spatial gradient and spatial divergence. The CDD system can then be written as

$$\partial_t \boldsymbol{Q} + \nabla \cdot \boldsymbol{\mathcal{F}}(\boldsymbol{Q}) = \boldsymbol{\mathcal{S}}(\boldsymbol{Q}) \qquad \text{in } V \times (0, T], \tag{21}$$

where $\boldsymbol{\mathcal{F}}(\boldsymbol{Q})$ denotes the spatial flux tensor and $\boldsymbol{\mathcal{S}}(\boldsymbol{Q})$ collects the source terms. The explicit forms of $\boldsymbol{\mathcal{F}}$ and $\boldsymbol{\mathcal{S}}$ were derived in the small-deformation setting in [64] and are extended here to finite deformation.

Since the CDD transport equations are formulated in the spatial configuration while the mesh $\mathcal{T}_h$ is fixed in the reference configuration, all spatial differential operators must be expressed in terms of reference-frame quantities. Denoting the material gradient by ∇_0, the spatial gradient of a scalar field w_h is obtained via

$$\nabla w_h = \mathbf{F}^{-\mathsf{T}} \nabla_0 w_h. \tag{22}$$

For a reference surface element with outward unit normal $\mathcal{N}_0$, the corresponding spatial outward normal $\mathcal{N}$ and area element $\mathrm{d}A$ follow from Nanson's formula,

$$\mathcal{N}\,\mathrm{d}A = J\mathbf{F}^{-\mathsf{T}}\mathcal{N}_0\,\mathrm{d}A_0, \qquad J = \det\mathbf{F}, \tag{23}$$

where $\mathrm{d}A_0$ denotes the reference area element. These relations are applied consistently throughout the assembly of the DG flux terms and surface integrals below.

We discretize Eq. (21) in space by a discontinuous Galerkin method in strong form; see, for example, [65, Sec. 5]. Let $\mathcal{T}_h$ be a partition of V_0 into hexahedral elements $\mathcal{K}$, and define the discontinuous polynomial space

$$\mathcal{W}_h = \left\{ \boldsymbol{\psi} \in [L^2(V_0)]^{n_Q} \;:\; \boldsymbol{\psi}|_{\mathcal{K}} \in [\mathbb{P}_p(\mathcal{K})]^{n_Q} \quad \forall \mathcal{K} \in \mathcal{T}_h \right\},$$

where $\mathbb{P}_p(\mathcal{K})$ denotes the space of polynomials of degree at most p on $\mathcal{K}$, and $\boldsymbol{\psi}|_{\mathcal{K}}$ denotes the restriction of $\boldsymbol{\psi}$ to $\mathcal{K}$. We approximate $\boldsymbol{Q}$ by $\boldsymbol{Q}_h(t) \in \mathcal{W}_h$ and use the same space for the test functions $\boldsymbol{\psi} \in \mathcal{W}_h$.

In the implementation, the CDD problem is solved slip system by slip system. For a fixed slip system $s \in \{1, \dots, S'\}$, let $\{\varphi_j\}_{j=1}^{N_s}$ denote the scalar DG basis functions associated with that slip-system solve, where N_s is the number of scalar DG degrees of freedom. We represent the vector-valued unknown by

$$\mathcal{Q}_h^s(\mathbf{X}, t) = \sum_{j=1}^{N_s} \mathbf{u}_{\mathrm{CDD},j}^s(t)\, \varphi_j(\mathbf{X}), \qquad \mathbf{u}_{\mathrm{CDD},j}^s(t) \in \mathbb{R}^4, \tag{24}$$

and collect the coefficient vectors $\mathbf{u}_{\mathrm{CDD},j}^s$ into the stacked vector $\mathbf{u}_{\mathrm{CDD}}^s(t) \in \mathbb{R}^{4N_s}$. All integrals in the formulation below are evaluated on the reference mesh $\mathcal{T}_h$ by pulling back spatial operators and surface normals via Eqs. (22) and (23). This yields the following semi-discrete strong-form DG formulation.

Problem 2.2. We seek $\mathcal{Q}_h(t) \in \mathcal{W}_h$ such that, for all test functions $\boldsymbol{\psi} \in \mathcal{W}_h$,

$$\begin{aligned} &\sum_{\mathcal{K} \in \mathcal{T}_h} \left[\int_{\mathcal{K}} \partial_t \mathcal{Q}_h \cdot \boldsymbol{\psi}\, \mathrm{d}V + \int_{\mathcal{K}} \big(\nabla \cdot \boldsymbol{\mathcal{F}}(\mathcal{Q}_h)\big) \cdot \boldsymbol{\psi}\, \mathrm{d}V \right. \\ &\left. + \int_{\partial \mathcal{K}} \Big(\widehat{\boldsymbol{\mathcal{F}}}_n(\mathcal{Q}_h^-, \mathcal{Q}_h^+; \mathcal{N}) - \boldsymbol{\mathcal{F}}(\mathcal{Q}_h^-)\mathcal{N} \Big) \cdot \boldsymbol{\psi}^-\, \mathrm{d}A \right] = \sum_{\mathcal{K} \in \mathcal{T}_h} \int_{\mathcal{K}} \boldsymbol{\mathcal{S}}(\mathcal{Q}_h) \cdot \boldsymbol{\psi}\, \mathrm{d}V. \end{aligned} \tag{25}$$

Here $\mathcal{N}$ denotes the outward spatial unit normal on $\partial\mathcal{K}$, obtained from $\mathcal{N}_0$ via Eq. (23), while $(\cdot)^-$ and $(\cdot)^+$ denote the interior and exterior traces, respectively. The quantity $\widehat{\boldsymbol{\mathcal{F}}}_n(\cdot, \cdot; \mathcal{N})$ is a numerical normal flux, that is, a consistent approximation of the physical normal flux $\boldsymbol{\mathcal{F}}(\cdot)\mathcal{N}$.

On interior faces, we use a consistent Riemann flux constructed by flux-vector splitting. The construction follows the small-deformation formulation of [64, Sec. 2.2], extended here to account for the finite-deformation geometry. For a face with spatial unit normal $\mathcal{N}$, we write

$$\widehat{\boldsymbol{\mathcal{F}}}_n(\mathcal{Q}_h^-, \mathcal{Q}_h^+; \mathcal{N}) = \boldsymbol{\mathcal{F}}^+(\mathcal{Q}_h^-; \mathcal{N}) + \boldsymbol{\mathcal{F}}^-(\mathcal{Q}_h^+; \mathcal{N}),$$

where $\boldsymbol{\mathcal{F}}^+(\cdot; \mathcal{N})$ collects the outgoing characteristic contributions (positive normal speeds) and $\boldsymbol{\mathcal{F}}^-(\cdot; \mathcal{N})$ the incoming contributions (negative normal speeds), so that

$$\boldsymbol{\mathcal{F}}(\mathcal{Q})\mathcal{N} = \boldsymbol{\mathcal{F}}^+(\mathcal{Q}; \mathcal{N}) + \boldsymbol{\mathcal{F}}^-(\mathcal{Q}; \mathcal{N}).$$

On boundary faces $f \subset \partial V_0$, the boundary condition is imposed through the numerical flux. For a transparent boundary, where dislocations may leave the surface freely, we suppress inflow and retain only the outgoing contribution by setting

$$\widehat{\boldsymbol{\mathcal{F}}}_n(\mathcal{Q}_h^-, \mathcal{Q}_h^+; \mathcal{N}) - \boldsymbol{\mathcal{F}}(\mathcal{Q}_h^-)\mathcal{N} = \mathbf{0}.$$

For a closed boundary, such as an impenetrable grain boundary, we enforce a vanishing normal flux,

$$\widehat{\boldsymbol{\mathcal{F}}}_n(\mathcal{Q}_h^-, \mathcal{Q}_h^+; \mathcal{N}) - \boldsymbol{\mathcal{F}}(\mathcal{Q}_h^-)\mathcal{N} = -\boldsymbol{\mathcal{F}}(\mathcal{Q}_h^-)\mathcal{N},$$

so that the correction term in Eq. (25) exactly cancels the interior normal flux.

Inserting the ansatz Eq. (24) into Eq. (25) yields, for each slip system s, a semi-discrete initial-value problem of the form

$$\dot{\mathbf{u}}_{\mathrm{CDD}}^s(t) = \mathbf{f}^s\big(\mathbf{u}_{\mathrm{CDD}}^s(t), t\big), \qquad \mathbf{u}_{\mathrm{CDD}}^s(0) = \mathbf{u}_{\mathrm{CDD},0}^s, \tag{26}$$

where $\mathbf{f}^s : \mathbb{R}^{4N_s} \times [0, T] \to \mathbb{R}^{4N_s}$ is assembled from three contributions on each element $\mathcal{K}$,

(i) the element-volume term $\int_{\mathcal{K}} (\nabla \cdot \boldsymbol{\mathcal{F}}(\mathcal{Q}_h^s)) \cdot \boldsymbol{\psi}\, \mathrm{d}V$,
(ii) the strong-form face correction $\int_{\partial\mathcal{K}} (\widehat{\boldsymbol{\mathcal{F}}}_n - \boldsymbol{\mathcal{F}}(\mathcal{Q}_h^{s,-})\mathcal{N}) \cdot \boldsymbol{\psi}^-\, \mathrm{d}A$, and
(iii) the source term $\int_{\mathcal{K}} \boldsymbol{\mathcal{S}}(\mathcal{Q}_h^s) \cdot \boldsymbol{\psi}\, \mathrm{d}V$.

The explicit time dependence in $\mathbf{f}^s(\cdot, t)$ enters through the CP-level quantities, namely the deformation gradient $\mathbf{F}(t)$ and the dislocation velocity field, which are supplied at each time step from the macro-scale solve.

Let $t_n \mapsto t_{n+1} = t_n + \Delta t$ denote a global time step. The slip systems are advanced sequentially by Lie splitting, which introduces a first-order splitting error in time, since the CDD transport is the computationally dominant step and time steps are constrained to resolve dislocation velocity gradients, this is accepted in practice. For $s = 1, \dots, S'$, we solve Eq. (26) from t_n to t_{n+1} while holding the remaining slip systems fixed at their most recently available values during the sweep. Each subsystem is advanced by the two-stage, second-order diagonally implicit Runge–Kutta scheme,

$$\mathbf{u}_{\mathrm{CDD}}^{s,n+1} = \mathbf{u}_{\mathrm{CDD}}^{s,n} + \Delta t \sum_{i=1}^{2} b_i \mathbf{k}_i^s, \qquad \mathbf{k}_i^s = \mathbf{f}^s\left(\mathbf{u}_{\mathrm{CDD}}^{s,n} + \Delta t \sum_{j=1}^{i} a_{ij} \mathbf{k}_j^s,\ t_n + c_i\, \Delta t \right),$$

with Butcher tableau

$$\begin{array}{c|cc} \frac{1}{4} & \frac{1}{4} & 0 \\ \frac{3}{4} & \frac{1}{2} & \frac{1}{4} \\ \hline & \frac{1}{2} & \frac{1}{2} \end{array}.$$

Algorithm 2: Computational sequence of the coupled CDD–CP simulation

Input: loading data: prescribed displacement $\bar{\mathbf{u}}$, traction $\mathbf{t}_0$, body force $\mathbf{b}_0$
Input: time-integration data: time-step size $\triangle t$, number of time steps N_t
Input: initial microstructure state: crystal rotation $\mathbf{R}_0$, plastic deformation gradient $\mathbf{F}_{\mathrm{p}}^0 = \mathbf{I}$, CDD state $\mathbf{u}_{\mathrm{CDD},0}^s$
Output: displacement field $\mathbf{u}$, plastic deformation gradient $\mathbf{F}_{\mathrm{p}}$, CDD state $\mathbf{u}_{\mathrm{CDD}}^s$ at all time steps
for $n \leftarrow 0$ **to** $N_t - 1$ **do**
  $t_{n+1} \leftarrow t_n + \triangle t$
  solve the macro-scale force-balance problem for $\mathbf{u}^{n+1}$ using $\mathbf{F}_{\mathrm{p}}^n$ // Algorithm 1
  evaluate τ^s, τ_{y}^s, and v^s for all $s = 1, \ldots, S'$
  for $s \leftarrow 1$ **to** S' **do**
    solve the CDD transport problem for $\mathbf{u}_{\mathrm{CDD}}^{s,n+1}$
  evaluate $\dot{\gamma}^s$ for all $s = 1, \ldots, S'$
  update $\mathbf{F}_{\mathrm{p}}^{n+1}$ using Eq. (14)

Here $\mathbf{k}_i^s \in \mathbb{R}^{4N_s}$ denotes the ith stage derivative, and

$$\mathbf{u}_{\mathrm{CDD},i}^s := \mathbf{u}_{\mathrm{CDD}}^{s,n} + \triangle t \sum_{j=1}^{i} a_{ij} \mathbf{k}_j^s$$

is the corresponding stage state at which $\mathbf{f}^s$ is evaluated. At each stage i, the source contribution, including Frank–Read nucleation, is evaluated at the stage time $t_n + c_i \triangle t$ and assembled into the stage right-hand side. Since $a_{ii} \neq 0$, each stage requires the solution of one sparse linear system, which is solved iteratively by GMRES preconditioned by point block Jacobi. This implicit time integration relaxes the CFL-type time-step restriction associated with explicit schemes for DG transport operators while retaining second-order accuracy in time within each slip-system solve.

We note that the curvature flux contains spatial derivatives of the dislocation velocity and depends on the alignment tensor, exhibiting higher regularity than the dislocation density itself. The strong-form DG discretization is therefore chosen to preserve the derivative structure of these velocity-dependent flux terms while maintaining stability in the presence of strongly heterogeneous dislocation distributions. The detailed derivation for the small-deformation case is given in [64], and the extension to finite deformation follows the same structure with spatial operators replaced by their reference-frame counterparts via Eqs. (22) and (23).

2.4. Overall structure of the coupled CDD–CP simulation

Before introducing the individual benchmark problems, we briefly summarize the computational structure of the coupled CDD–CP simulation. At each loading step t_n, the formulation combines two interacting subproblems, namely a macro-scale elliptic force-balance problem (Section 2.2) for the displacement field $\mathbf{u}$, and a set of micro-scale hyperbolic CDD transport problems (Section 2.3) for the dislocation states $\mathbf{u}_{\mathrm{CDD}}^s$ on the individual slip systems s.

The coupling is mediated by the plastic flow. The macro-scale stress state determines the resolved shear stresses and the corresponding dislocation velocities, whereas the evolving dislocation fields determine the plastic slip rates and thereby influence the constitutive response entering the force-balance problem.

At a given time step $t_n \rightarrow t_{n+1}$, the external loading is first prescribed through the boundary conditions of the force-balance problem. Using the current plastic deformation $\mathbf{F}_{\mathrm{p}}^n$ and dislocation state, the macro-scale equilibrium problem is then solved once for the displacement field. From the resulting stress state, the resolved shear stress and slip resistance are evaluated on each slip system, which determine the dislocation velocity. Next, for each slip system, the corresponding CDD transport problem is advanced in time, yielding updated fields for the total dislocation density, the GND components, and the curvature density. These updated dislocation fields define the slip rates through Orowan's relation, which are then used to update the plastic deformation to $\mathbf{F}_{\mathrm{p}}^{n+1}$ by the local integration rule in Eq. (14). The updated plastic state is subsequently used in the macro-scale equilibrium problem of the next loading step. The overall computational sequence is summarized in Algorithm 2.

3. Problem setup

This section defines the two benchmark configurations considered in this study, namely (i) a single-slip simple shear problem and (ii) uniaxial tensile tests of single-crystalline and polycrystalline specimens. In both cases, the micro-scale CDD problem is initialized by a spatially random dislocation density field. In the polycrystalline case, randomness also enters through the Voronoi grain morphology and the randomly assigned crystallographic orientations. These stochastic microstructural inputs affect both the macroscopic mechanical response and the evolving dislocation microstructure, and their propagation through the coupled CDD–CP model is one of the central subjects of the numerical study. For each configuration, we specify the geometry and boundary conditions of the macro-scale force-balance problem (Problem 2.1), as well as the initial and boundary conditions of the micro-scale CDD transport problem (Problem 2.2).

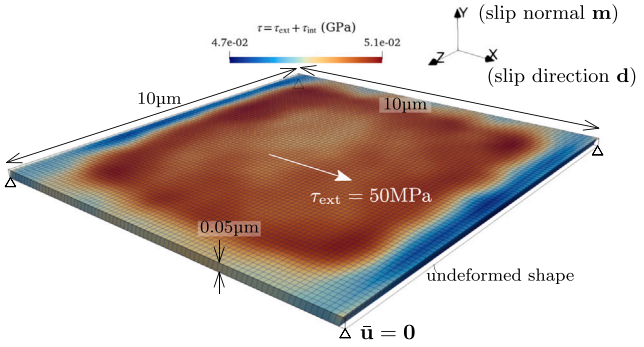

Fig. 1. Geometry and boundary conditions for the single-slip simple shear benchmark. The bottom face is fixed to remove rigid-body motion, all remaining faces are traction-free, and the specimen is loaded by a constant external resolved shear stress τ_{ext} on the active slip system.

3.1. Single-slip system under simple shear

This benchmark is designed to test CDD transport, Frank–Read multiplication, and surface escape in a controlled single-slip setting. Since only one slip system is active, isotropic elasticity is used for this test. The material parameters for the simplified isotropic copper reference material are summarized in Table 1.

The reference domain V_0 is a single-crystal specimen with dimensions $10\,\mu\text{m} \times 0.05\,\mu\text{m} \times 10\,\mu\text{m}$, containing a single active slip system. The slip direction is aligned with the x-axis, $\mathbf{d}_0 = \mathbf{e}_x$, the slip-plane normal with the y-axis, $\mathbf{m}_0 = \mathbf{e}_y$, and the in-plane edge direction of the slip-system basis is $\mathbf{l}_0 = \mathbf{m}_0 \times \mathbf{d}_0 = \mathbf{e}_z$. As established in Section 2.1, $\mathbf{l}_0$ is a fixed basis vector of the slip-system triad and should not be confused with the local line direction of individual dislocation segments. The initial crystal rotation is the identity, $\mathbf{R}_0 = \mathbf{I}$, corresponding to Tait–Bryan angles $\boldsymbol{\xi} = (0°, 0°, 0°)$ for all finite elements.

The computational mesh $\mathcal{T}_h$ consists of uniform hexahedral elements with mesh size $0.125\,\mu\text{m} \times 0.05\,\mu\text{m} \times 0.125\,\mu\text{m}$, resulting in $80 \times 1 \times 80$ elements over the reference domain. The force-balance problem (Problem 2.1) is solved using first-order continuous Galerkin finite elements, and the CDD transport problem (Problem 2.2) is solved using a first-order discontinuous Galerkin discretization on the same mesh. The geometry and boundary conditions are illustrated in Fig. 1.

The specimen is driven by a constant prescribed external resolved shear stress $\tau_{\text{ext}} = 50\,\text{MPa}$, which enters the resolved shear stress Eq. (9) on the active slip system as an additive contribution supplementing the Schmid projection of the mechanically computed stress $\mathbf{S}_e$. This loading strategy mimics a uniformly applied macroscopic shear stress and is commonly used in CDD studies to drive dislocation motion in a controlled setting [54,66], while the force-balance problem (Problem 2.1) is still solved at each loading step to resolve the displacement field, lattice rotation, and finite kinematics consistently. Body forces are neglected, $\mathbf{b}_0 = \mathbf{0}$, and the Neumann boundary $\Gamma_t = \partial V_0 \setminus \Gamma_d$ is traction-free, $\mathbf{t}_0 = \mathbf{0}$. To eliminate rigid-body motion, a Dirichlet condition is imposed on the bottom face $\Gamma_d = \{y = 0\}$,

$$\mathbf{u} = \bar{\mathbf{u}} = \mathbf{0} \qquad \text{on } \Gamma_d.$$

This benchmark is therefore best understood as a reduced CDD transport test in which the mechanical coupling is present but the dominant driving force is the prescribed uniform shear stress, rather than a stress field generated by inhomogeneous displacement boundary conditions.

The CDD transport problem (Problem 2.2) is initialized by spatially heterogeneous fields on the active slip system. We generate a high-resolution random field $\Xi(\mathbf{X}) \sim \text{Uniform}(-1, 1)$ and project it onto the computational mesh $\mathcal{T}_h$. The initial dislocation density and curvature density are prescribed as

$$\rho(\mathbf{X}, 0) = \rho_0\,|\Xi(\mathbf{X})|, \qquad q(\mathbf{X}, 0) = q_0\,\Xi(\mathbf{X}) = k_0\rho_0\,\Xi(\mathbf{X}),$$

with $\rho_0 = 0.6\,\mu\text{m}^2$ and $k_0 := q_0/\rho_0 = 64\,\mu\text{m}$. The initial GND vector is set to zero, $\boldsymbol{\kappa}(\mathbf{X}, 0) = \mathbf{0}$, so that no resolved net GND density is prescribed at the continuum scale at the start of the simulation.

These initial fields are interpreted as stochastic continuum representations of unresolved closed dislocation loops below the spatial discretization scale, as illustrated in Fig. 2. The prescribed curvature k_0 corresponds to a characteristic loop radius $1/k_0 \approx 15.6\,\text{nm}$, which is smaller than the mesh size $0.125\,\mu\text{m}$, confirming that the initial loops are not resolved as individual dislocation lines but enter through the sub-element continuum CDD fields ρ and q. During loading, transport, curvature evolution, dislocation source activity, and boundary escape evolve the fields ρ, $\boldsymbol{\kappa}$, and q, so that the GND vector need not remain zero.

Dislocation sources are introduced with a constant effective source length $l_{\text{FR}} = 0.4\,\mu\text{m}$, prescribed as a benchmark simplification to isolate the effects of source density and source location. The spatial support of the source-density field is prescribed stochastically by generating a high-resolution Bernoulli field $I(\mathbf{X}) \in \{0, 1\}$, projecting it onto the mesh, and restricting source activity to regions with nonzero initial dislocation density,

$$n_{\text{FR}}(\mathbf{X}) = n_{\text{FR},0}\,I(\mathbf{X})\,\mathbb{1}_{\{\rho(\mathbf{X},0)>0\}}.$$

Table 1
Material and initial microstructure parameters used for the single-slip simple shear benchmark. The solver tolerances and iteration limits are those used in the Newton and local update algorithms described in Appendix A.

Parameter	Value	Parameter	Value
Simplified isotropic copper reference material			
E	117 GPa [67]	ν	0.35 [68]
μ	43 GPa [67]	a	0.35 [69]
b	0.254 nm [70]	B	5×10^{-5} Pa s [52]
c_{FR}	3.92 [33]		
CDD initialization $\mathbf{u}^{s}_{\mathrm{CDD},0}$ for the single slip system			
ρ_0	$0.6\,\mu\mathrm{m}^{-2}$	$k_0 := q_0/\rho_0$	$64\,\mu\mathrm{m}^{-1}$
l_{FR}	0.4 µm	N_{FR}	{0, 50, 500}
$\boldsymbol{\kappa}_0$	$\mathbf{0}$	S'	1
Numerical discretization and solver settings			
CG degree	1	DG degree	1
Δt	0.1 ms	Final time T	500 ms
$N_t = T/\Delta t$	5000		
GMRES preconditioner	Point block Jacobi	GMRES tolerance	1e−8
GMRES restart/max iters	1000		
$\epsilon_{\mathrm{glb,abs}}$	1e−8	$\epsilon_{\mathrm{glb,rel}}$	1e−12
$k_{\mathrm{glb,max}}$	10	$k_{\mathrm{ls,max}}$	5
$\epsilon_{\mathrm{loc,abs}}$	1e−8	$\epsilon_{\mathrm{loc,rel}}$	1e−12
$k_{\mathrm{loc,max}}$	50		

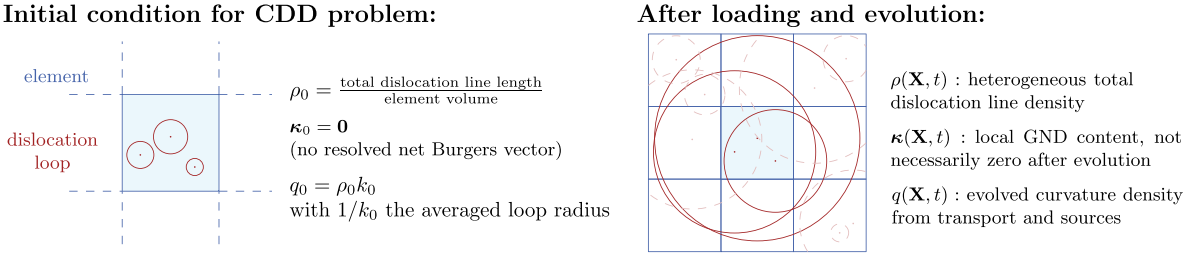

Fig. 2. Interpretation of the stochastic CDD initial condition. The initial fields represent unresolved closed dislocation loops below the spatial discretization scale, with ρ_0 prescribing the total dislocation line density, $\boldsymbol{\kappa}_0 = \mathbf{0}$ prescribing no resolved net GND density, and $q_0 = \rho_0 k_0$ prescribing the initial curvature density. During loading and CDD evolution, the fields $\rho(\mathbf{X}, t)$, $\boldsymbol{\kappa}(\mathbf{X}, t)$, and $q(\mathbf{X}, t)$ evolve through transport, source activity, and boundary escape.

The constant $n_{\mathrm{FR},0}$ is chosen such that $\int_{V_0} n_{\mathrm{FR}}\,\mathrm{d}V_0 = N_{\mathrm{FR}}$, and we consider $N_{\mathrm{FR}} \in \{0, 50, 500\}$, where N_{FR} denotes the prescribed total strength of the continuum source-density field expressed as an equivalent number of sources.

Transparent boundary conditions are imposed on the entire boundary ∂V_0, allowing dislocations to leave the surface freely,

$$\widehat{\boldsymbol{\mathcal{F}}}_n(\boldsymbol{\mathcal{Q}}^-, \boldsymbol{\mathcal{Q}}^+; \mathcal{N}) - \boldsymbol{\mathcal{F}}(\boldsymbol{\mathcal{Q}}^-)\mathcal{N} = \mathbf{0} \qquad \text{on } \partial V_0.$$

3.2. Single-crystalline and polycrystalline tensile test

This benchmark studies uniaxial tensile loading of single-crystalline and polycrystalline copper specimens with cubic anisotropic elasticity, using 12 FCC slip systems. The material parameters are summarized in Table 3.

Both specimens share the same reference domain V_0 with dimensions $100\,\mu\mathrm{m} \times 400\,\mu\mathrm{m} \times 100\,\mu\mathrm{m}$ and the same computational mesh $\mathcal{T}_h$, consisting of uniform hexahedral elements with mesh size $h = 3.125\,\mu\mathrm{m} \times 3.125\,\mu\mathrm{m} \times 3.125\,\mu\mathrm{m}$, resulting in $32 \times 128 \times 32$ elements. The force-balance problem (Problem 2.1) is solved using first-order continuous Galerkin finite elements, and the CDD transport problem (Problem 2.2) is solved using a first-order discontinuous Galerkin discretization on the same mesh.

Tensile loading is imposed through Dirichlet boundary conditions on the bottom and top faces,

$$\bar{\mathbf{u}}(\mathbf{X}, t_n) = \begin{cases} \mathbf{0}, & y = 0\,\mu\mathrm{m}, \\ (0,\, u_y(t_n),\, 0), & y = 400\,\mu\mathrm{m}, \end{cases}$$

so that the bottom face is fixed and the top face is displaced in the y-direction. The remaining boundary $\Gamma_{\mathrm{t}} = \partial V_0 \setminus \Gamma_{\mathrm{d}}$ is traction-free, $\mathbf{t}_0 = \mathbf{0}$, and body forces are neglected, $\mathbf{b}_0 = \mathbf{0}$. The geometries and boundary conditions are illustrated in Fig. 3.

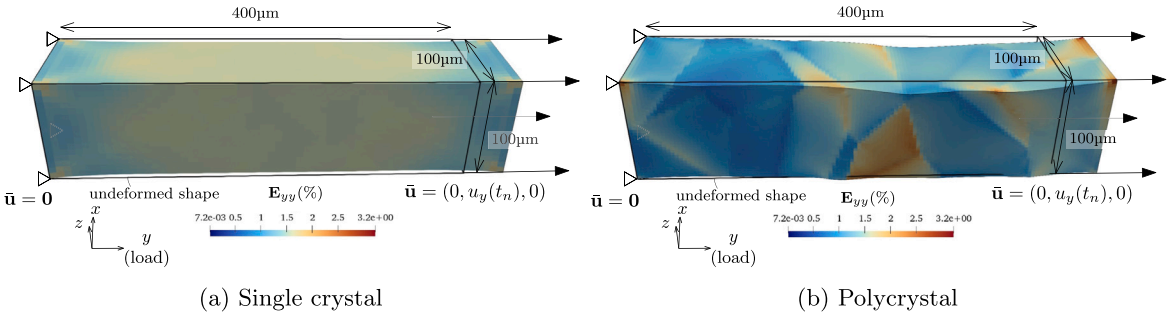

Fig. 3. Geometries and boundary conditions for the single-crystalline and polycrystalline tensile tests.

Table 2
Notation of the 12 FCC orthonormal slip-system bases. The labels A4, A5, etc. follow the Schmid–Boas notation, while the numbers in parentheses give the corresponding slip-system index s.

Slip system (s)	A4 (1)	A5 (2)	A2 (3)	B3 (4)	B6 (5)	B2 (6)
Plane normal $\mathbf{m}_0^s$	(111)	(111)	(111)	(11$\bar{1}$)	(1$\bar{1}$1)	(1$\bar{1}\bar{1}$)
Slip direction $\mathbf{d}_0^s$	[01$\bar{1}$]	[10$\bar{1}$]	[1$\bar{1}$0]	[011]	[101]	[1$\bar{1}$0]
Slip system (s)	C4 (7)	C6 (8)	C1 (9)	D3 (10)	D5 (11)	D1 (12)
Plane normal $\mathbf{m}_0^s$	($\bar{1}$11)	($\bar{1}$11)	($\bar{1}$11)	(1$\bar{1}$1)	(1$\bar{1}$1)	(1$\bar{1}$1)
Slip direction $\mathbf{d}_0^s$	[01$\bar{1}$]	[101]	[110]	[011]	[10$\bar{1}$]	[110]

To represent the stochastic crystallographic structure of the polycrystalline specimen, the reference domain V_0 is partitioned into $N = 25$ grains $\{G_n\}_{n=1}^N$ such that $V_0 = \bigcup_{n=1}^N G_n$ and $G_n \cap G_{n'} = \emptyset$ for $n \neq n'$. The grain structure is modeled by a Voronoi tessellation of seed points $\{\mathbf{c}_n\}_{n=1}^N$, where each $\mathbf{c}_n$ is sampled independently from the uniform distribution on V_0, with each grain defined by

$$G_n = \left\{\mathbf{X} \in V_0 \ : \ \|\mathbf{X} - \mathbf{c}_n\| \leq \|\mathbf{X} - \mathbf{c}_{n'}\| \text{ for all } n' \neq n\right\}.$$

Within each grain n, the crystallographic orientation is specified by the Tait–Bryan angles $\boldsymbol{\xi}_n = (\theta_n, \phi_n, \omega_n)$, following the rotation sequence convention in Eq. (4). The angles are generated from independent random variables $\mathcal{U}_{1,n}, \mathcal{U}_{2,n}, \mathcal{U}_{3,n} \sim \text{Uniform}(0, 1)$ as

$$\boldsymbol{\xi}_n = \left(2\pi\mathcal{U}_{1,n} - \pi,\ \arccos(1 - 2\mathcal{U}_{2,n}) - \frac{\pi}{2},\ 2\pi\mathcal{U}_{3,n} - \pi\right). \tag{27}$$

following [50, Ch. 17]. Because the aggregate contains only $N = 25$ grains, it should not be interpreted as a statistically converged representative volume element of an untextured polycrystal, but rather as a finite random aggregate used to test the interaction between grain morphology, lattice orientation, and CDD transport and pile-up. Plasticity in each grain is modeled using the 12 FCC slip systems of the $\{111\}\langle 110\rangle$ family (Table 2), rotated into the global frame by $\mathbf{R}_0(\boldsymbol{\xi}_n)$ as defined in Eq. (4). For the single-crystal specimens, three loading directions are considered, namely [010], [$\bar{1}$1$\bar{1}$], and [01$\bar{1}$], with the corresponding Tait–Bryan angles listed in Table 3.

The initial CDD fields are prescribed independently on each slip system and, in the polycrystalline case, independently within each grain. For each slip system $s = 1, \ldots, 12$, we generate a spatially heterogeneous random field $\Xi^s(\mathbf{X}) \sim \text{Uniform}(-1, 1)$, projected onto the computational mesh, and prescribe the initial dislocation density and curvature density as

$$\rho^s(\mathbf{X}, 0) = \rho_0^s\,|\Xi^s(\mathbf{X})|, \qquad q^s(\mathbf{X}, 0) = q_0^s\,\Xi^s(\mathbf{X}) = k_0^s\rho_0^s\,\Xi^s(\mathbf{X}).$$

The initial GND vector is set to zero on every slip system,

$$\boldsymbol{\kappa}^s(\mathbf{X}, 0) = \mathbf{0}, \qquad s = 1, \ldots, 12.$$

dislocation sources are initialized independently on each slip system with the source length l_{FR}^s and number of sources N_{FR}^s listed in Table 3.

For the CDD transport problem (Problem 2.2), we distinguish between external boundaries and internal grain boundaries. Transparent boundary conditions are imposed on the external boundary ∂V_0, allowing dislocations to leave the surface freely,

$$\widehat{\boldsymbol{\mathcal{F}}}_n(\mathcal{Q}^-, \mathcal{Q}^+; \mathcal{N}) \cdot \mathcal{N} = \mathbf{0} \qquad \text{on } \partial V_0.$$

On internal grain boundaries $\Gamma_{\text{gb}} = \bigcup_{n \neq n'}(\partial G_n \cap \partial G_{n'})$, dislocation transport across grain interfaces is prohibited through a zero normal-flux condition,

$$\widehat{\boldsymbol{\mathcal{F}}}_n(\mathcal{Q}_h^-, \mathcal{Q}_h^+; \mathcal{N}) = \boldsymbol{\mathcal{F}}^-(\mathcal{Q}_h^-; \mathcal{N}) \qquad \text{on } \Gamma_{\text{gb}}.$$

Table 3
Material and initial microstructure parameters used for the single-crystal and polycrystalline tensile simulations. The solver tolerances and iteration limits are those used in the Newton and local update algorithms described in Appendix A.

Parameter	Value	Parameter	Value
Copper material parameters with cubic anisotropic elasticity			
C_{11}	168 GPa [67]	C_{12}	121 GPa [67]
C_{44}	75 GPa [67]	μ	43 GPa [67]
b	0.254 nm [70]	a	0.35 [69]
B	5×10^{-5} Pa s [52]	c_{FR}	3.92 [33]
CDD initialization $\mathbf{u}^s_{\mathrm{CDD},0}$ prescribed for each slip system $s = 1, \ldots, S'$			
ρ^s_0	$0.6\,\mu\mathrm{m}^{-2}$	$k^s_0 := q^s_0/\rho^s_0$	$64\,\mu\mathrm{m}^{-1}$
l^s_{FR}	0.4 μm	N^s_{FR}	80
$\boldsymbol{\kappa}^s_0$	$\mathbf{0}$	S'	12
Initial crystal rotation $\mathbf{R}_0$, Tait–Bryan angles (θ, ϕ, ω)			
Single crystal [010]	(0°, 0°, 0°)	Single crystal $[\bar{1}1\bar{1}]$	(36.206°, 12.200°, −36.206°)
Single crystal $[01\bar{1}]$	(45°, 0°, 0°)	Polycrystal	Eq. (27)
Numerical discretization and solver settings			
CG degree	1	DG degree	1
$\triangle t$	0.002 ms	Final time T	50 ms
$N_t = T/\triangle t$	25 000		
GMRES preconditioner	Point block Jacobi	GMRES tolerance	1e−8
GMRES restart/max iters	1000		
$\epsilon_{\mathrm{glb,abs}}$	1e−6	$\epsilon_{\mathrm{glb,rel}}$	1e−6
$k_{\mathrm{glb,max}}$	50	$k_{\mathrm{ls,max}}$	5
$\epsilon_{\mathrm{loc,abs}}$	1e−6	$\epsilon_{\mathrm{loc,rel}}$	1e−6
$k_{\mathrm{loc,max}}$	50		

4. Numerical results

This section presents numerical results based on the proposed finite-deformation CDD–CP framework and compares the results with those obtained from the small-deformation formulation of [36,57]. We first examine the single-slip simple shear benchmark (Section 4.1) to assess how stochastic dislocation microstructures and dislocation source distributions govern the competition between dislocation multiplication and boundary escape. We next study single-crystal tensile tests (Section 4.3) for three crystallographic loading orientations, analyzing how lattice rotation drives secondary slip-system activation and how the two kinematic descriptions diverge at the microstructural level. Tensile simulations of stochastic polycrystalline aggregates (Section 4.4) then show how grain-boundary constraints and orientation mismatch amplify finite-deformation effects on the macroscopic response and plastic-strain distribution. An assessment of the robustness of the exponential-map and backward-Euler local plastic updates follows (Section 4.5), with particular attention to regions of large plastic increments. The section closes with ensemble simulations of 64 stochastic polycrystalline realizations (Section 4.6), demonstrating realization-to-realization variability while preserving consistent qualitative trends.

4.1. Single-slip microstructure evolution with random dislocations

We examine the single-slip simple shear benchmark introduced in Section 3.1 to assess whether the finite-deformation CDD–CP framework correctly captures the physical regimes of stochastic dislocation microstructure evolution under varying source activity. The prescribed initial density and curvature fields represent unresolved sub-element closed loops (see Fig. 2), and the total source strength is varied as $N_{\mathrm{FR}} \in \{0, 50, 500\}$ while all other parameters are held fixed. Dislocation multiplication is represented by the continuum source term introduced in Section 2.1, which serves as a simplified model for stress-driven multiplication mechanisms. All results use the finite-deformation CDD–CP formulation with the exponential-map time integrator. All dislocation-density fields are shown in the reference configuration V_0, consistent with the reference-coordinate formulation of the CDD equations, and the maximum engineering shear strain reached at $t = 500\,\mathrm{ms}$ is approximately $\gamma_{\max} \approx 0.02$ for all cases.

Fig. 4 shows the temporal evolution of the total dislocation density ρ under constant loading $\tau_{\mathrm{ext}} = 50\,\mathrm{MPa}$. The three cases exhibit qualitatively distinct behavior controlled by the competition between dislocation multiplication and boundary escape, providing a natural parameter study of the framework across three physically different regimes. For $N_{\mathrm{FR}} = 0$ shown in the first row of Fig. 4, no multiplication occurs beyond the initially seeded field. The initially sub-element closed loops expand outward under the applied shear stress, with segments of opposite sign moving in opposite directions. As the loops grow beyond the element scale, neighboring loops coalesce into larger density concentrations that remain mobile and migrate collectively toward the free surfaces, where they escape, leaving a nearly dislocation-free specimen. The dominant physics is therefore loop expansion followed by boundary escape.

For $N_{\mathrm{FR}} = 50$ shown in the second row of Fig. 4, the source term generates new loops locally alongside the expanding initial loops, producing scattered high-density clusters visible at early times. Unlike the $N_{\mathrm{FR}} = 0$ case, the domain-averaged density

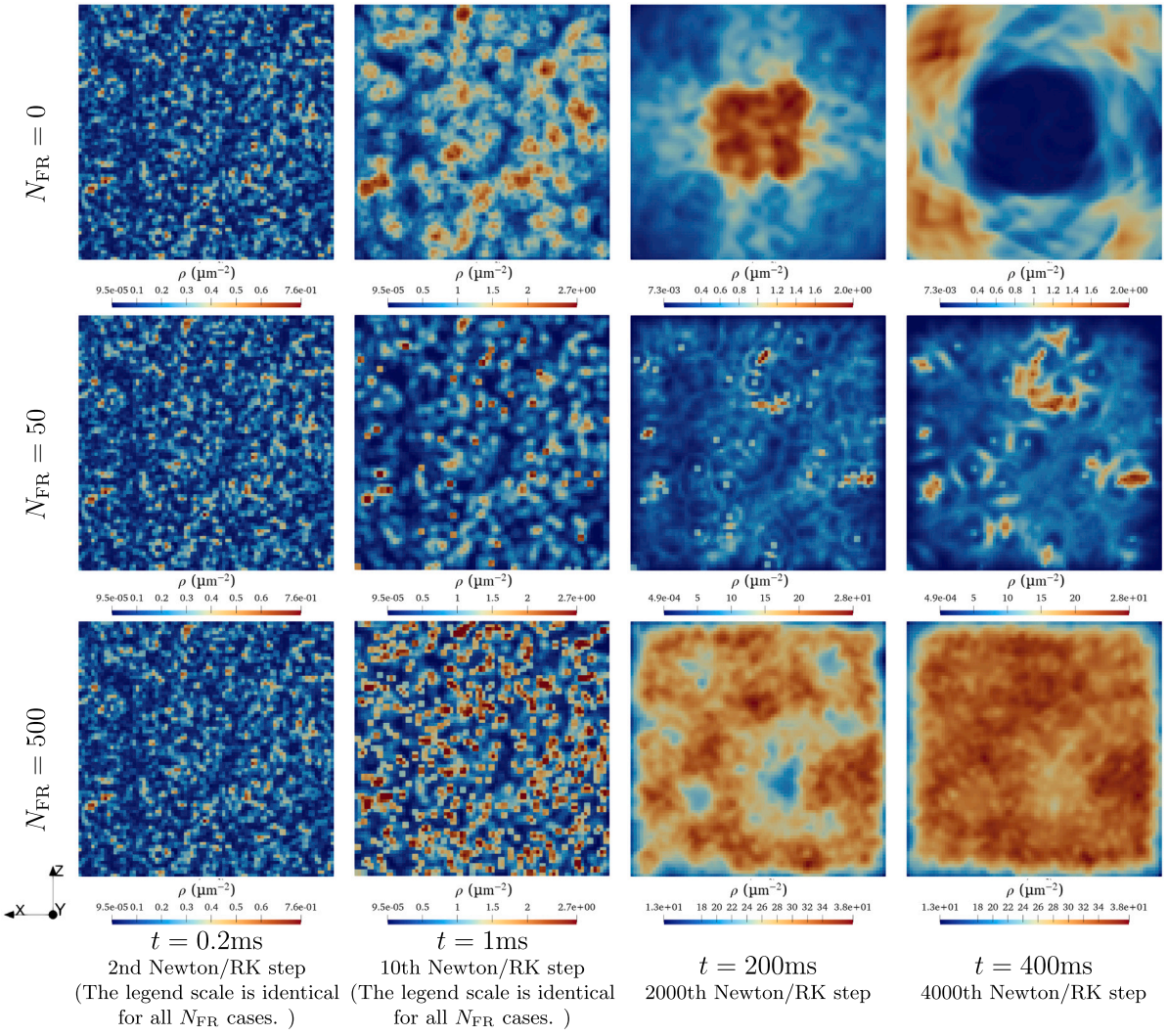

Fig. 4. Temporal evolution of the total dislocation density $\rho(\mathbf{X}, t)$ in the single-slip simple shear benchmark for $N_{FR} \in \{0, 50, 500\}$ under constant external resolved shear stress $\tau_{ext} = 50$ MPa. All cases start from the same stochastic initial CDD field and are shown on the plane $y = 0.05\,\mu$m in the reference configuration V_0. The color scale is shared across all N_{FR} cases at early times $t \in \{0.2\,\text{ms}, 1\,\text{ms}\}$ and is independent per row at later times to resolve the spatial structure within each regime. The final snapshot is shown at $t = 400$ ms since the $N_{FR} = 0$ case reaches a nearly dislocation-free state before $T = 500$ ms; the maximum engineering shear strain at $t = 500$ ms is approximately $\gamma_{max} \approx 0.02$ for all cases.

increases over the simulated interval as multiplication partially compensates boundary escape. However, the accumulated density remains spatially heterogeneous and largely mobile, and no persistent organized structure develops within the simulated time interval.

For $N_{FR} = 500$ shown in the third row of Fig. 4, multiplication is strong enough to continuously replenish density faster than boundary escape removes it. As the total density ρ grows throughout the bulk, the statistically random source and transport process generates roughly equal contributions of opposite-sign GND content, which largely cancel in the GND vector $\boldsymbol{\kappa}$ while still contributing to ρ as SSD density. This SSD accumulation raises the Taylor resistance τ_y until it approaches the applied stress τ_{ext} throughout most of the bulk, driving the dislocation velocity toward zero and arresting further dislocation transport through Taylor-hardening saturation. The domain approaches a quasi-steady state by $t = 200$ ms, with only a thin depletion zone near the free surfaces. The final state $t = 400$ ms is dominated by a nearly uniform high SSD density in the bulk interior, as shown in Fig. 6(d), rather than by a spatially organized pattern with a characteristic wavelength. The GND components, shown in Figs. 6(a) to 6(c), remain comparatively small and exhibit a residual filamentary structure that is a secondary imprint of the transport process rather than a dominant feature of the final state.

The mechanism leading to the saturated state for $N_{FR} = 500$ is illustrated in Fig. 5. Since the Taylor type slip resistance τ_y in Eq. (10) depends on the dislocation density ρ, the initially random density field immediately produces a heterogeneous resistance

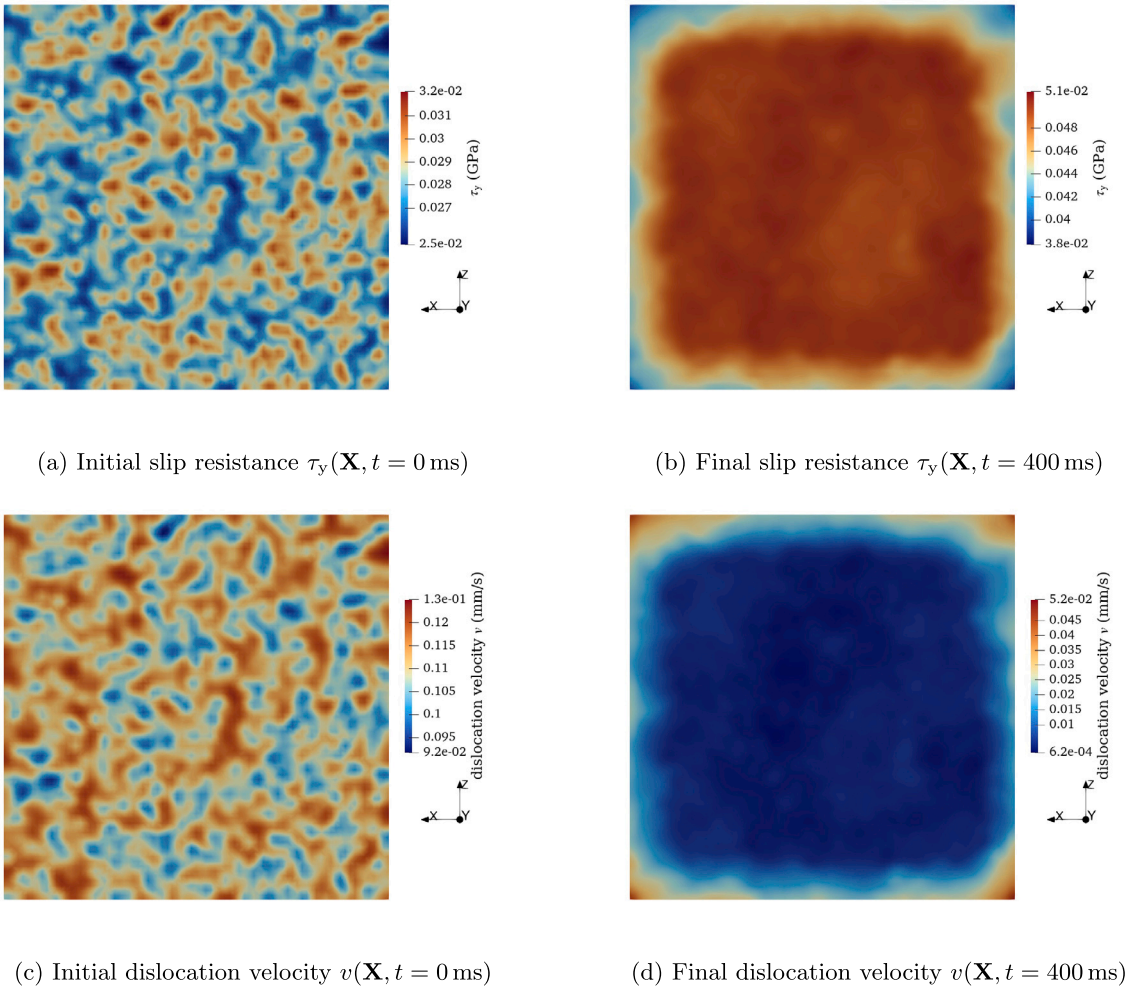

(a) Initial slip resistance $\tau_y(\mathbf{X}, t = 0\,\text{ms})$

(b) Final slip resistance $\tau_y(\mathbf{X}, t = 400\,\text{ms})$

(c) Initial dislocation velocity $v(\mathbf{X}, t = 0\,\text{ms})$

(d) Final dislocation velocity $v(\mathbf{X}, t = 400\,\text{ms})$

Fig. 5. Evolution of the slip resistance $\tau_y(\mathbf{X}, t)$ and dislocation velocity $v(\mathbf{X}, t)$ for $N_{FR} = 500$. The initially heterogeneous density field induces a heterogeneous Taylor resistance. Dislocation multiplication, transport, and boundary escape further modify τ_y, which saturates close to the applied stress and drives the dislocation velocity toward zero throughout the bulk.

field (see Fig. 5(a)) and, through the velocity law in Eq. (8), a nonuniform glide velocity, i.e., regions with lower τ_y permit faster transport while regions with higher τ_y move more slowly (see Fig. 5(c)). As dislocation loops evolve, CDD transport redistributes the existing density while the source term generates additional line density locally. Where density accumulates, τ_y increases and the local velocity decreases, reinforcing further accumulation. As the field evolves, τ_y saturates close to τ_{ext} throughout the bulk (see Fig. 5(b)), and the velocity approaches zero nearly everywhere (see Fig. 5(d)). The dominant outcome of the dislocation structure is therefore driven by Taylor-hardening saturation.

To further characterize the saturated state for $N_{FR} = 500$, Fig. 6 decomposes the final dislocation field into the screw and edge projections of $\boldsymbol{\kappa}$, the GND magnitude $\|\boldsymbol{\kappa}\|$, and the SSD density ρ_{SSD}. The projections of $\boldsymbol{\kappa}$ onto $\mathbf{d}$ and $\mathbf{l}$ quantify the net signed screw- and edge-character GND densities, $\|\boldsymbol{\kappa}\|$ the local net GND density, and ρ_{SSD} the part of ρ not contributing to the net GND vector. The decomposition confirms that the final state is dominated by ρ_{SSD}: the bulk interior is nearly uniformly filled with high SSD density, while the GND components are comparatively small and localized near boundary-affected regions. Opposite-signed contributions largely cancel in the interior, leaving small $\|\boldsymbol{\kappa}\|$ while still contributing to ρ as ρ_{SSD}. Since τ_y depends on ρ, this SSD-dominated bulk accumulation is the direct cause of the Taylor-hardening saturation described above. The filamentary structure visible in the GND magnitude field (see Figs. 6(a) to 6(c)) is a residual of the transport process and carries a secondary spatial organization reminiscent of the transport instability patterns of Sandfeld and Zaiser [66], but it is not the dominant feature of the final state.

The temporal evolution of spatially averaged dislocation measures is shown in Fig. 7. We plot

$$\bar{\rho} = \frac{1}{|V_0|}\int_{V_0} \rho(\mathbf{X}, t)\,\mathrm{d}V_0, \qquad \bar{\kappa}_{\text{screw}} = \frac{1}{|V_0|}\int_{V_0} \kappa_{\text{screw}}(\mathbf{X}, t)\,\mathrm{d}V_0, \qquad \bar{\kappa}_{\text{edge}} = \frac{1}{|V_0|}\int_{V_0} \kappa_{\text{edge}}(\mathbf{X}, t)\,\mathrm{d}V_0,$$

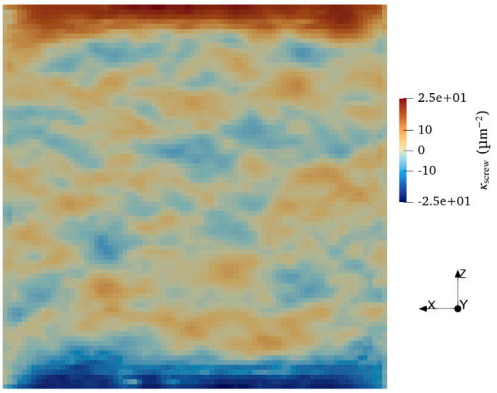

(a) Screw GND component $\kappa_{\mathrm{screw}}(\mathbf{X}, t = 400\,\mathrm{ms})$

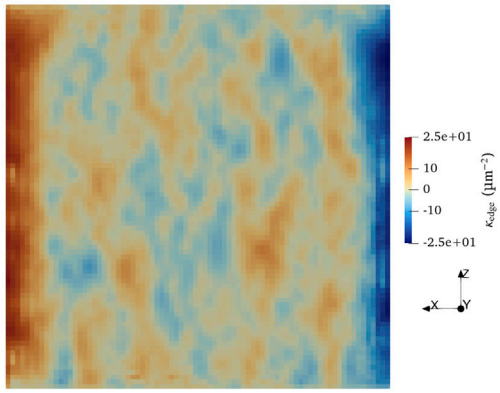

(b) Edge GND component $\kappa_{\mathrm{edge}}(\mathbf{X}, t = 400\,\mathrm{ms})$

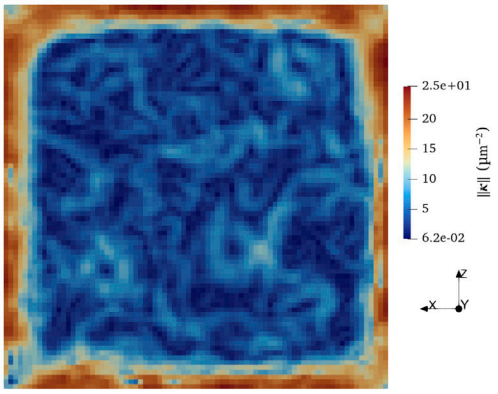

(c) GND magnitude $\|\boldsymbol{\kappa}\|(\mathbf{X}, t = 400\,\mathrm{ms})$

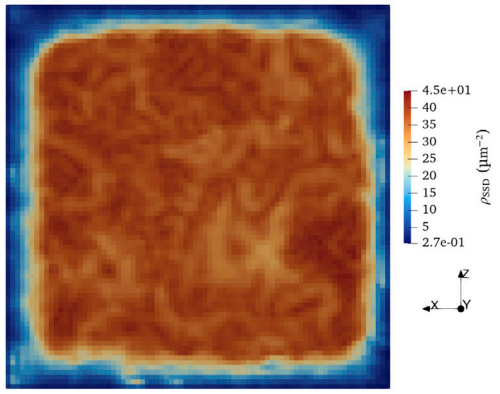

(d) SSD density $\rho_{\mathrm{SSD}}(\mathbf{X}, t = 400\,\mathrm{ms})$

Fig. 6. Dislocation-density components at the final time for $N_{\mathrm{FR}} = 500$. The fields κ_{screw} and κ_{edge} are the projections of the GND vector onto the screw and edge directions, $\|\boldsymbol{\kappa}\|$ is the GND magnitude, and $\rho_{\mathrm{SSD}} = \rho - \|\boldsymbol{\kappa}\|$ is the statistically stored part of the total dislocation density. The final state is dominated by a nearly uniform high SSD density in the bulk interior, consistent with Taylor-hardening saturation.

with shaded regions indicating the interquartile range of the spatial fields. The three regimes are clearly reflected in the averaged measures: for $N_{\mathrm{FR}} = 0$, the domain-averaged density decays monotonically as loops escape through the free surfaces; for $N_{\mathrm{FR}} = 50$, multiplication delays but does not prevent this decay; for $N_{\mathrm{FR}} = 500$, the averaged density grows rapidly and plateaus as the bulk saturates. In all cases, the spatial averages of κ_{screw} and κ_{edge} remain close to zero: positive and negative GND contributions generated during transport and loop bow-out largely cancel when integrated over the domain, confirming that no specimen-scale GND bias develops. The wide interquartile bands for $N_{\mathrm{FR}} = 500$ reflect the persistent spatial heterogeneity in the GND field, consistent with the filamentary structure observed in Fig. 6(c).

These results complete the physical characterization of the three source-density regimes. The broader continuum patterning literature provides useful context for interpreting the observed behavior, and in particular for understanding why the present simulations do not reproduce wavelength-selective dislocation patterns despite sharing the same underlying Taylor-type resistance mechanism. In scalar density models, Sandfeld and Zaiser [66] showed that Taylor-type flow resistance combined with CDD transport can destabilize a homogeneous dislocation arrangement and produce spontaneous wavelength-selective patterns, a mechanism further analyzed by Wu et al. [71] and Wu and Zaiser [72]. In vector-density CDD, Xia and El-Azab [27] demonstrated mesoscale patterning using multi-slip transport, and Lin and El-Azab [73] extended this by explicitly implementing annihilation and junction reactions. In dislocation-based CPFEM, Grilli et al. [74,75] showed that cross-slip and junction formation are necessary to reproduce

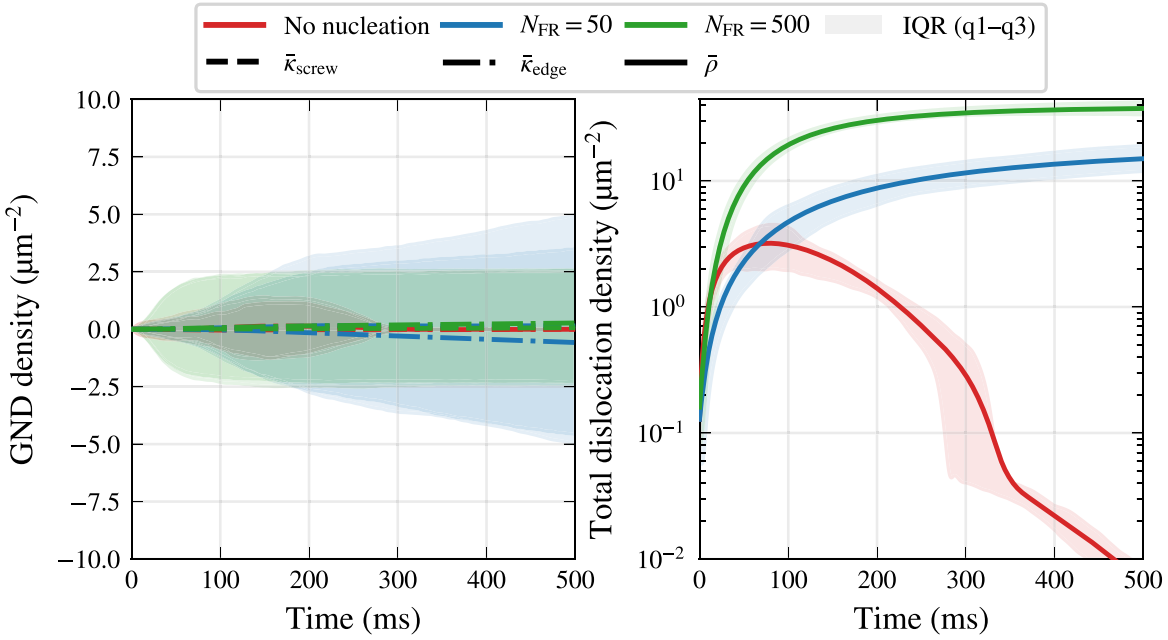

Fig. 7. Temporal evolution of spatially averaged dislocation measures for different source strengths. Solid curves show domain averages; shaded regions indicate the interquartile range.

vein, channel, and labyrinth structures. At finite deformation, Arora and Acharya [22] produced stressed dislocation patterns with non-zero net Burgers vector walls without constitutive cross-slip assumptions.

Despite sharing the same underlying mechanism of Taylor-type density-dependent resistance coupled to CDD transport, the present simulations do not reproduce the wavelength-selective patterns of Sandfeld and Zaiser [66]. Four differences in the setup account for this. First, their model contains no dislocation source and total number of dislocation loops is conserved, so patterning emerges purely from transport redistribution; here, the continuum source term continuously injects density that drives τ_y toward global saturation, suppressing spatial organization before it can develop. Second, they start from a near-homogeneous state whose small perturbations undergo wavelength-selective instability, whereas the present strongly heterogeneous initial condition bypasses this linear regime entirely. Third, the free surfaces act as dislocation sinks that compete with any instability growth. Fourth, Wu and Zaiser [72] show that a gradient stress proportional to $\nabla\rho$ is responsible for wavelength selection; without it the instability grows at all wavelengths without producing a characteristic length scale. The present model includes only internal stresses derived from $\boldsymbol{\kappa}$ and therefore would not be expected to produce wavelength selection even in a more favorable parameter regime. Reproducing wavelength-selective patterning within the present framework would therefore require more moderate multiplication rates, a geometry where boundary escape does not dominate, and the inclusion of gradient stress contributions to $\nabla\rho$.

These results demonstrate that the finite-deformation CDD–CP framework captures three qualitatively distinct regimes of single-slip microstructure evolution governed by the competition between dislocation multiplication and boundary escape. The density heterogeneity observed in all three cases arises from the interplay of the stochastic initial condition, the density-dependent Taylor resistance, CDD transport, and boundary escape, and should be distinguished from two other classes of results in the continuum patterning literature. The first class comprises the spontaneous wavelength-selective patterns arising from a homogeneous-state transport instability [66,71,72], and the second comprises fully developed cell structures whose formation requires physical reaction kinetics, including annihilation, junction formation, lock formation, and cross-slip [27,73–75], that are absent from the present model. The present benchmark is therefore best understood as a verification that the framework can propagate stochastic initial dislocation microstructures and source distributions through the coupled CDD–CP evolution and assess their effect on the final microstructural state across a physically relevant parameter range, rather than as a study of dislocation patterning per se. More physical descriptions of dislocation multiplication, incorporating reaction kinetics, cross-slip, and density-dependent source activity, enter the CDD evolution equations as additional source and sink terms in the same mathematical structure as Eq. (11), and can therefore be incorporated as natural extensions within the present stochastic finite-deformation framework. Similarly, more realistic initial microstructures could be obtained by homogenizing relaxed discrete dislocation dynamics configurations onto the CDD continuum fields. The modular structure of the framework makes both directions straightforward to pursue, and they are left for future work.

4.2. Comparison of small- and finite-deformation kinematics in the single-slip simulation

To assess the consistency and numerical performance of the two kinematic descriptions, we compare the small- and finite-deformation frameworks under the same stochastic initialization and loading conditions introduced in Section 3.1, using the case $N_{\mathrm{FR}} = 50$ and the exponential-map update for the finite-deformation formulation. The comparison covers the maximum displacement magnitude

$$\max(\|\mathbf{u}\|) := \max_{\mathbf{X}\in V_0} \|\mathbf{u}_\ell(\mathbf{X}, t)\|,$$

the domain-integrated dislocation density and curvature density,

$$\mathrm{Mass}(\rho) := \int_{V_0} \rho(\mathbf{X}, t)\, \mathrm{d}V_0, \qquad \mathrm{Mass}(q) := \int_{V_0} q(\mathbf{X}, t)\, \mathrm{d}V_0,$$

and the wall-clock times of the force-balance and CDD time integrators, all shown in Fig. 8.

As shown in Fig. 8(a), the two formulations predict similar maximum displacement histories, with deviations largest near the onset of plastic deformation and decreasing as loading proceeds. The integrated dislocation measures in Fig. 8(b) agree closely at early times and diverge gradually, with the small-deformation model consistently predicting slightly smaller values of both $\mathrm{Mass}(\rho)$ and $\mathrm{Mass}(q)$ at later times.

For the computational cost, shown in Figs. 8(c) and 8(d), the small-deformation force-balance solve is significantly cheaper per Newton iteration, reflecting the additional nonlinear couplings introduced by the multiplicative kinematics and the exponential-map update in the finite-deformation formulation. The CDD transport solve is of comparable cost for both formulations.

Overall, the two kinematic descriptions produce qualitatively consistent macroscopic and microstructural responses under identical stochastic initialization. The quantitative differences that do arise can be attributed to the different kinematic descriptions and update procedures in the presence of local heterogeneity, which gives rise to nonuniform deformation and local lattice rotation. The transport velocities and internal fields remain sufficiently close between the two formulations that the predicted dislocation evolution is still in overall agreement, confirming that the finite-deformation framework is consistent with its small-deformation counterpart in this single-slip setting.

4.3. Single-crystal tensile test

We investigate a single-crystal specimen subjected to uniaxial tension for three crystallographic orientations, [010], $[\bar{1}1\bar{1}]$, and $[01\bar{1}]$, aligned with the loading direction, following the setup detailed in Section 3.2. The predictions of the small- and finite-deformation CDD–CP frameworks are compared, and within the finite-deformation setting two local time-integration schemes for $\mathbf{F}_{\mathrm{p}}$ are considered, namely the exponential-map and the backward-Euler scheme. All simulations are performed under identical stochastic initial dislocation distributions so that the influence of the kinematic description and local time-integration strategy can be examined in isolation. All microstructural fields are shown in the reference configuration V_0.

The macroscopic response is characterized by volume-averaged stress and strain over the central region $V_c \subset V_0$ satisfying $100\,\mu\mathrm{m} < y < 300\,\mu\mathrm{m}$, chosen to reduce boundary effects,

$$\bar{\sigma}_{yy} = \frac{1}{|V_c|} \int_{V_c} \sigma_{yy}(\mathbf{X}, \cdot)\, \mathrm{d}V, \qquad \bar{\varepsilon}_{yy} = \frac{1}{|V_c|} \int_{V_c} \varepsilon_{yy}(\mathbf{X}, \cdot)\, \mathrm{d}V.$$

The stress–strain curves for all three orientations are shown in the left column of Fig. 9. The finite-deformation formulations (both exponential-map and backward-Euler) and the small-deformation model exhibit very similar behavior up to approximately 1.2% strain for all loading orientations, and the two finite-deformation integration schemes are essentially indistinguishable over this range. Deviations from the small-deformation formulation remain minor, though slightly more pronounced than in the simple shear case. For loading along [010] (Fig. 9(a)), all models predict monotonic hardening with a mild secondary hardening stage emerging at approximately $\bar{\varepsilon}_{yy} = 0.95\%$. For $[\bar{1}1\bar{1}]$ and $[01\bar{1}]$ (Figs. 9(c) and 9(e)), the stress response exhibits a small overshoot followed by relaxation toward a stable stress level together with modest hardening.

The right column of Fig. 9 shows the temporal evolution of the integrated dislocation density per slip system, $\mathrm{Mass}(\rho^s)$, for each loading orientation. In all cases, the slip systems separate clearly into a predominantly activated group and a less active group, with both kinematic frameworks predicting similar activation sequences at early strains. Differences emerge at larger strains, where the finite-deformation formulation predicts additional activation within the initially less active group due to lattice rotation.

For loading along [010] (Fig. 9(b)), the predominantly activated systems (slip directions 1–4) evolve identically in both frameworks throughout the simulation. Beyond $\bar{\varepsilon}_{yy} \approx 0.8\%$, the small-deformation model predicts stronger activation of direction 6 relative to direction 5, whereas the finite-deformation formulation predicts additional activation in direction 5 as well, coinciding with the onset of secondary hardening at $\bar{\varepsilon}_{yy} \approx 0.95\%$. For loading along $[\bar{1}1\bar{1}]$ (Fig. 9(d)), the predominantly activated directions are 2, 4, and 6, while directions 1, 3, and 5 remain comparatively inactive. The finite-deformation formulation predicts additional activation of slip systems on the D plane from approximately $\bar{\varepsilon}_{yy} \approx 0.75\%$ onward, whereas the small-deformation model preserves the initial separation throughout. For loading along $[01\bar{1}]$ (Fig. 9(f)), the predominantly activated systems are associated with the B and D slip planes, while those on the A and C planes remain less active. Again, the finite-deformation formulation predicts a gradual activation of the initially less active systems from approximately $\bar{\varepsilon}_{yy} \approx 0.75\%$ onward, an effect absent in the small-deformation

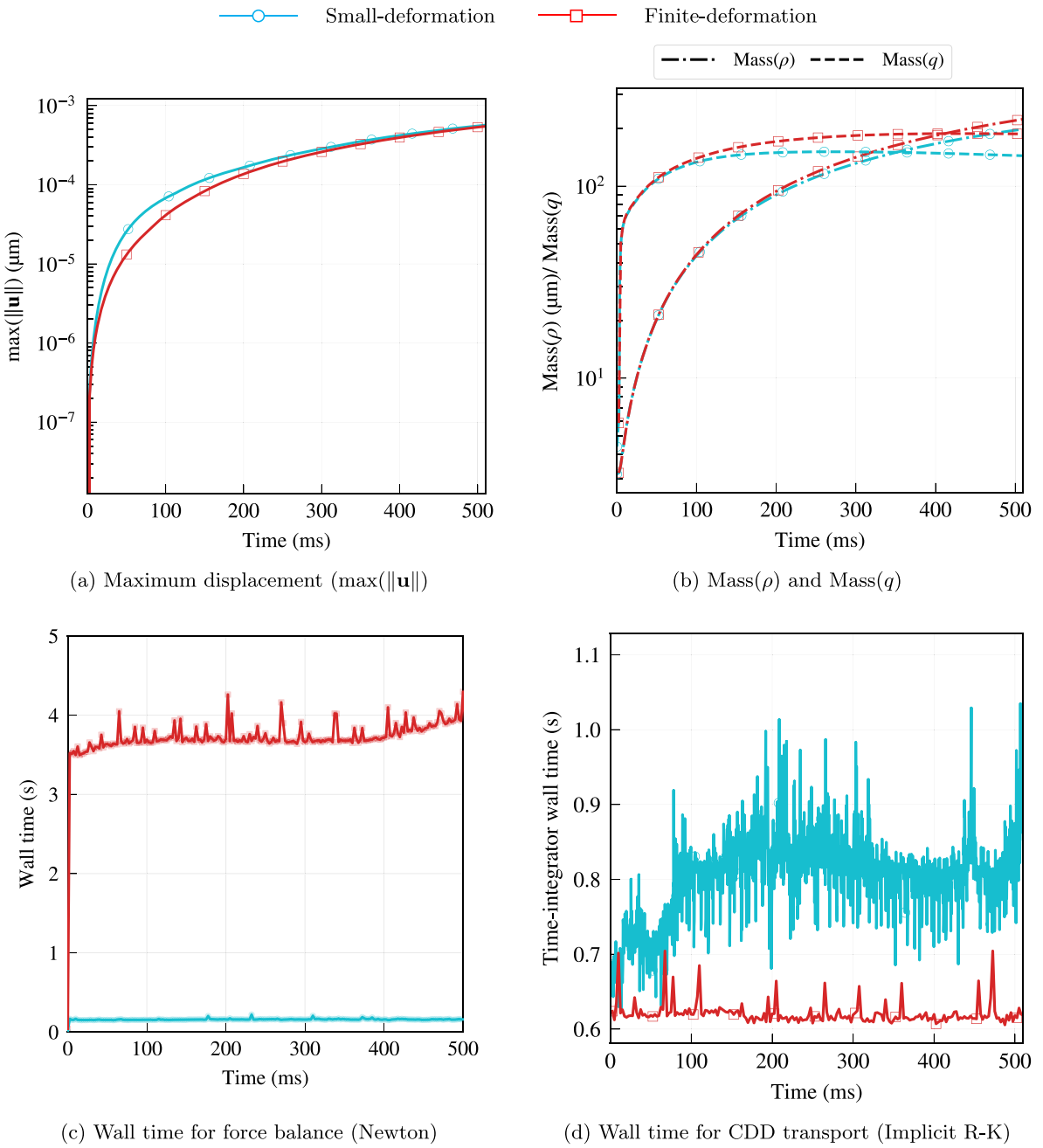

(a) Maximum displacement (max(‖**u**‖))

(b) Mass(ρ) and Mass(q)

(c) Wall time for force balance (Newton)

(d) Wall time for CDD transport (Implicit R-K)

Fig. 8. Comparison of the small- and finite-deformation (exponential-map plastic time integrator) formulations for a single-slip material under simple shear with identical stochastic initialization.

description. In all three orientations, this additional activation is driven by lattice rotation, which modifies the effective Schmid factors and promotes slip activity in systems that would otherwise remain weakly active.

To further illustrate the role of lattice rotation, we examine the spatial distribution of dislocation density and lattice misorientation for the $[\bar{1}1\bar{1}]$ loading case at $\bar{\varepsilon}_{yy} \approx 1\%$, computed with the finite-deformation formulation using the exponential-map update, shown in Fig. 10. The lattice misorientation (Fig. 10(a)) is mainly localized near the specimen corners, attributed to the applied boundary conditions. Three representative types of slip-system behavior are identified. Slip system B2 (Fig. 10(b)), belonging to the predominantly activated group, develops high dislocation density throughout the region of elevated tensile stress. Slip system B3 (Fig. 10(c)), belonging to the less active group, shows almost no dislocation evolution by the end of loading. Slip system D3 (Fig. 10(d)), also initially less active, exhibits a pronounced density increase near the specimen boundaries where lattice misorientation

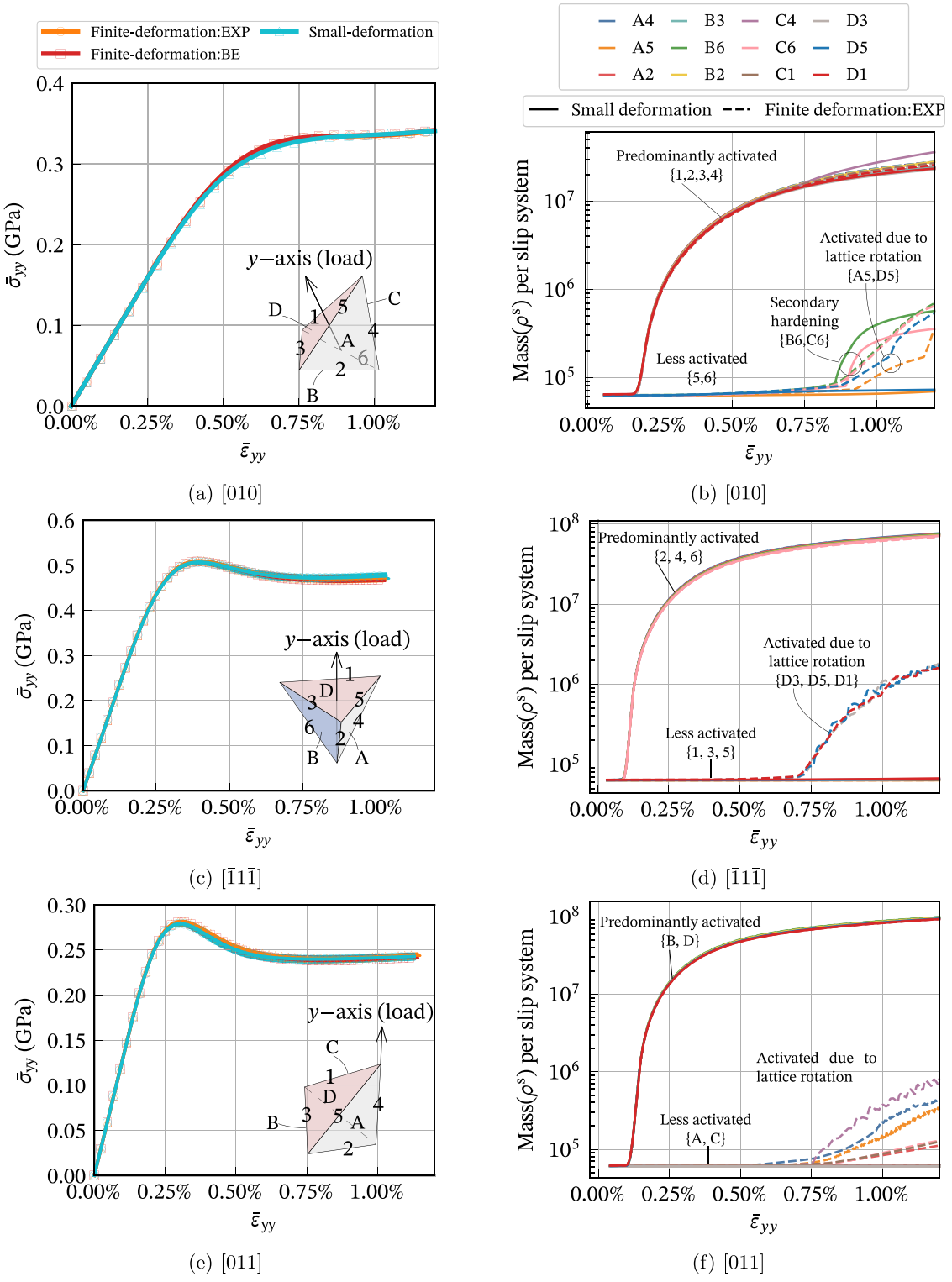

(a) [010] (b) [010]

(c) $[\bar{1}1\bar{1}]$ (d) $[\bar{1}1\bar{1}]$

(e) $[01\bar{1}]$ (f) $[01\bar{1}]$

Fig. 9. Comparison of the small- and finite-deformation CDD–CP formulations in a single-crystal tensile test for different crystallographic loading orientations, using the EXP and BE updates, where EXP denotes the exponential-map update and BE denotes the backward-Euler update. The legend uses the Schmid–Boas notation to label the slip systems as defined in Table 2.

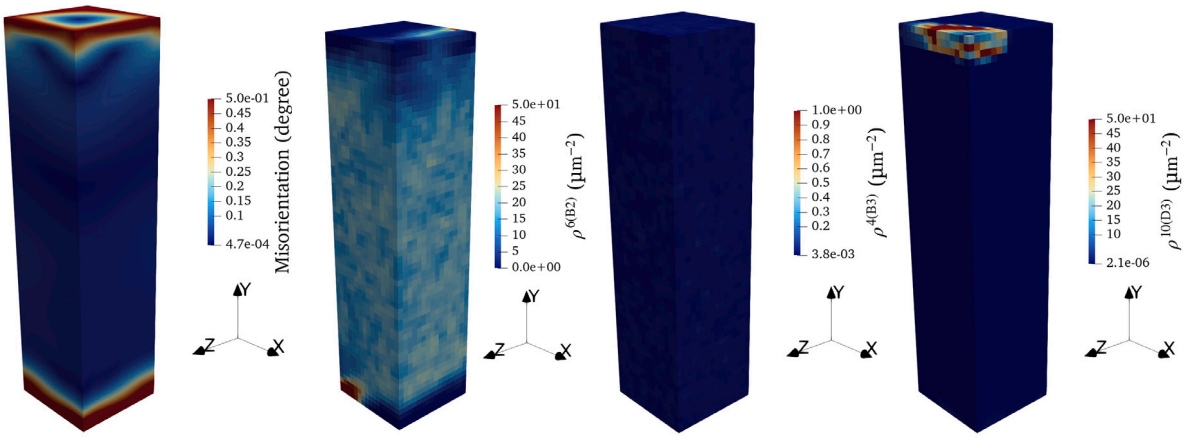

Fig. 10. Microstructural fields for the $[\bar{1}1\bar{1}]$ loading case at $\bar{\varepsilon}_{yy} \approx 1\%$, computed with the finite-deformation formulation using the exponential-map update. (a) Lattice misorientation distribution. (b) Total dislocation density ρ on slip system B2, which is predominantly activated. (c) Dislocation density on slip system B3, which is less activated. (d) Dislocation density on slip system D3, showing localized activation near regions of high lattice misorientation.

is largest, confirming that local lattice rotation promotes activation of slip systems that would otherwise remain weakly active under the prescribed loading direction. The same rotation-driven activation pattern is observed for the other loading orientations, appearing along direction 5 for [010] loading and on the A and C planes for $[01\bar{1}]$ loading.

In summary, the single-crystal tensile simulations show that the small- and finite-deformation CDD–CP frameworks predict very similar macroscopic stress–strain responses for all three loading orientations, and the two finite-deformation integration schemes are essentially indistinguishable in the considered strain range. At the microstructural level, the finite-deformation formulation predicts additional activation of initially weak slip systems at larger strains, driven by local lattice rotation that modifies the effective slip-system alignment and promotes plastic activity in regions that remain less active under the small-deformation description.

4.4. Polycrystalline tensile test

We next investigate the tensile response of a polycrystalline specimen using the small- and finite-deformation CDD–CP frameworks, following the setup detailed in Section 3.2. All comparisons use the exponential-map time integrator for the finite-deformation formulation. The convergence behavior of the backward-Euler scheme is addressed separately in Section 4.5. All dislocation-density and plastic-strain fields are shown in the reference configuration V_0.

The volume-averaged stress–strain curves in Fig. 13(a) reveal clear differences between the small- and finite-deformation models already near the onset of plastic deformation, and these differences persist and grow over the extended strain range up to $\bar{\varepsilon}_{yy} \approx 5\%$. This behavior contrasts with the single-crystal simulations in Section 4.3, where both formulations produce nearly identical macroscopic responses up to at least 1.2% strain and differences emerge only at larger strains through lattice-rotation-driven secondary slip activation. The earlier onset of kinematic differences in the polycrystal is a direct consequence of grain interactions: the geometric incompatibilities between neighboring grains with different crystallographic orientations generate local lattice rotation and plastic heterogeneity from the very beginning of plastic flow, so finite kinematics cannot be treated as a higher-order correction even at small strains. In the single-crystal case, by contrast, lattice rotation is more gradual and spatially uniform at early stages, and kinematic differences only accumulate once global lattice rotation becomes significant.

The broader crystal plasticity literature consistently employs finite-deformation kinematics for polycrystalline simulations, motivated by the need to correctly capture crystallographic texture evolution and lattice rotation under grain interactions. Bronkhorst, Kalidindi and Anand [76] demonstrated that satisfying both compatibility and equilibrium at grain boundaries produces substantially better agreement with experiment, and Miehe, Schröder and Schotte [77] developed a finite-deformation computational homogenization framework that has since become standard for polycrystal texture simulations. As noted by Roters et al. [46], grain boundaries generate GND pile-ups and local stress concentrations from the very onset of plastic flow, as dislocations activated in favorably oriented grains immediately encounter misorientation-induced obstacles at grain interfaces. The finite-deformation formulation accounts for this consistently through the evolving lattice rotation tensor $\mathbf{R}_t$, which continuously updates the Schmid tensors and the rotated elasticity tensor at every loading step, whereas the small-deformation formulation keeps these tensors fixed and therefore cannot capture the feedback between grain-boundary-induced rotation and slip activation regardless of the applied strain magnitude. To our knowledge, the present results provide a first quantitative assessment of this divergence in the context

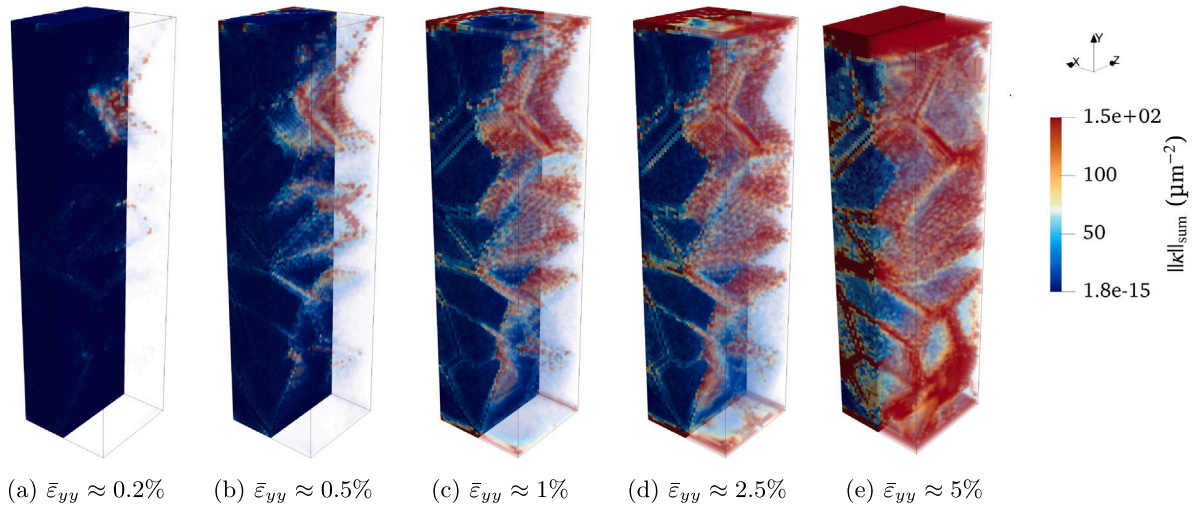

Fig. 11. Evolution of the GND density during the polycrystalline tensile test at different levels of average tensile strain $\bar{\varepsilon}_{yy}$. The plotted quantity is the sum of the norms of the GND vectors over all twelve slip systems. The GND density progressively accumulates along grain boundaries as deformation increases, reflecting plastic incompatibilities between neighboring grains.

of a transport-based CDD–CP framework with explicit dislocation evolution, showing that the two kinematic descriptions separate immediately at the onset of plastic flow in the polycrystalline setting rather than gradually as in the single-crystal case.

The microstructural evidence supporting this picture is provided by the GND density evolution shown in Fig. 11, where the plotted quantity is the sum of the norms of the GND vectors over all twelve slip systems, $\|\boldsymbol{\kappa}\|_{\text{sum}} = \sum_{s=1}^{12} \|\boldsymbol{\kappa}^s\|$. At small strains ($\bar{\varepsilon}_{yy} \approx 0.2\%$), the GND density remains low and begins to emerge near the upper part of the specimen. With increasing deformation, it progressively accumulates along grain boundaries, and at larger strains ($\bar{\varepsilon}_{yy} \approx 2.5\%$ and 5%) a continuous network of elevated GND density develops along grain interfaces, reflecting the growing plastic incompatibilities between neighboring grains.

The accompanying lattice rotation evolution is shown in Fig. 12. The IPF maps in the top row show that in the initial configuration each grain exhibits a nearly uniform color, indicating a spatially constant lattice orientation. As deformation proceeds, color gradients develop within the grains, reflecting heterogeneous plastic deformation, with the strongest orientation gradients near grain boundaries, coinciding with the regions of high GND density in Fig. 11. The pole figures confirm that the initial orientation distribution is approximately random, with the {100}, {110}, and {111} poles approximately uniformly distributed. During deformation, the poles cluster progressively, indicating a growing tendency toward crystallographic texture development, though the overall texture remains relatively weak up to $\bar{\varepsilon}_{yy} \approx 5\%$. Details of the IPF coloring procedure are given in Appendix B.

The spatial distribution of plastic strain at the final deformation state ($\bar{\varepsilon}_{yy} \approx 5\%$) is shown in Figs. 13(b) and 13(c). The small-deformation formulation preserves the initial crystallographic geometry too rigidly, promoting stronger localization of plastic deformation near grain boundaries. The finite-deformation formulation, by contrast, updates the lattice orientations consistently during deformation, allowing slip activity to redistribute as the grains rotate and producing a more diffuse plastic-strain pattern. This difference becomes more pronounced at larger strains, providing a clear visual confirmation of the kinematic divergence identified in the stress–strain curves.

4.5. Performance of local plastic updates

We now examine the iterative performance of the exponential-map and backward-Euler schemes for the local plastic update and the influence of non-convergence on the predicted macroscopic response. The constitutive update follows the formulation introduced in Section 2.1 (see Eq. (14)) and the linearization detailed in Appendix A.3. The analysis is based on the tensile response of a polycrystalline specimen computed with the finite-deformation CDD–CP framework, following the problem setup described in Section 3.2. All spatial distributions of local iteration counts and plastic increment magnitudes are shown in the reference configuration V_0.

Fig. 14(a) reports the percentage of local $\mathbf{F}_{\text{p}}$-updates that converge within one Newton iteration and within at most two iterations when solving Eq. (44), using the same time step $\Delta t = 0.002\,\text{ms}$ for both schemes. Throughout the loading process, both schemes show the same fraction of quadrature points converging in a single iteration. Differences appear once plastic slip becomes active, that the exponential-map update converges within at most two iterations everywhere, whereas the backward-Euler update often requires many more iterations and repeatedly reaches the prescribed cap $k_{\text{loc,max}} = 50$ without satisfying the convergence tolerance. The spatial distributions of local iteration counts at $\bar{\varepsilon}_{yy} \approx 2.5\%$, shown in Figs. 14(b) and 14(c), reveal that the difficult regions occur in similar locations for both schemes, mainly near areas with large lattice rotations induced by boundary condition constraints, grain

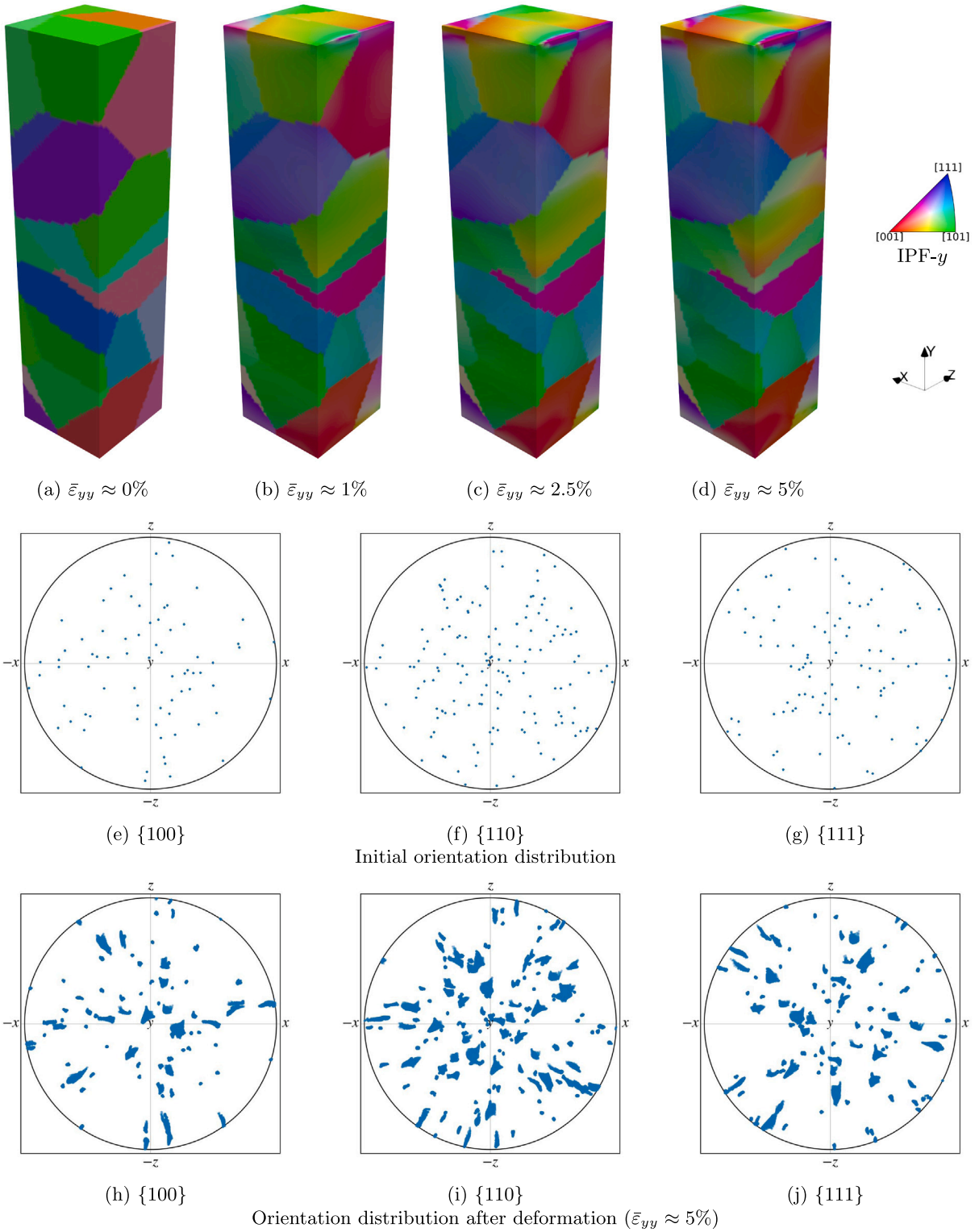

Fig. 12. Evolution of lattice orientation in the polycrystal during tensile deformation predicted by the finite-deformation model with the exponential-map local time integrator. The top row shows IPF maps with respect to the sample y-axis before and after deformation, with the corresponding IPF color key shown on the right. The pole figures show the orientation distribution of the {100}, {110}, and {111} crystal directions for the initial ($\mathbf{R}_0$) and current ($\mathbf{R}_t$) rotation tensor configurations at $\bar{\varepsilon}_{yy} \approx 5\%$.

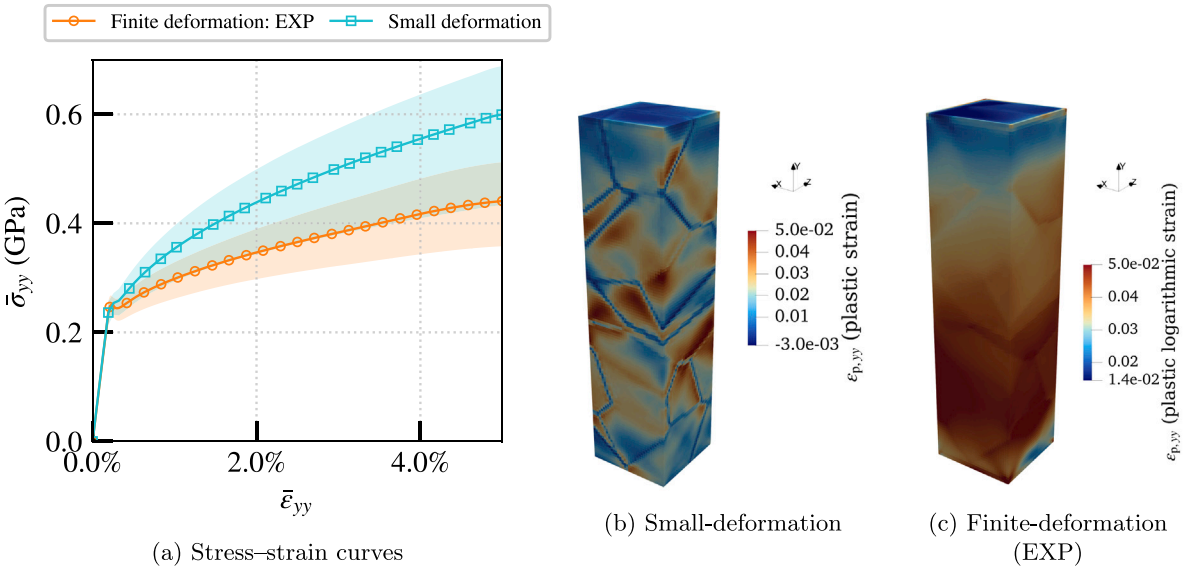

(a) Stress–strain curves (b) Small-deformation (c) Finite-deformation (EXP)

Fig. 13. Polycrystalline tensile response predicted by the small- and finite-deformation CDD–CP formulations using the exponential-map time integrator. (a) Volume-averaged stress–strain curves up to $\bar{\varepsilon}_{yy} \approx 5\%$. (b)–(c) Spatial distribution of the yy-component of plastic strain at the final deformation state at $\bar{\varepsilon}_{yy} \approx 5\%$. The finite-deformation model exhibits a more redistributed plastic-deformation pattern across grain boundaries, whereas the small-deformation formulation shows stronger localization near grain boundaries.

boundaries, or dislocation source nucleation sites. The exponential-map update resolves these regions within two iterations, while the backward-Euler update fails to converge there before reaching the iteration cap.

To relate the local convergence behavior to the magnitude of the plastic update, we compare the iteration-count maps with the incremental plastic velocity-gradient magnitude. For a time step Δt, we define

$$\Delta \mathbf{L}_{\mathrm{p}} := \Delta t\, \mathbf{L}_{\mathrm{p}} = \sum_{s=1}^{12} \Delta \gamma^{s}\, \mathbf{M}_{t}^{s}, \qquad \Delta \gamma^{s} := \Delta t\, \dot{\gamma}^{s},$$

and use its Frobenius norm $\| \Delta \mathbf{L}_{\mathrm{p}} \|$ as a local measure of the plastic increment magnitude. The spatial comparison in Fig. 15 shows that regions requiring many backward-Euler local Newton iterations strongly overlap with regions of large $\| \Delta \mathbf{L}_{\mathrm{p}} \|$. At early strain levels, $\bar{\varepsilon}_{yy} \approx 1\%$ and 2.5%, these regions are mainly localized near grain boundaries and active dislocation source regions. At $\bar{\varepsilon}_{yy} \approx 5\%$, they extend over grains with high plastic deformation.

The difference between the two update schemes can be understood from how they treat large local plastic increments in the multiplicative evolution of $\mathbf{F}_{\mathrm{p}}$. The exponential-map update represents the incremental flow generated by $\mathbf{L}_{\mathrm{p}}$ through $\exp(\Delta t \mathbf{L}_{\mathrm{p}})$, which is consistent with the multiplicative evolution of $\mathbf{F}_{\mathrm{p}}$. The backward-Euler update uses Eq. (14a), which is only a first-order approximation of the exponential flow, and when $\| \Delta \mathbf{L}_{\mathrm{p}} \|$ is large the resulting local nonlinear problem becomes more challenging for Newton's method and may fail to reach the prescribed tolerance within the iteration cap $k_{\mathrm{loc,max}} = 50$. The theoretical advantages of exponential updates for finite-strain plasticity are well established [78,79], and the present results demonstrate their practical relevance in heterogeneous polycrystalline CDD–CP simulations, where grain boundaries, lattice rotation, dislocation source activity, and localized plastic slip generate large spatial variations in the local plastic increment.

In regions where the backward-Euler update reaches the iteration cap without satisfying the convergence tolerance, the returned $\mathbf{F}_{\mathrm{p}}$ should not be regarded as a fully converged local solution, and the resulting stress–strain curve is therefore not used in Section 4.4 as a physical prediction of the backward-Euler scheme. To confirm that the non-convergence is linked to the time-step size rather than to a fundamental limitation of the backward-Euler formula, we performed an additional check with a reduced time step $\Delta t = 0.0002$ ms, one tenth of the main simulation step. With this smaller step, almost all local updates converge within the prescribed iteration limit, with the remaining non-converged quadrature points accounting for approximately 1% of the total and located near boundary regions.

Fig. 16 shows the resulting stress–strain curves as a convergence diagnostic. The reduced-step backward-Euler curve is nearly identical to the exponential-map curve, confirming that the deviation of the large-step backward-Euler run is a numerical artefact of local non-convergence rather than evidence of a physical difference between the two update formulas. The artificially higher stress predicted by the large-step backward-Euler run follows directly from the under-prediction of plastic slip at non-converged quadrature points.

The results of this section should be read as a robustness and practical efficiency assessment for the chosen fixed time-stepping strategy, not as a definitive comparison between the backward-Euler and exponential-map formulas. Under this strategy, the exponential-map scheme converges within at most two local Newton iterations at all quadrature points for $\Delta t = 0.002$ ms and is

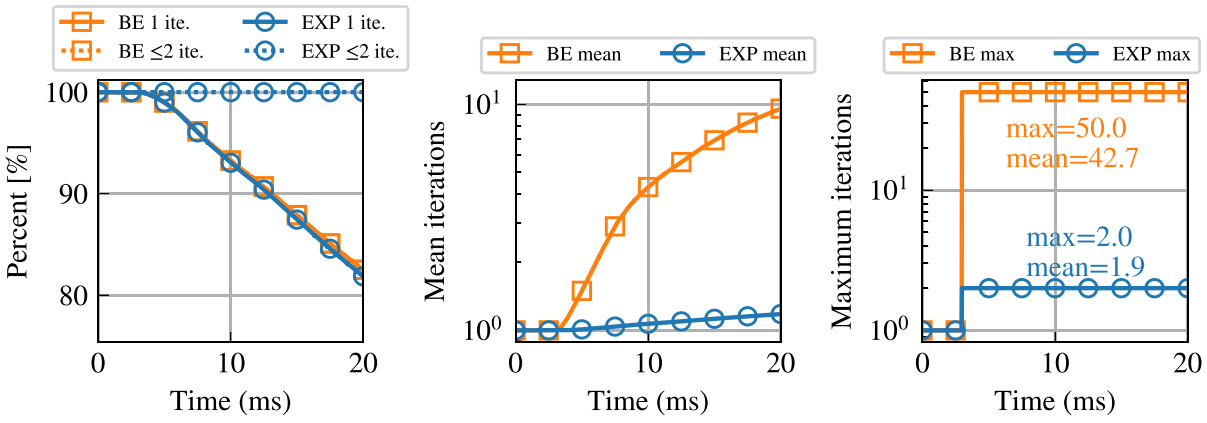

(a) Iteration statistics for the local plastic update.

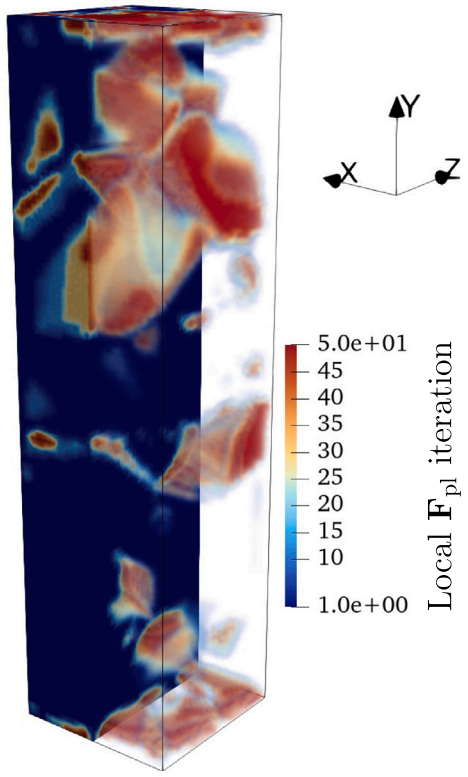

(b) Backward-Euler local update

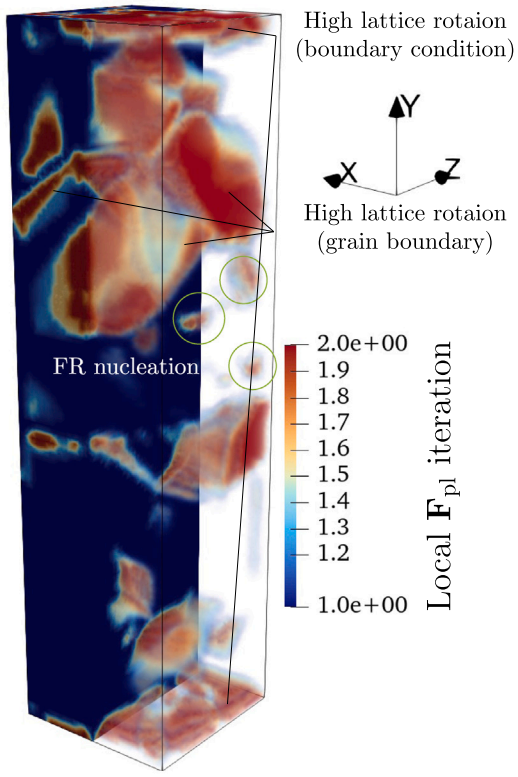

(c) Exponential-map local update

Fig. 14. Iteration behavior of the local plastic update. (a) Percentage of quadrature points converging within one or at most two Newton iterations, together with the mean and maximum iteration counts. (b)–(c) Spatial distribution of local Newton iterations for the backward-Euler and exponential-map updates. Regions requiring multiple iterations coincide with areas of strong lattice rotation, grain boundaries, or dislocation nucleation.

therefore the more robust practical option. The backward-Euler scheme, while cheaper per local update due to its simpler algebraic structure, requires a ten times smaller time step to achieve comparable convergence under the same fixed strategy, increasing the number of global Newton solves and offsetting its per-step cost advantage. A fairer and potentially more efficient backward-Euler implementation would pair it with an adaptive local or global time-step cutback algorithm that selectively reduces the step size only where the local plastic increment is large, avoiding the cost of a globally reduced time step. Such an algorithm could recover the per-step cost advantage of backward-Euler while maintaining convergence in heterogeneous regions, making it a competitive

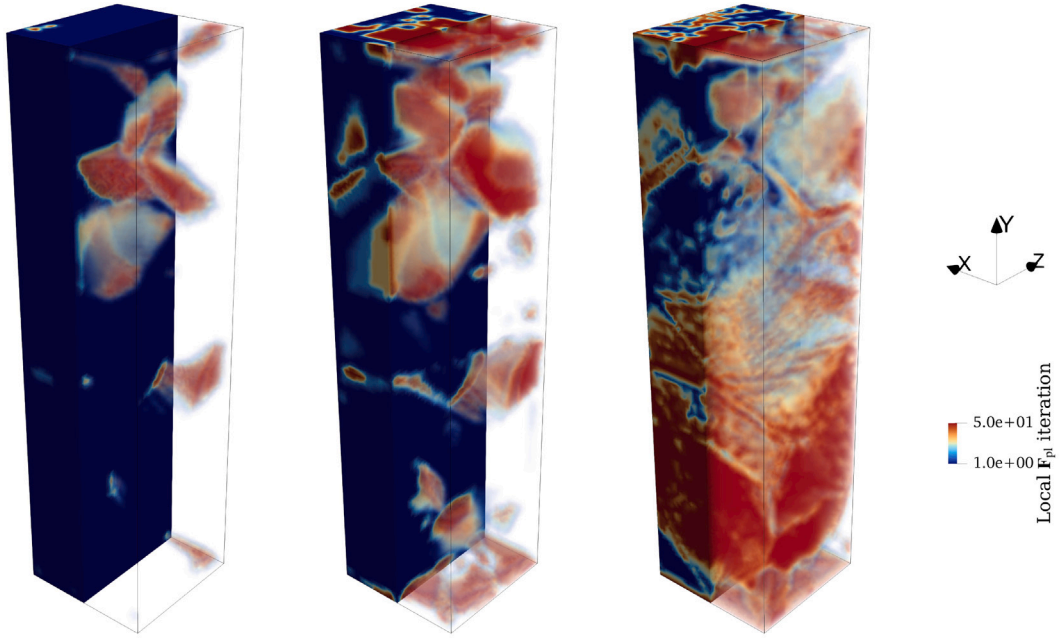

(a) Local iterations $\bar{\varepsilon}_{yy} \approx 1\%$ (b) Local iterations $\bar{\varepsilon}_{yy} \approx 2.5\%$ (c) Local iterations $\bar{\varepsilon}_{yy} \approx 5\%$

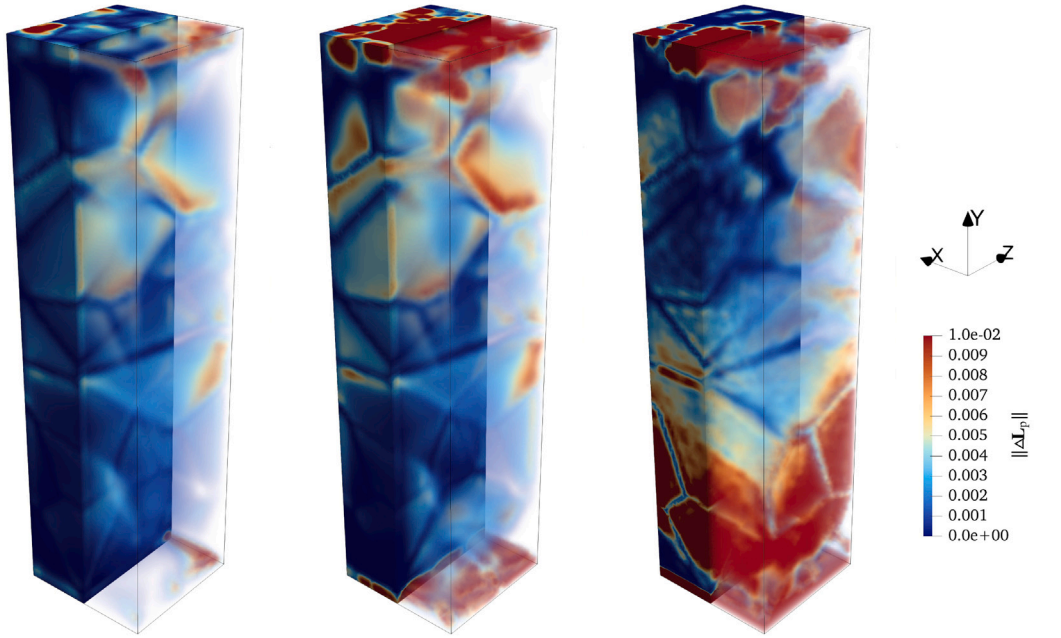

(d) $\| \triangle \mathbf{L}_{\mathrm{p}} \|$ $\bar{\varepsilon}_{yy} \approx 1\%$ (e) $\| \triangle \mathbf{L}_{\mathrm{p}} \|$ $\bar{\varepsilon}_{yy} \approx 2.5\%$ (f) $\| \triangle \mathbf{L}_{\mathrm{p}} \|$ $\bar{\varepsilon}_{yy} \approx 5\%$

Fig. 15. Spatial correlation between backward-Euler local iteration counts and the incremental plastic update magnitude when $\triangle t = 0.002\,\mathrm{ms}$. The top row shows the local Newton iteration count for $\mathbf{F}_{\mathrm{p}}$, and the bottom row shows $\| \triangle \mathbf{L}_{\mathrm{p}} \|$, with $\triangle \mathbf{L}_{\mathrm{p}} = \sum_{s=1}^{12} \Delta\gamma^s \mathbf{M}_t^s$. Regions requiring many iterations or not converged coincide with regions of large $\| \triangle \mathbf{L}_{\mathrm{p}} \|$.

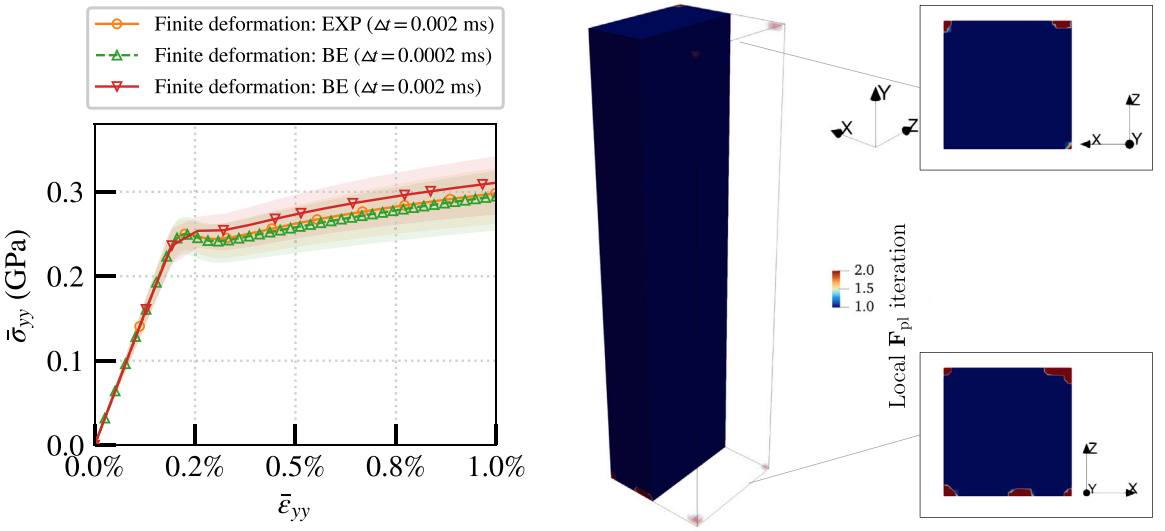

(a) Stress–strain diagnostic (b) Non-converged quadrature points at $\bar{\varepsilon}_{yy} \approx 1\%$

Fig. 16. Convergence diagnostic for the local plastic update. (a) Stress–strain curves for the exponential-map update at $\Delta t = 0.002$ ms, the backward-Euler update at the same time step, and the reduced-step backward-Euler check at $\Delta t = 0.0002$ ms. The reduced-step backward-Euler curve nearly overlaps with the exponential-map curve, whereas the large-step backward-Euler curve gives an artificially higher stress due to under-predicted plastic slip. (b) Locations of the remaining non-converged quadrature points in the reduced-step backward-Euler run at $\bar{\varepsilon}_{yy} \approx 1\%$. These points account for about 1% of all quadrature points and are mainly near boundary regions.

alternative to the exponential-map update. Developing and optimizing such a strategy is beyond the scope of the present work and is left for future study.

4.6. Ensemble variability in stochastic polycrystalline simulations

The polycrystalline simulations discussed above are based on one representative stochastic realization. To demonstrate that the proposed framework can be operated at ensemble scale and to quantify the realization-to-realization variability introduced by microstructural randomness, we consider an ensemble of 64 independent polycrystalline tensile simulations. In each realization, the grain morphology, crystallographic orientations, initial dislocation-density fields, and dislocation source locations are all sampled independently, while the material parameters, loading conditions, numerical discretization, number of grains, prescribed initial dislocation-density level, and total number of dislocation sources are kept fixed as listed in Table 3. Running 64 fully coupled finite-deformation CDD–CP simulations with independent stochastic microstructures demonstrates the scalability of the framework and provides a first quantitative picture of how these combined microstructural uncertainties propagate through the coupled mechanics and dislocation evolution.

The ensemble results are summarized in Fig. 17, where gray curves denote individual realizations and highlighted curves denote ensemble medians. The macroscopic response is characterized by volume-averaged stress and strain over the full reference domain,

$$\bar{\sigma}_{yy} = \frac{1}{|V_0|}\int_{V_0} \sigma_{yy}(\mathbf{X},\cdot)\,\mathrm{d}V_0, \qquad \bar{\varepsilon}_{yy} = \frac{1}{|V_0|}\int_{V_0} \varepsilon_{yy}(\mathbf{X},\cdot)\,\mathrm{d}V_0.$$

The microstructural state is tracked through integrated dislocation measures summed over all 12 FCC slip systems,

$$\mathrm{Mass}(\rho_{\mathrm{tot}}) = \sum_{s=1}^{12}\int_{V_0} \rho^s(\mathbf{X},\cdot)\,\mathrm{d}V_0, \quad \mathrm{Mass}(\kappa_{\mathrm{tot}}) = \sum_{s=1}^{12}\int_{V_0} \|\boldsymbol{\kappa}^s(\mathbf{X},\cdot)\|\,\mathrm{d}V_0, \quad \mathrm{Mass}(|q|_{\mathrm{tot}}) = \sum_{s=1}^{12}\int_{V_0} |q^s(\mathbf{X},\cdot)|\,\mathrm{d}V_0.$$

The macroscopic stress–strain response in Fig. 17(a) shows a visible spread across realizations that is most pronounced in the hardening regime following yield. The scatter in yield stress and subsequent hardening rate reflects the combined effect of grain morphology, crystallographic orientation, and the spatial arrangement of initial dislocation sources, all of which vary independently across realizations. Despite this spread, the ensemble median follows a consistent trend and the qualitative features of the response, including the elastic regime, the onset of plastic flow, and the hardening behavior, are preserved across all realizations.

The integrated dislocation measures in Figs. 17(b) to 17(d) show a similar pattern. The total dislocation density $\mathrm{Mass}(\rho_{\mathrm{tot}})$ and the GND density $\mathrm{Mass}(\kappa_{\mathrm{tot}})$ both increase consistently after the onset of plasticity, with a spread that grows with strain, reflecting the progressive divergence of dislocation transport paths driven by different grain configurations. The curvature measure $\mathrm{Mass}(|q|_{\mathrm{tot}})$ rises sharply in the early loading stage as Frank–Read sources activate, and subsequently exhibits the largest relative

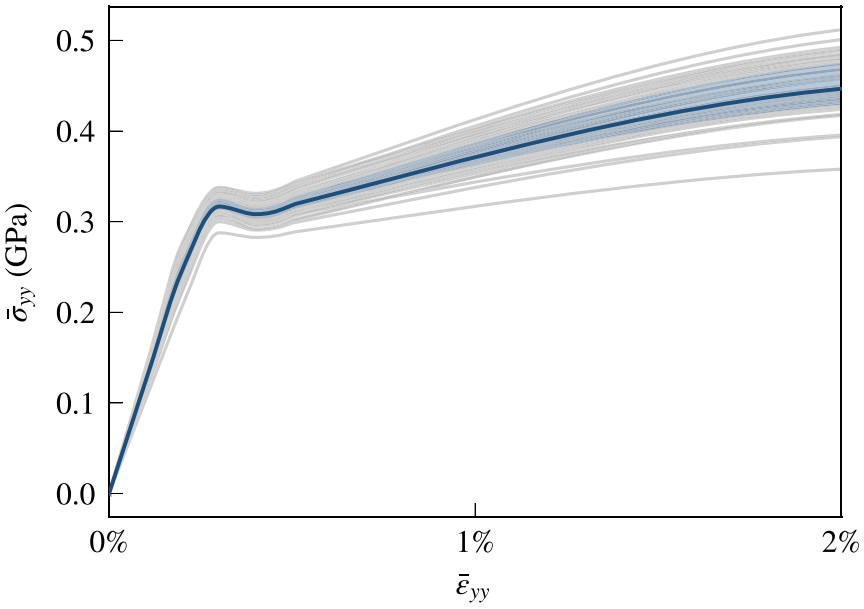

(a) Macroscopic stress–strain response.

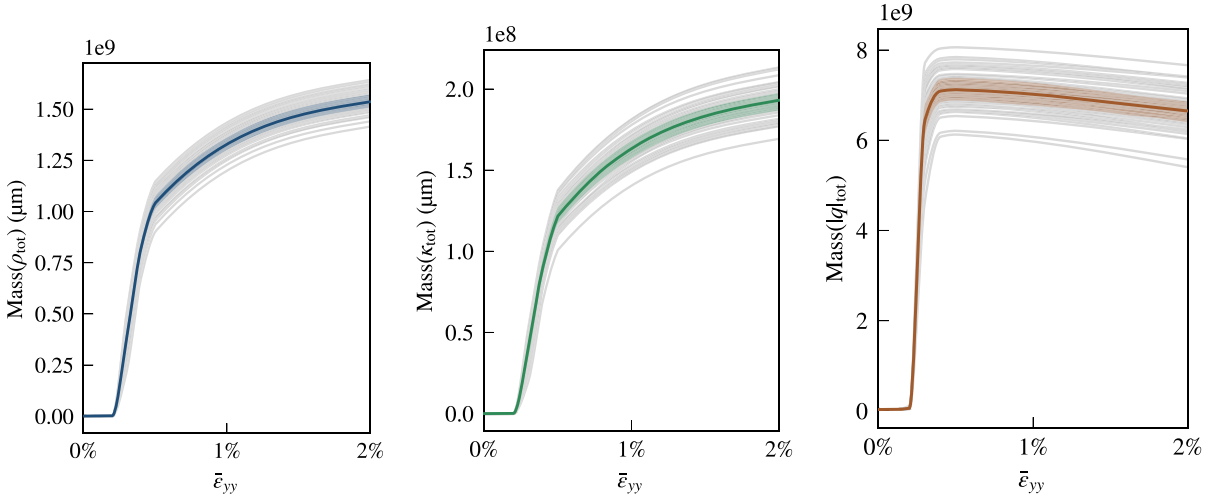

(b) Mass(ρ_{tot}). (c) Mass(κ_{tot}). (d) Mass($|q|_{\mathrm{tot}}$).

Fig. 17. Ensemble variability in the polycrystalline tensile simulations. (a) Macroscopic stress–strain response. (b) Integrated total dislocation density. (c) Integrated GND density. (d) Integrated curvature density. Gray curves denote individual stochastic realizations, and highlighted curves denote ensemble medians over 64 realizations. The dislocation measures are summed over all 12 FCC slip systems.

scatter among the three measures, indicating that the spatial distribution of dislocation sources has a particularly strong influence on the curvature-density evolution. Across all four quantities, the ensemble medians are well-defined and the individual realizations cluster consistently around them, confirming that the observed variability is a genuine reflection of microstructural uncertainty rather than numerical noise.

These results establish that microstructural randomness in grain morphology, crystallographic orientation, initial dislocation distributions, and source locations produces measurable and physically meaningful variability in both the macroscopic mechanical response and the evolving dislocation microstructure. This variability cannot be captured by deterministic single-realization simulations alone, and its quantification requires a framework capable of propagating stochastic microstructural inputs through the full coupled finite-deformation CDD–CP evolution. The present ensemble study represents a first step in this direction, demonstrating that uncertainty-aware dislocation-based crystal plasticity is both computationally feasible and scientifically informative within the proposed framework. The algorithmic infrastructure for more rigorous uncertainty quantification, including multilevel Monte

Carlo, and stochastic gradient descent methods, is available within the M++ platform [40–43] on which the present framework is built, providing a natural path toward statistically converged uncertainty quantification studies with dedicated experimental design, ensemble-size convergence checks, and separation of contributions from individual random inputs. These extensions are left for future work.

5. Conclusion

We presented a stochastic finite-deformation CDD–CP framework coupling finite-strain crystal plasticity with CDD transport for total dislocation density, GND density, and curvature density, with stochastic initial dislocation fields, source distributions, grain morphologies, and crystallographic orientations as inputs. A consistent algorithmic tangent enables robust Newton-based solution under strongly heterogeneous stochastic fields, the CDD equations are discretized by a nodal discontinuous Galerkin method with diagonally implicit Runge–Kutta time integration, and the framework is implemented in M++, whose uncertainty quantification infrastructure provides a natural path toward uncertainty-aware dislocation-based crystal plasticity. The main findings are as follows.

- **Stochastic single-slip microstructure evolution.** Three qualitatively distinct regimes are captured, ranging from boundary-escape-dominated density decay to a quasi-saturated SSD-dominated bulk state controlled by Taylor hardening. The Frank–Read source term enters the CDD transport equations in the same mathematical structure as more complete reaction-kinetics terms, so that annihilation, cross-slip, and junction reactions can be incorporated as natural extensions. Converged solutions are obtained under strongly heterogeneous stochastic initial fields across all source-density regimes.
- **Finite-deformation effects in single crystals.** The two kinematic formulations produce essentially the same macroscopic stress–strain response up to $\bar{\varepsilon}yy \approx 1.2\%$. Differences arise mainly near the specimen boundaries, where the boundary constraints induce lattice rotation and promote additional dislocation activity on initially weak slip systems from approximately $\bar{\varepsilon}yy \approx 0.75\%$ onward. This effect is absent in the small-deformation formulation.
- **Early kinematic divergence in polycrystals.** Grain-boundary constraints and orientation mismatch cause the small- and finite-deformation formulations to separate immediately at the onset of plastic flow and remain separated up to $\bar{\varepsilon}_{yy} \approx 5\%$, in contrast to the gradual divergence in single crystals. This provides a first quantitative assessment of this divergence in a transport-based CDD–CP framework and underscores the necessity of finite kinematics even at conventionally small strains.
- **Robustness of local plastic updates.** The exponential-map update converges within at most two local Newton iterations at all quadrature points, whereas the backward-Euler scheme requires a ten times smaller time step for comparable convergence. A reduced-step diagnostic confirms the backward-Euler deviation is a numerical artefact, and motivates adaptive cutback strategies to recover its per-step cost advantage.
- **Uncertainty-aware dislocation-based crystal plasticity.** An ensemble of 64 stochastic polycrystalline simulations shows that randomness in grain morphology, crystallographic orientation, initial dislocation distributions, and source locations produces measurable variability in both the macroscopic response and evolving dislocation microstructure that deterministic single-realization simulations cannot capture. The solver remains convergent across all realizations, and the ensemble constitutes a first demonstration of uncertainty-aware dislocation-based crystal plasticity in a transport-based CDD–CP setting.

Overall, the framework resolves the coupled feedback among dislocation transport, density-dependent hardening, lattice rotation, and grain-boundary constraints in stochastic heterogeneous microstructures while remaining robust, extensible, and scalable. Future extensions fall naturally into two directions.

On the physical side, the framework should incorporate more complete dislocation reaction kinetics, including annihilation, cross-slip, and junction reactions, as additional source and sink contributions to the CDD evolution equations. Microstructure-dependent source parameters and relaxed initial CDD states informed by discrete dislocation dynamics would further improve the physical fidelity of the stochastic initialization. Grain-boundary conditions beyond the current impenetrability assumption, such as transmission and nucleation at interfaces, are a natural extension for polycrystalline simulations.

On the numerical side, adaptive local or global time-step cutback strategies for the backward-Euler plastic update would recover its per-step cost advantage while maintaining convergence in heterogeneous regions. The ensemble capability of the framework provides a natural basis for uncertainty-aware studies of dislocation-driven plasticity, including sensitivity analysis with respect to microstructural inputs, calibration of continuum dislocation models from higher-resolution data, and optimal-control approaches for microstructure design.

CRediT authorship contribution statement

Sing-Huei Lee: Writing – original draft, Visualization, Software, Methodology, Investigation, Formal analysis, Data curation, Conceptualization. **Adrian Asmund Fessler:** Writing – review & editing, Software, Methodology. **Katrin Schulz:** Writing – review & editing, Validation, Supervision, Project administration, Funding acquisition, Conceptualization.

Declaration of competing interest

The authors declare that they have no known competing financial interests or personal relationships that could have appeared to influence the work reported in this paper.

Acknowledgments

We gratefully acknowledge the financial support of this work in the context of the German Research Foundation (DFG) project SCHU 3074/8-1 and the funding by the Carl-Zeiss-Stiftung. We also thank Dr. Niklas Baumgarten for his contributions and discussions regarding the simulation software.

We further acknowledge the computing time provided on the high-performance computer HoreKa by the National High-Performance Computing Center at KIT (NHR@KIT). This center is jointly supported by the Federal Ministry of Education and Research and the Ministry of Science, Research and the Arts of Baden-Württemberg, as part of the National High-Performance Computing (NHR) joint funding program (https://www.nhr-verein.de/en/our-partners). HoreKa is partly funded by the German Research Foundation (DFG).

Appendix A. Elasto-Viscoplastic consistent tangent operator

In this section, we derive the algorithmic (material) tangent

$$\mathbb{A}_{\mathrm{alg}} = \frac{\partial \mathbf{P}}{\partial \mathbf{F}},$$

which is required in the global Jacobian (Eq. (20)) for the solution of the macroscale force-balance problem in the finite-strain viscoplasticity model.

Throughout the macro-scale Newton iteration, the dislocation-state variables (ρ^s, $\boldsymbol{\kappa}^s$, q^s) are treated as frozen. The elastic second Piola–Kirchhoff stress $\mathbf{S}_{\mathrm{e}}$ is evaluated from $(\mathbf{F}, \mathbf{F}_{\mathrm{p}})$; see Eq. (3). Accordingly, Eq. (2) is interpreted as the composed constitutive mapping

$$\mathbf{P}(\mathbf{F}, \mathbf{F}_{\mathrm{p}}) = \mathbf{F}\mathbf{F}_{\mathrm{p}}^{-1}\, \mathbf{S}_{\mathrm{e}}(\mathbf{F}, \mathbf{F}_{\mathrm{p}})\, \mathbf{F}_{\mathrm{p}}^{-\top}.$$

Since $\mathbf{P}(\mathbf{F}, \mathbf{F}_{\mathrm{p}})$ depends on both arguments, a variation $\delta\mathbf{F}$ affects $\mathbf{P}$ both directly and indirectly through the induced plastic increment $\delta\mathbf{F}_{\mathrm{p}}$. Hence,

$$\delta\mathbf{P} = \underbrace{\left(\frac{\partial \mathbf{P}}{\partial \mathbf{F}}\right)_{\mathbf{F}_{\mathrm{p}}}}_{:=\mathbb{A}_{\mathrm{e}}}[\delta\mathbf{F}] \;+\; \underbrace{\left(\frac{\partial \mathbf{P}}{\partial \mathbf{F}_{\mathrm{p}}}\right)_{\mathbf{F}}}_{:=\mathbb{A}_{\mathrm{p}}}[\delta\mathbf{F}_{\mathrm{p}}]. \tag{28}$$

Here, $\mathbb{A}_{\mathrm{e}}$ denotes the elastic tangent obtained with frozen plastic state, whereas $\mathbb{A}_{\mathrm{p}}$ is the coupling operator describing the sensitivity of $\mathbf{P}$ to variations in $\mathbf{F}_{\mathrm{p}}$ at fixed $\mathbf{F}$. The dependence $\delta\mathbf{F}_{\mathrm{p}}(\delta\mathbf{F})$ follows from the linearization of the local constitutive update, written abstractly as a residual equation $\mathbf{H}(\mathbf{F}, \mathbf{F}_{\mathrm{p}}) = \mathbf{0}$ at each quadrature point.

Linearization of $\mathbf{H}$ with respect to $\mathbf{F}$ and $\mathbf{F}_{\mathrm{p}}$ yields

$$\delta\mathbf{H}(\mathbf{F}, \mathbf{F}_{\mathrm{p}}) = \underbrace{\left(\frac{\partial \mathbf{H}}{\partial \mathbf{F}}\right)_{\mathbf{F}_{\mathrm{p}}}}_{:=\mathbb{H}_{\mathrm{e}}}[\delta\mathbf{F}] \;+\; \underbrace{\left(\frac{\partial \mathbf{H}}{\partial \mathbf{F}_{\mathrm{p}}}\right)_{\mathbf{F}}}_{:=\mathbb{H}_{\mathrm{p}}}[\delta\mathbf{F}_{\mathrm{p}}] = \mathbf{0}. \tag{29}$$

Here, $\mathbb{H}_{\mathrm{e}}$ and $\mathbb{H}_{\mathrm{p}}$ denote the Jacobian blocks of the local residual with respect to $\mathbf{F}$ and $\mathbf{F}_{\mathrm{p}}$, respectively.

Combining Eqs. (28) and (29) gives the coupled linearized system at a quadrature point,

$$\begin{bmatrix} \delta\mathbf{P} \\ \mathbf{0} \end{bmatrix} = \begin{bmatrix} \mathbb{A}_{\mathrm{e}} & \mathbb{A}_{\mathrm{p}} \\ \mathbb{H}_{\mathrm{e}} & \mathbb{H}_{\mathrm{p}} \end{bmatrix} \begin{bmatrix} \delta\mathbf{F} \\ \delta\mathbf{F}_{\mathrm{p}} \end{bmatrix}.$$

From the second row, $\delta\mathbf{F}_{\mathrm{p}}$ can be eliminated as

$$\delta\mathbf{F}_{\mathrm{p}} = -\,\mathbb{H}_{\mathrm{p}}^{-1}\mathbb{H}_{\mathrm{e}}[\delta\mathbf{F}], \tag{30}$$

and substitution into the first row yields the Schur-complement form

$$\boxed{\delta\mathbf{P} = \left[\mathbb{A}_{\mathrm{e}} - \mathbb{A}_{\mathrm{p}}\,\mathbb{H}_{\mathrm{p}}^{-1}\mathbb{H}_{\mathrm{e}}\right][\delta\mathbf{F}] \;=:\; \mathbb{A}_{\mathrm{alg}}[\delta\mathbf{F}].} \tag{31}$$

Thus, $\mathbb{A}_{\mathrm{e}}$ represents the elastic slope at frozen plastic state, whereas the term $\mathbb{A}_{\mathrm{p}}\,\mathbb{H}_{\mathrm{p}}^{-1}\mathbb{H}_{\mathrm{e}}$ accounts for the additional compliance introduced by the local plastic update.

Two rotation-dependent quantities enter this appendix in the current configuration: the sample-frame elasticity tensor $\mathbb{C} = \mathbb{C}(t)$, obtained from the reference tensor $\mathbb{C}_0$ by the current lattice-to-sample rotation $\mathbf{R}_t = \mathbf{Q}\,\mathbf{R}_0$ (Eq. (6)), and the Schmid tensor

$\mathbf{M}^s \equiv \mathbf{M}^s_t = \mathbf{d}^s_t \otimes \mathbf{m}^s_t = \mathbf{R}_t\, \mathbf{M}^s_0\, \mathbf{R}_t^\top$. Both are carried by the same elastic lattice rotation $\mathbf{R}_t$, obtained from the polar decomposition of $\mathbf{F}_e$; the reference quantities $\mathbb{C}_0$, $\{\mathbf{d}^s_0, \mathbf{l}^s_0, \mathbf{m}^s_0\}$, and the Burgers magnitude b^s are fixed. The rotation $\mathbf{R}_t$ is refreshed between time steps and held fixed throughout each macro-scale Newton solve. Within a Newton iteration $\mathbb{C}$ and $\mathbf{M}^s_t$ are therefore independent of $\mathbf{F}$, so that $\delta\mathbb{C} = \mathbf{0}$ and $\delta\mathbf{M}^s_t = \mathbf{0}$ exactly, and $\mathbb{A}_{\text{alg}}$ is the fully consistent tangent of the algorithmic update.

The derivation proceeds in four steps. First, we derive $\mathbb{A}_e$. Second, we derive $\mathbb{A}_p$. Third, we linearize the local constitutive relation $\delta\mathbf{F}_p(\delta\mathbf{F})$ in order to obtain $\mathbb{H}_e$ and $\mathbb{H}_p$. Finally, we solve the local constitutive equation and assemble the consistent tangent $\mathbb{A}_{\text{alg}}$.

A.1. Elastic tangent operator $\mathbb{A}_e$

We now derive the elastic tangent operator acting on a perturbation of the total deformation gradient, $\mathbb{A}_e[\delta\mathbf{F}]$, i.e. the first term in Eq. (28) (equivalently, the first term in Eq. (31)).

We recall the stress relations defined in Section 2.1:

$$\mathbf{P} = \mathbf{F}\,\mathbf{F}_p^{-1}\,\mathbf{S}_e\,\mathbf{F}_p^{-\top}, \qquad \mathbf{S}_e = \mathbb{C} : \mathbf{E}_e, \qquad \mathbf{E}_e = \tfrac{1}{2}(\mathbf{C}_e - \mathbf{I}),$$

where $\mathbf{C}_e$ is the elastic right Cauchy–Green tensor $\mathbf{C}_e = \mathbf{F}_e^\top\mathbf{F}_e = \mathbf{F}_p^{-\top}\,\mathbf{F}^\top\mathbf{F}\,\mathbf{F}_p^{-1}$.

Holding $\mathbf{F}_p$ fixed, the variation of $\mathbf{P}$ induced by $\delta\mathbf{F}$ is

$$\mathbb{A}_e[\delta\mathbf{F}] := \delta\mathbf{P}\Big|_{\mathbf{F}_p} = (\delta\mathbf{F})\,\mathbf{F}_p^{-1}\,\mathbf{S}_e\,\mathbf{F}_p^{-\top} \;+\; \mathbf{F}\,\mathbf{F}_p^{-1}\,(\delta\mathbf{S}_e)\Big|_{\mathbf{F}_p}\,\mathbf{F}_p^{-\top}. \tag{32}$$

The variation of $\mathbf{S}_e$ induced by $\delta\mathbf{F}$ with $\mathbf{F}_p$ can be written as

$$\delta\mathbf{S}_e\Big|_{\mathbf{F}_p} = \tfrac{1}{2}\,\mathbb{C} : \delta\mathbf{C}_e\Big|_{\mathbf{F}_p}. \tag{33}$$

And the variation of $\mathbf{C}_e$ is

$$\delta\mathbf{C}_e\Big|_{\mathbf{F}_p} = \mathbf{F}_p^{-\top}\Big((\delta\mathbf{F})^\top\mathbf{F} + \mathbf{F}^\top(\delta\mathbf{F})\Big)\mathbf{F}_p^{-1}. \tag{34}$$

Here, we introduce the symmetric mapping operator

$$\boldsymbol{\Phi}_F[\delta\mathbf{F}] := \tfrac{1}{2}\,\mathbf{F}_p^{-\top}\Big((\delta\mathbf{F})^\top\mathbf{F} + \mathbf{F}^\top(\delta\mathbf{F})\Big)\mathbf{F}_p^{-1}, \tag{35}$$

so that Eqs. (33) and (34) imply

$$\delta\mathbf{S}_e\Big|_{\mathbf{F}_p} = \mathbb{C} : \boldsymbol{\Phi}_F[\delta\mathbf{F}]. \tag{36}$$

Substituting Eq. (36) into Eq. (32) gives

$$\boxed{\mathbb{A}_e[\delta\mathbf{F}] = (\delta\mathbf{F})\,\mathbf{F}_p^{-1}\,\mathbf{S}_e\,\mathbf{F}_p^{-\top} + \mathbf{F}\,\mathbf{F}_p^{-1}\,\big(\mathbb{C} : \boldsymbol{\Phi}_F[\delta\mathbf{F}]\big)\,\mathbf{F}_p^{-\top}} \tag{37}$$

with $\boldsymbol{\Phi}_F$ defined in Eq. (35).

A.2. Plastic-state coupling operator $\mathbb{A}_p$

We now derive the plastic-state coupling operator acting on a perturbation of the plastic deformation gradient, $\mathbb{A}_p[\delta\mathbf{F}_p]$, i.e. the second term in Eq. (28) (equivalently, the second term in Eq. (31)).

We start from recalling the definition in Section 2.1:

$$\mathbf{P} = \mathbf{F}\,\mathbf{F}_p^{-1}\,\mathbf{S}_e\,\mathbf{F}_p^{-\top}, \qquad \mathbf{S}_e = \mathbb{C} : \mathbf{E}_e, \qquad \mathbf{E}_e = \tfrac{1}{2}(\mathbf{C}_e - \mathbf{I}), \tag{38}$$

where the elastic right Cauchy–Green tensor is

$$\mathbf{C}_e := \mathbf{F}_e^\top\mathbf{F}_e = \mathbf{F}_p^{-\top}\,\mathbf{C}\,\mathbf{F}_p^{-1}, \qquad \mathbf{C} := \mathbf{F}^\top\mathbf{F}.$$

Throughout this subsection, $\mathbf{F}$ is held fixed, so $\mathbf{C}$ is constant. We use the standard differential identities for the inverse and inverse transpose of a second-order tensor:

$$\delta(\mathbf{F}_p^{-1}) = -\,\mathbf{F}_p^{-1}\,\delta\mathbf{F}_p\,\mathbf{F}_p^{-1}, \qquad \delta(\mathbf{F}_p^{-\top}) = -\,\mathbf{F}_p^{-\top}\,(\delta\mathbf{F}_p)^\top\,\mathbf{F}_p^{-\top}.$$

They follow from differentiating $\mathbf{F}_p\,\mathbf{F}_p^{-1} = \mathbf{I}$ and $(\mathbf{F}_p^{-1})^\top = \mathbf{F}_p^{-\top}$, respectively.

By definition, $\mathbb{A}_p[\delta\mathbf{F}_p] := \delta\mathbf{P}\big|_{\mathbf{F}}$. Using (38) and the identities above, we obtain

$$\begin{aligned}\mathbb{A}_p[\delta\mathbf{F}_p] = \delta\mathbf{P}\big|_{\mathbf{F}} &= \mathbf{F}\,\delta(\mathbf{F}_p^{-1})\,\mathbf{S}_e\,\mathbf{F}_p^{-\top} \;+\; \mathbf{F}\,\mathbf{F}_p^{-1}\,(\delta\mathbf{S}_e)\big|_{\mathbf{F}}\,\mathbf{F}_p^{-\top} \;+\; \mathbf{F}\,\mathbf{F}_p^{-1}\,\mathbf{S}_e\,\delta(\mathbf{F}_p^{-\top}) \\ &= -\,\mathbf{F}\,\mathbf{F}_p^{-1}\,\delta\mathbf{F}_p\,\mathbf{F}_p^{-1}\,\mathbf{S}_e\,\mathbf{F}_p^{-\top} \;+\; \mathbf{F}\,\mathbf{F}_p^{-1}\,(\delta\mathbf{S}_e)\big|_{\mathbf{F}}\,\mathbf{F}_p^{-\top} \;-\; \mathbf{F}\,\mathbf{F}_p^{-1}\,\mathbf{S}_e\,\mathbf{F}_p^{-\top}\,(\delta\mathbf{F}_p)^{\top}\,\mathbf{F}_p^{-\top}.\end{aligned} \tag{39}$$

To compute the second term in Eq. (39), we write $(\delta\mathbf{S}_e)\big|_{\mathbf{F}}$ as

$$\delta\mathbf{S}_e\big|_{\mathbf{F}} = \mathbb{C} : \delta\mathbf{E}_e\big|_{\mathbf{F}} = \tfrac{1}{2}\,\mathbb{C} : \delta\mathbf{C}_e\big|_{\mathbf{F}}. \tag{40}$$

Then we differentiate $\mathbf{C}_e = \mathbf{F}_p^{-\top}\mathbf{C}\mathbf{F}_p^{-1}$ with respect to $\mathbf{F}_p$ (at fixed $\mathbf{C}$), we obtain

$$\begin{aligned}\delta\mathbf{C}_e\big|_{\mathbf{F}} &= \delta(\mathbf{F}_p^{-\top})\,\mathbf{C}\,\mathbf{F}_p^{-1} \;+\; \mathbf{F}_p^{-\top}\,\mathbf{C}\,\delta(\mathbf{F}_p^{-1}) \\ &= -\,\mathbf{F}_p^{-\top}\,(\delta\mathbf{F}_p)^{\top}\,\mathbf{F}_p^{-\top}\,\mathbf{C}\,\mathbf{F}_p^{-1} \;-\; \mathbf{F}_p^{-\top}\,\mathbf{C}\,\mathbf{F}_p^{-1}\,\delta\mathbf{F}_p\,\mathbf{F}_p^{-1} \\ &= -\,\mathbf{F}_p^{-\top}(\delta\mathbf{F}_p)^{\top}\,\mathbf{C}_e \;-\; \mathbf{C}_e\,\delta\mathbf{F}_p\,\mathbf{F}_p^{-1}.\end{aligned}$$

To collect the $\delta\mathbf{F}_p$-dependence, we introduce the symmetric mapping operator

$$\boldsymbol{\Phi}_P[\delta\mathbf{F}_p] := \tfrac{1}{2}\,\delta\mathbf{C}_e\big|_{\mathbf{F}} = -\,\tfrac{1}{2}\Big(\mathbf{F}_p^{-\top}\,(\delta\mathbf{F}_p)^{\top}\,\mathbf{C}_e + \mathbf{C}_e\,\delta\mathbf{F}_p\,\mathbf{F}_p^{-1}\Big). \tag{41}$$

Inserting Eq. (41) into Eq. (40) yields

$$\delta\mathbf{S}_e\big|_{\mathbf{F}} = \mathbb{C} : \boldsymbol{\Phi}_P[\delta\mathbf{F}_p]. \tag{42}$$

Finally, substituting Eq. (42) into Eq. (39) gives

$$\boxed{\begin{aligned}\mathbb{A}_p[\delta\mathbf{F}_p] &= \delta\mathbf{P}\big|_{\mathbf{F}} \\ &= -\,\mathbf{F}\,\mathbf{F}_p^{-1}\,\delta\mathbf{F}_p\,\mathbf{F}_p^{-1}\,\mathbf{S}_e\,\mathbf{F}_p^{-\top} \;+\; \mathbf{F}\,\mathbf{F}_p^{-1}\,\big(\mathbb{C} : \boldsymbol{\Phi}_P[\delta\mathbf{F}_p]\big)\,\mathbf{F}_p^{-\top} \;-\; \mathbf{F}\,\mathbf{F}_p^{-1}\,\mathbf{S}_e\,\mathbf{F}_p^{-\top}\,(\delta\mathbf{F}_p)^{\top}\,\mathbf{F}_p^{-\top}.\end{aligned}} \tag{43}$$

A.3. Linearization of the local constitutive relationship

At each quadrature point, the plastic state $\mathbf{F}_p$ is obtained from an implicit time-discrete update (see Section 2.1). Consequently, in the global Newton linearization, a variation of the deformation gradient $\delta\mathbf{F}$ induces a compatible variation $\delta\mathbf{F}_p$ through the local constitutive constraint. The purpose of this subsection is to linearize this local constitutive relationship, identify the Jacobian blocks $\mathbb{H}_e$ and $\mathbb{H}_p$, and thereby provide the local relation needed for Schur-complement condensation in the algorithmic tangent construction (see Eq. (30)).

Following Section 2.1, we consider the finite-strain, rate-dependent flow $\dot{\mathbf{F}}_p = \mathbf{L}_p\,\mathbf{F}_p$, where $\mathbf{L}_p$ is determined by the CDD slip kinetics. Over a time increment $\triangle t$, the update is enforced by solving, at each quadrature point, the nonlinear local residual equation

$$\mathbf{H}(\mathbf{F}, \mathbf{F}_p) := \mathbf{F}_p - \mathcal{H}_{\Delta t}\Big(\mathbf{L}_p\big(\mathbf{S}_e(\mathbf{F}, \mathbf{F}_p)\big)\Big)\,\mathbf{F}_p^{\text{old}} = \mathbf{0}. \tag{44}$$

Here $\mathcal{H}_{\Delta t}(\cdot)$ denotes the update map associated with the chosen time integration scheme for $\mathbf{F}_p$. In the macro Newton iteration, the dislocation state variables (e.g. ρ^s, $\boldsymbol{\kappa}^s$, q^s) are held fixed. However, the elastic stress $\mathbf{S}_e$ is recomputed from $(\mathbf{F}, \mathbf{F}_p)$ via the elastic law Eq. (3). As a result, $\mathbf{L}_p$ depends on both $\mathbf{F}$ and $\mathbf{F}_p$ through $\mathbf{S}_e(\mathbf{F}, \mathbf{F}_p)$, which is the source of the local coupling between $\delta\mathbf{F}$ and $\delta\mathbf{F}_p$.

Linearizing $\mathbf{H}$ with respect to $\mathbf{F}$ and $\mathbf{F}_p$ yields the two Jacobian blocks $\mathbb{H}_e$ and $\mathbb{H}_p$ of the local residual with respect to $\mathbf{F}$ and $\mathbf{F}_p$, respectively (see Eq. (29)). We next detail the derivation of $\mathbb{H}_e$ and $\mathbb{H}_p$ for two common choices of the update map $\mathcal{H}_{\Delta t}$ as discussed in Section 2.1.

Backward Euler. For the backward-Euler scheme we introduce $\mathbf{X} := \mathbf{I} - \triangle t\,\mathbf{L}_p$ and set $\mathcal{H}_{\Delta t}^{\text{BE}} := \mathbf{X}^{-1}$, so that the local residual reads

$$\mathbf{H}^{\text{BE}}(\mathbf{F}, \mathbf{F}_p) := \mathbf{F}_p - (\mathbf{I} - \triangle t\,\mathbf{L}_p)^{-1}\,\mathbf{F}_p^{\text{old}} = \mathbf{0}. \tag{45}$$

Using $\delta(\mathbf{X}^{-1}) = -\mathbf{X}^{-1}(\delta\mathbf{X})\mathbf{X}^{-1}$ together with $\delta\mathbf{X} = -\,\triangle t\,\delta\mathbf{L}_p$ yields

$$\delta\mathcal{H}_{\Delta t}^{\text{BE}} = \mathcal{H}_{\Delta t}^{\text{BE}}\,(\triangle t\,\delta\mathbf{L}_p)\,\mathcal{H}_{\Delta t}^{\text{BE}}.$$

Substitution into $\delta\mathbf{H}^{\text{BE}}$ gives

$$\delta\mathbf{H}^{\text{BE}} = \delta\mathbf{F}_p - \mathcal{H}_{\Delta t}^{\text{BE}}\,(\triangle t\,\delta\mathbf{L}_p)\,\mathcal{H}_{\Delta t}^{\text{BE}}\,\mathbf{F}_p^{\text{old}},$$

and therefore the Jacobian blocks are

$$\mathbb{H}_{\mathrm{e}}[\delta\mathbf{F}] = -\,\mathcal{H}^{\mathrm{BE}}_{\Delta t}\big(\Delta t\,\delta\mathbf{L}_{\mathrm{p}}[\delta\mathbf{F}]\big)\,\mathcal{H}^{\mathrm{BE}}_{\Delta t}\,\mathbf{F}^{\mathrm{old}}_{\mathrm{p}}, \tag{46a}$$

$$\mathbb{H}_{\mathrm{p}}[\delta\mathbf{F}_{\mathrm{p}}] = \delta\mathbf{F}_{\mathrm{p}} - \mathcal{H}^{\mathrm{BE}}_{\Delta t}\big(\Delta t\,\delta\mathbf{L}_{\mathrm{p}}[\delta\mathbf{F}_{\mathrm{p}}]\big)\,\mathcal{H}^{\mathrm{BE}}_{\Delta t}\,\mathbf{F}^{\mathrm{old}}_{\mathrm{p}}. \tag{46b}$$

Exponential map. For the exponential update $\mathcal{H}^{\exp}_{\Delta t} := \exp(\Delta t\,\mathbf{L}_{\mathrm{p}})$ the residual is

$$\mathbf{H}^{\exp}(\mathbf{F},\mathbf{F}_{\mathrm{p}}) := \mathbf{F}_{\mathrm{p}} - \exp(\Delta t\,\mathbf{L}_{\mathrm{p}})\,\mathbf{F}^{\mathrm{old}}_{\mathrm{p}} = \mathbf{0}. \tag{47}$$

With the Fréchet derivative $D\exp_{\mathbf{A}}[\mathbf{Z}]$ and the shorthand $\mathcal{E}_{\mathbf{L}_{\mathrm{p}}}[\cdot] := D\exp_{\Delta t\mathbf{L}_{\mathrm{p}}}[\Delta t(\cdot)]$ (cf. [51, B.2], [80]), we obtain

$$\delta\mathbf{H}^{\exp} = \delta\mathbf{F}_{\mathrm{p}} - \mathcal{E}_{\mathbf{L}_{\mathrm{p}}}[\delta\mathbf{L}_{\mathrm{p}}]\,\mathbf{F}^{\mathrm{old}}_{\mathrm{p}},$$

and hence

$$\mathbb{H}_{\mathrm{e}}[\delta\mathbf{F}] = -\,\mathcal{E}_{\mathbf{L}_{\mathrm{p}}}\big(\delta\mathbf{L}_{\mathrm{p}}[\delta\mathbf{F}]\big)\,\mathbf{F}^{\mathrm{old}}_{\mathrm{p}}, \tag{48a}$$

$$\mathbb{H}_{\mathrm{p}}[\delta\mathbf{F}_{\mathrm{p}}] = \delta\mathbf{F}_{\mathrm{p}} - \mathcal{E}_{\mathbf{L}_{\mathrm{p}}}\big(\delta\mathbf{L}_{\mathrm{p}}[\delta\mathbf{F}_{\mathrm{p}}]\big)\,\mathbf{F}^{\mathrm{old}}_{\mathrm{p}}. \tag{48b}$$

Finally, we linearize $\mathbf{L}_{\mathrm{p}}$ through the slip kinetics. Recall

$$\mathbf{L}_{\mathrm{p}} = \sum_{s=1}^{S'} \dot\gamma^{s}\,\mathbf{M}^{s}, \qquad \dot\gamma^{s} = v^{s}\,b^{s}\,\rho^{s}, \qquad \tau^{s} = \mathbf{S}_{\mathrm{e}} : \mathbf{M}^{s} + \tau^{s}_{\mathrm{int}}.$$

In this local linearization, we treat ρ^{s} and τ^{s}_{int} as frozen. For slip systems that remain active during the increment, the Perzyna form implies

$$\delta\dot\gamma^{s} = \frac{1}{\eta^{s}}\,(\delta\mathbf{S}_{\mathrm{e}} : \mathbf{M}^{s}),$$

with $1/\eta^{s} = (b^{s})^{2}\rho^{s}/B$. Since $\mathbf{M}^{s}_{t}$ is held fixed during the Newton solve, $\delta\mathbf{M}^{s}_{t} = \mathbf{0}$, and we obtain

$$\delta\mathbf{L}_{\mathrm{p}} = \sum_{s}^{S'} \frac{1}{\eta^{s}}(\delta\mathbf{S}_{\mathrm{e}} : \mathbf{M}^{s})\,\mathbf{M}^{s} =: \mathbb{G} : \delta\mathbf{S}_{\mathrm{e}}, \qquad \mathbb{G} := \sum_{s}^{S'} \frac{1}{\eta^{s}}\,\mathbf{M}^{s}\otimes\mathbf{M}^{s}. \tag{49}$$

Using the previously derived decompositions $\delta\mathbf{S}_{\mathrm{e}}\big|_{\mathbf{F}_{\mathrm{p}}} = \mathbb{C} : \boldsymbol{\Phi}_{\mathrm{F}}[\delta\mathbf{F}]$ and $\delta\mathbf{S}_{\mathrm{e}}\big|_{\mathbf{F}} = \mathbb{C} : \boldsymbol{\Phi}_{\mathrm{P}}[\delta\mathbf{F}_{\mathrm{p}}]$, we write

$$\delta\mathbf{S}_{\mathrm{e}} = \mathbb{C} : \boldsymbol{\Phi}_{\mathrm{F}}[\delta\mathbf{F}] + \mathbb{C} : \boldsymbol{\Phi}_{\mathrm{P}}[\delta\mathbf{F}_{\mathrm{p}}]. \tag{50}$$

Inserting Eq. (50) into Eq. (49) and defining $\mathbb{J} := \mathbb{G} : \mathbb{C}$ yields

$$\delta\mathbf{L}_{\mathrm{p}} = \mathbb{J} : \boldsymbol{\Phi}_{\mathrm{F}}[\delta\mathbf{F}] \;+\; \mathbb{J} : \boldsymbol{\Phi}_{\mathrm{P}}[\delta\mathbf{F}_{\mathrm{p}}]. \tag{51}$$

Substituting Eq. (51) into the expressions for $\mathbb{H}_{\mathrm{e}}$ and $\mathbb{H}_{\mathrm{p}}$ yields the linearized local system

$$\mathbb{H}_{\mathrm{p}}[\delta\mathbf{F}_{\mathrm{p}}] = -\,\mathbb{H}_{\mathrm{e}}[\delta\mathbf{F}].$$

Solving this system at each quadrature point expresses $\delta\mathbf{F}_{\mathrm{p}}$ in terms of $\delta\mathbf{F}$ and enables the Schur-complement condensation in Eq. (31).

A.4. Local constitutive solve for $\mathbf{F}_{\mathrm{p}}$ at a quadrature point

At each iteration step k of the global Newton iteration, and at each quadrature point, the total deformation gradient $\mathbf{F}$ is known (from the current trial displacement), while the plastic state $\mathbf{F}_{\mathrm{p}}$ is updated by solving the time-discrete constitutive constraint $\mathbf{H}(\mathbf{F},\mathbf{F}_{\mathrm{p}}) = \mathbf{0}$ (cf. Eq. (44)) with a local Newton method. The dislocation-state variables are frozen during the global Newton step. The choice of the time-integration map $\mathcal{H}_{\Delta t}$ (backward-Euler or exponential-map, see Appendix A.3) only affects the residual evaluation and the Jacobians for the local Newton method. The local solution procedure is identical.

Given $\mathbf{F}$ and a current local iterate $\mathbf{F}_{\mathrm{p}}$, we evaluate $\mathbf{H}(\mathbf{F},\mathbf{F}_{\mathrm{p}})$ and the Jacobian blocks $\mathbb{H}_{\mathrm{e}} = \partial\mathbf{H}/\partial\mathbf{F}$ and $\mathbb{H}_{\mathrm{p}} = \partial\mathbf{H}/\partial\mathbf{F}_{\mathrm{p}}$ derived in Appendix A.3 at each quadrature point:

- For BE, use Eqs. (45), (46a) and (46b).
- For EXP, use Eqs. (47), (48a) and (48b).

In both cases, the linearization of $\mathbf{L}_\mathrm{p}$ enters only through Eq. (51), i.e. $\delta\mathbf{L}_\mathrm{p} = \mathbb{J} : \boldsymbol{\Phi}_\mathrm{F}[\delta\mathbf{F}] + \mathbb{J} : \boldsymbol{\Phi}_\mathrm{P}[\delta\mathbf{F}_\mathrm{p}]$ with $\mathbb{J} = \mathbb{G} : \mathbb{C}$ as defined previously. The local Newton update solves

$$\mathbb{H}_\mathrm{p}[\Delta\mathbf{F}_\mathrm{p}] = -\mathbf{H}(\mathbf{F}, \mathbf{F}_\mathrm{p}), \qquad \mathbf{F}_\mathrm{p} \leftarrow \mathbf{F}_\mathrm{p} + \Delta\mathbf{F}_\mathrm{p},$$

until the local stopping criteria are met (e.g. $\|\mathbf{H}\| < \epsilon_{\mathrm{loc,abs}}$ and $\|\Delta\mathbf{F}_\mathrm{p}\| < \epsilon_{\mathrm{loc,rel}}$). For the detail implementation of the local constitutive solve, please see Algorithm 4.

Finally, the converged $\mathbf{F}_\mathrm{p}^\star$ is then used to compute the stress $\mathbf{P}(\mathbf{F}, \mathbf{F}_\mathrm{p}^\star)$ for the residual of force balance and, via the blocks $\mathbb{H}_\mathrm{e}$ and $\mathbb{H}_\mathrm{p}$, the algorithmic tangent $\mathbb{A}_\mathrm{alg}$ through the Schur complement Eq. (31). For the detail implementation to compute $\mathbb{A}_\mathrm{alg}$, please see Algorithm 5.

Algorithm 3: Residual evaluation

Input: t_n, $\mathbf{u}_h$, Δt, $\mathbf{F}_\mathrm{p}(t_{n-1})$
Output: $\mathbf{r}(\mathbf{u}_h)$ and iterated plastic deformation tensor $\mathbf{F}_\mathrm{p}^\star$
Function `Residual` $(t_n, \mathbf{u}_h, \Delta t, \mathbf{F}_\mathrm{p}(t_{n-1}))$**:**
  $\mathbf{r} \leftarrow \mathbf{0}$
  for *each cell* c *and each integration point* g *of* c **do**
    $\mathbf{F} \leftarrow \mathbf{I} + \nabla_0 \mathbf{u}_h|_{(c,g)}$
    $\mathbf{F}_\mathrm{p}^\star \leftarrow \mathtt{LocalPlasticSolve}(\mathbf{F}, \mathbf{F}_\mathrm{p}(t_{n-1}))$ `/* Solve Eq. (44), see Algorithm 4 */`
    `CacheFpIter` $(c, g, \mathbf{F}_\mathrm{p}^\star)$ `/* Store` $\mathbf{F}_\mathrm{p}^\star$ `for Jacobian at the same` $\mathbf{u}_h$`. */`
    $\mathbf{P} \leftarrow \mathtt{StressUpdate}(c, g, \mathbf{F}, \mathbf{F}_\mathrm{p}^\star)$
    for *each test dof* (i, α) *in* c **do**
      $\mathbf{r}_{i\alpha}$ += $w_g\Big(\mathbf{P} : (\nabla_0 \varphi_i \otimes \mathbf{e}_\alpha)\Big)$ `//` w_g `is the weight at` g`.`
  return r

Function `StressUpdate` $(c, g, \mathbf{F}, \mathbf{F}_\mathrm{p}^\star)$**:**
  $\mathbf{F}_\mathrm{e} \leftarrow \mathbf{F}(\mathbf{F}_\mathrm{p}^\star)^{-1}$; $\mathbf{C}_\mathrm{e} \leftarrow \mathbf{F}_\mathrm{e}^\mathsf{T}\mathbf{F}_\mathrm{e}$; $\mathbf{E}_\mathrm{e} \leftarrow \frac{1}{2}(\mathbf{C}_\mathrm{e} - \mathbf{I})$
  $\mathbf{S}_\mathrm{e} \leftarrow \mathbb{C}(c, g) : \mathbf{E}_\mathrm{e}$ `//` `Rotated elasticity tensor at` (c, g)`, see Eq. (6)`
  $\mathbf{P} \leftarrow \mathbf{F}_\mathrm{e}\,\mathbf{S}_\mathrm{e}\,(\mathbf{F}_\mathrm{p}^\star)^{-\mathsf{T}}$
  return P

Appendix B. Inverse pole figure coloring

The inverse pole figure coloring used in the polycrystalline tensile tests visualizes the local crystal orientation relative to the sample loading direction, here chosen as the y-axis. At each material point, the sample loading direction $\mathbf{e}_y$ is mapped into the crystal coordinate system as

$$\mathbf{n}_c = \mathbf{Q}^\mathsf{T}\mathbf{R}_0^\mathsf{T}\mathbf{e}_y,$$

where $\mathbf{e}_y$ is the Cartesian unit vector in the loading direction, $\mathbf{R}_0$ denotes the crystal orientation, and $\mathbf{Q}$ the lattice rotation. The vector $\mathbf{n}_c$ therefore represents the loading direction expressed in crystal coordinates. To obtain the IPF color, the direction $\mathbf{n}_c : V_0 \to \mathbb{R}^3$ is reduced by crystal symmetry to the fundamental region of the cubic crystal and projected onto the standard cubic IPF triangle, bounded by the $\langle 100\rangle$, $\langle 110\rangle$, and $\langle 111\rangle$ directions. The position of the projected point within this triangle determines the displayed color.

Data availability

Simulation data and videos for all results will be available on request. The source code for the CDD–CP simulation software realized in M++ is stored as a subproject under https://gitlab.kit.edu/kit/mpp. Access rights may also be granted upon reasonable request.

Algorithm 4: Local implicit iteration for $\mathbf{F}_\mathrm{p}^\star$ under given $\mathbf{F}$

Input: $\mathbf{F}$, $\mathbb{C}$, $\mathbf{F}_\mathrm{p}(t_{n-1})$, $\triangle t$, scheme $\in \{\mathrm{BE}, \mathrm{EXP}\}$; tolerances $(\epsilon_{\mathrm{loc,abs}}, \epsilon_{\mathrm{loc,rel}})$; $k_{\mathrm{loc,max}}$
Output: $\mathbf{F}_\mathrm{p}^\star$

Function `LocalPlasticSolve`$(\mathbf{F},\ \mathbf{F}_\mathrm{p}(t_{n-1}))$**:**

- $\mathbf{F}_\mathrm{p} \leftarrow \mathbf{F}_\mathrm{p}(t_{n-1})$
- **for** $k_\mathrm{loc} \leftarrow 0$ **to** $k_{\mathrm{loc,max}}$ **do**
  - $\mathbf{F}_\mathrm{e} \leftarrow \mathbf{F}\,\mathbf{F}_\mathrm{p}^{-1}$; $\mathbf{C}_\mathrm{e} \leftarrow \mathbf{F}_\mathrm{e}^\top \mathbf{F}_\mathrm{e}$; $\mathbf{S}_\mathrm{e} \leftarrow \mathbb{C}(c,g) : \frac{1}{2}(\mathbf{C}_\mathrm{e} - \mathbf{I})$
  - $\{\eta^s\}_{s\in S'} \leftarrow$ `ComputeViscosity`$(\mathbf{S}_\mathrm{e})$
  - $\mathbb{G} \leftarrow \sum_s \frac{1}{\eta^s}\mathbf{M}^s \otimes \mathbf{M}^s$
  - $\mathbf{L}_\mathrm{p} \leftarrow \mathbb{G} : \mathbf{S}_\mathrm{e}$
  - `/* Evaluate the local residual` $\mathbf{H}$`. */`
  - **if** scheme = BE **then** $\mathbf{H} \leftarrow \mathbf{F}_\mathrm{p} - (\mathbf{I} - \triangle t\,\mathbf{L}_\mathrm{p})^{-1}\mathbf{F}_\mathrm{p}(t_{n-1})$ `// See Eq. (45).`
  - **else if** scheme = EXP **then** $\mathbf{H} \leftarrow \mathbf{F}_\mathrm{p} - \exp(\triangle t\,\mathbf{L}_\mathrm{p})\,\mathbf{F}_\mathrm{p}(t_{n-1})$ `// See Eq. (47).`
  - **if** $\|\mathbf{H}\| \le \epsilon_{\mathrm{loc,abs}} + \epsilon_{\mathrm{loc,rel}}(\|\mathbf{F}_\mathrm{p}\| + 1)$ **then**
    - **if** scheme = BE **then**
      - $\mathbf{F}_\mathrm{p} \leftarrow \mathbf{F}_\mathrm{p} \leftarrow \mathbf{F}_\mathrm{p}/(\det \mathbf{F}_\mathrm{p})^{1/3}$
    - **return** $\mathbf{F}_\mathrm{p}^\star = \mathbf{F}_\mathrm{p}$
  - `/* Begin local linear solve (`$\mathbb{H}_\mathrm{p}\ \triangle\mathbf{F}_\mathrm{p} = -\mathbf{H}$`, with fixed` $\mathbf{F}$`) */`
  - define $\boldsymbol{\Phi}_\mathrm{P}[\delta\mathbf{F}_\mathrm{p}] \leftarrow -\frac{1}{2}\left(\mathbf{F}_\mathrm{p}^{-\top}(\delta\mathbf{F}_\mathrm{p})^\top\mathbf{C}_\mathrm{e} + \mathbf{C}_\mathrm{e}\,\delta\mathbf{F}_\mathrm{p}\,\mathbf{F}_\mathrm{p}^{-1}\right)$ `// See Eq. (41).`
  - $\mathbb{K}_\mathrm{flow} \leftarrow \mathbb{G} : \mathbb{C}(c,g)$
  - define `TransportOperator`$[Z] \leftarrow \begin{cases} (\mathbf{I} - \triangle t\,\mathbf{L}_\mathrm{p})^{-1}Z, & \text{backward-Euler,} \\ \widetilde{\mathcal{E}}_{\mathbf{L}_\mathrm{p}}[Z] := \mathcal{E}_{\mathbf{L}_\mathrm{p}}[Z]\,e^{-\Delta t\,\mathbf{L}_\mathrm{p}}, & \text{exponential-map.} \end{cases}$
  - $\mathbb{H}_\mathrm{p}[\delta\mathbf{F}_\mathrm{p}] \leftarrow \delta\mathbf{F}_\mathrm{p} -$ `TransportOperator`$\left[\triangle t\,(\mathbb{K}_\mathrm{flow} : \boldsymbol{\Phi}_\mathrm{P}[\delta\mathbf{F}_\mathrm{p}])\right]\mathbf{F}_\mathrm{p}$ `/* See Eqs. (46b) and (48b). */`
  - $\triangle\mathbf{F}_\mathrm{p} \leftarrow$ `SolveLinear`$(\mathbb{H}_\mathrm{p}, -\mathbf{H})$;
  - $\mathbf{F}_\mathrm{p} \leftarrow \mathbf{F}_\mathrm{p} + \triangle\mathbf{F}_\mathrm{p}$
- **return** $\mathbf{F}_\mathrm{p}^\star = \mathbf{F}_\mathrm{p}$

Function `ComputeViscosity`$(\mathbf{S}_\mathrm{e})$**:**

- **for** *each slip system* s *in* S' **do**
  - $\tau^s \leftarrow \mathbf{S}_\mathrm{e} : \mathbf{M}^s + \tau_\mathrm{int}^s$;
  - $\chi^s \leftarrow \mathbb{1}_{|\tau^s| > \tau_\mathrm{y}^s}$;
  - $\eta^s \leftarrow \dfrac{(b^s)^2\rho^s}{B}\,\chi^s$
- **return** $\{\eta^s\}_{s\in S'}$

Algorithm 5: Jacobian evaluation

Input: time t_n, displacement field $\mathbf{u}_h$, time step $\triangle t$, cached plastic states $\mathbf{F}_\mathrm{p}^\star$
Output: global Jacobian $\mathbf{J}(\mathbf{u}_h)$
Function `Jacobian` $(t_n, \mathbf{u}_h, \triangle t, \mathbf{F}_\mathrm{p}^\star)$**:**

- $\mathbf{J} \leftarrow \mathbf{0}$
- **for** *each cell* c *and each integration point* g *of* c **do**
  - $\mathbf{F} \leftarrow \mathbf{I} + \nabla_0 \mathbf{u}_h\|_{(c,g)}$
  - /* Cach $\mathbf{F}_\mathrm{p}^\star$ from residual pass. */
  - $\mathbf{F}_\mathrm{p}^\star \leftarrow$ `FetchCachedFp`(c, g)
  - /* $\mathbb{A}_\mathrm{alg} = d\mathbf{P}/d\mathbf{F}$ (See Eq. (31).) */
  - $\mathbb{A}_\mathrm{alg} \leftarrow$ `LocalAlgorithmicTangent`$(c, g, \mathbf{F}, \mathbf{F}_\mathrm{p}^\star, \triangle t)$
  - **for** *each test dof* (π, α) *and trial dof* (j, β) *in* c **do**
    - $\mathbf{J}_{(i,\alpha),(j,\beta)} \mathrel{+}= w_g \left(\mathbb{A}_\mathrm{alg} : (\nabla_0 \varphi_j \otimes \mathbf{e}_\beta) \right) : (\nabla_0 \varphi_i \otimes \mathbf{e}_k)$
- **return** $\mathbf{J}$

Function `LocalAlgorithmicTangent` $(c, g, \mathbf{F}, \mathbf{F}_\mathrm{p}^\star, \triangle t)$**:**

- $\mathbf{F}_\mathrm{e} \leftarrow \mathbf{F}\,\mathbf{F}_\mathrm{p}^{\star -1}$; $\mathbf{C}_\mathrm{e} \leftarrow \mathbf{F}_\mathrm{e}^\top \mathbf{F}_\mathrm{e}$; $\mathbf{S}_\mathrm{e} \leftarrow \mathbb{C}(c, g) : \frac{1}{2}(\mathbf{C}_\mathrm{e} - \mathbf{I})$
- define $\boldsymbol{\Phi}_\mathrm{F}[\delta\mathbf{F}] := \frac{1}{2}\left(\mathbf{F}_\mathrm{p}^{\star -\top} \delta\mathbf{F}^\top \mathbf{F}_\mathrm{e} + \mathbf{F}_\mathrm{e}^\top \delta\mathbf{F}\, \mathbf{F}_\mathrm{p}^{\star -1}\right)$
  - // See Eq. (35).
- define $\boldsymbol{\Phi}_\mathrm{P}[\delta\mathbf{F}_\mathrm{p}^\star] := -\frac{1}{2}\left(\mathbf{F}_\mathrm{p}^{\star -\top} (\delta\mathbf{F}_\mathrm{p}^\star)^\top \mathbf{C}_\mathrm{e} + \mathbf{C}_\mathrm{e}\, \delta\mathbf{F}_\mathrm{p}^\star\, \mathbf{F}_\mathrm{p}^{\star -1}\right)$
  - // See Eq. (41).
- define $\mathbb{A}_\mathrm{e}[\delta\mathbf{F}] := \delta\mathbf{F}\, \mathbf{F}_\mathrm{p}^{\star -1} \mathbf{S}_\mathrm{e}\, \mathbf{F}_\mathrm{p}^{\star -\top} + \mathbf{F}_\mathrm{e}\, (\mathbb{C}(c, g) : \boldsymbol{\Phi}_\mathrm{F}[\delta\mathbf{F}])\, \mathbf{F}_\mathrm{p}^{\star -\top}$
  - // See Eq. (37).
- define $\mathbb{A}_\mathrm{p}[\delta\mathbf{F}_\mathrm{p}^\star] := -\mathbf{F}_\mathrm{e}\, \delta\mathbf{F}_\mathrm{p}^\star\, \mathbf{F}_\mathrm{p}^{\star -1}\, \mathbf{S}_\mathrm{e}\, \mathbf{F}_\mathrm{p}^{\star -\top} + \mathbf{F}_\mathrm{e}\, (\mathbb{C}(c, g) : \boldsymbol{\Phi}_\mathrm{P}[\delta\mathbf{F}_\mathrm{p}^\star])\, \mathbf{F}_\mathrm{p}^{\star -\top} - \mathbf{F}_\mathrm{e}\, \mathbf{S}_\mathrm{e}\, \mathbf{F}_\mathrm{p}^{\star -\top} (\delta\mathbf{F}_\mathrm{p}^\star)^\top\, \mathbf{F}_\mathrm{p}^{\star -\top}$
  - // See Eq. (43).
- $\{\eta^s\}_{s \in S'} \leftarrow$ `ComputeViscosity`$(\mathbf{S}_\mathrm{e})$
- $\mathbb{G} \leftarrow \sum_s \frac{1}{\eta^s}\, \mathbf{M}^s \otimes \mathbf{M}^s$
- $\mathbf{L}_\mathrm{p} \leftarrow \mathbb{G} : \mathbf{S}_\mathrm{e}$
- $\mathcal{K}(\boldsymbol{\Phi}) \leftarrow (\mathbb{G} : \mathbb{C}(c, g)) : \boldsymbol{\Phi}$
- $\mathtt{TransportOperator}[Z] \leftarrow \begin{cases} (I - \triangle t\, \mathbf{L}_\mathrm{p})^{-1}\, Z, & \text{backward-Euler,} \\ \widetilde{\mathcal{E}}_{\mathbf{L}_\mathrm{p}}[Z] := \mathcal{E}_{\mathbf{L}_\mathrm{p}}[Z]\, e^{-\alpha \mathbf{L}_\mathrm{p}}, & \text{exponential-map.} \end{cases}$
- /* See Eqs. (46a) and (48a). */
- define $\mathbb{H}_\mathrm{e}[\delta\mathbf{F}] := -\,\mathtt{TransportOperator}\left[\, \triangle t\, \mathcal{K}(\boldsymbol{\Phi}_\mathrm{F}[\delta\mathbf{F}])\right] \mathbf{F}_\mathrm{p}^\star$
- /* See Eqs. (46b) and (48b). */
- define $\mathbb{H}_\mathrm{p}[\delta\mathbf{F}_\mathrm{p}^\star] := \delta\mathbf{F}_\mathrm{p}^\star - \mathtt{TransportOperator}\left[\, \triangle t\, \mathcal{K}(\boldsymbol{\Phi}_\mathrm{P}[\delta\mathbf{F}_\mathrm{p}^\star])\right] \mathbf{F}_\mathrm{p}^\star$
- $\mathbb{K} \leftarrow$ `SolveLocalLinear`$(\mathbb{H}_\mathrm{p}, \mathbb{H}_\mathrm{e})$
- $\mathbb{A}_\mathrm{alg} \leftarrow \mathbb{A}_\mathrm{e} - \mathbb{A}_\mathrm{p}\, \mathbb{K}$
- **return** $\mathbb{A}_\mathrm{alg}$

References

[1] H. Mughrabi, Dislocation wall and cell structures and long-range internal stresses in deformed metal crystals, Acta Metall. 31 (9) (1983) 1367–1379, http://dx.doi.org/10.1016/0001-6160(83)90007-X, URL https://www.sciencedirect.com/science/article/pii/000161608390007X.

[2] N. Hansen, D. Kuhlmann-Wilsdorf, Low energy dislocation structures due to unidirectional deformation at low temperatures, Mater. Sci. Eng. 81 (1986) 141–161, http://dx.doi.org/10.1016/0025-5416(86)90258-2, URL https://www.sciencedirect.com/science/article/pii/0025541686902582.

[3] D.A. Hughes, N. Hansen, High angle boundaries formed by grain subdivision mechanisms, Acta Mater. 45 (9) (1997) 3871–3886, http://dx.doi.org/10.1016/S1359-6454(97)00027-X, URL https://www.sciencedirect.com/science/article/pii/S135964549700027X.

[4] H.-J. Bunge, Texture Analysis in Materials Science: Mathematical Methods, Elsevier, 2013.

[5] O. Kapetanou, V. Koutsos, E. Theotokoglou, D. Weygand, M. Zaiser, Statistical analysis and stochastic dislocation-based modeling of microplasticity, J. Mech. Behav. Mater. 24 (3–4) (2015) 105–113, http://dx.doi.org/10.1515/jmbm-2015-0012.

[6] B. Katzer, K. Zoller, D. Weygand, K. Schulz, Identification of dislocation reaction kinetics in complex dislocation networks for continuum modelling using data-driven methods, J. Mech. Phys. Solids 168 (2022) 105042, http://dx.doi.org/10.1016/j.jmps.2022.105042, URL https://www.sciencedirect.com/science/article/pii/S0022509622002216.

[7] P. Cao, Maximum strength and dislocation patterning in multi–principal element alloys, Sci. Adv. 8 (45) (2022) eabq7433, http://dx.doi.org/10.1126/sciadv.abq7433, URL https://www.science.org/doi/abs/10.1126/sciadv.abq7433.

[8] R.J. Asaro, Crystal plasticity, J. Appl. Mech. (ISSN: 0021-8936) 50 (4b) (1983) 921–934, http://dx.doi.org/10.1115/1.3167205.

[9] D. Peirce, R.J. Asaro, A. Needleman, Material rate dependence and localized deformation in crystalline solids, Acta Metall. (ISSN: 0001-6160) 31 (12) (1983) 1951–1976, http://dx.doi.org/10.1016/0001-6160(83)90014-7, URL https://www.sciencedirect.com/science/article/pii/0001616083900147.

[10] S. Kalidindi, C. Bronkhorst, L. Anand, Crystallographic texture evolution in bulk deformation processing of FCC metals, J. Mech. Phys. Solids (ISSN: 0022-5096) 40 (3) (1992) 537–569, http://dx.doi.org/10.1016/0022-5096(92)80003-9, URL https://www.sciencedirect.com/science/article/pii/0022509692800039.

[11] F. Roters, M. Diehl, P. Shanthraj, P. Eisenlohr, C. Reuber, S. Wong, T. Maiti, A. Ebrahimi, T. Hochrainer, H.-O. Fabritius, S. Nikolov, M. Friák, N. Fujita, N. Grilli, K. Janssens, N. Jia, P. Kok, D. Ma, F. Meier, E. Werner, M. Stricker, D. Weygand, D. Raabe, DAMASK – the Düsseldorf advanced material simulation kit for modeling multi-physics crystal plasticity, thermal, and damage phenomena from the single crystal up to the component scale, Comput. Mater. Sci. (ISSN: 0927-0256) 158 (2019) 420–478, http://dx.doi.org/10.1016/j.commatsci.2018.04.030, URL https://www.sciencedirect.com/science/article/pii/S0927025618302714.

[12] U. Kocks, H. Mecking, Physics and phenomenology of strain hardening: the FCC case, Prog. Mater. Sci. (ISSN: 0079-6425) 48 (3) (2003) 171–273, http://dx.doi.org/10.1016/S0079-6425(02)00003-8, URL https://www.sciencedirect.com/science/article/pii/S0079642502000038.

[13] A. Arsenlis, D.M. Parks, Modeling the evolution of crystallographic dislocation density in crystal plasticity, J. Mech. Phys. Solids (ISSN: 0022-5096) 50 (9) (2002) 1979–2009, http://dx.doi.org/10.1016/S0022-5096(01)00134-X, URL https://www.sciencedirect.com/science/article/pii/S002250960100134X.

[14] A. Patra, S. Chaudhary, N. Pai, T. Ramgopal, S. Khandelwal, A. Rao, D.L. McDowell, ρ-CP: Open source dislocation density based crystal plasticity framework for simulating temperature-and strain rate-dependent deformation, Comput. Mater. Sci. (ISSN: 0927-0256) 224 (2023) 112182, http://dx.doi.org/10.1016/j.commatsci.2023.112182, URL https://www.sciencedirect.com/science/article/pii/S0927025623001763.

[15] J. Cappola, J. Wang, L. Li, A dislocation-density-based crystal plasticity model for FCC nanocrystalline metals incorporating thermally-activated depinning from grain boundaries, Int. J. Plast. (ISSN: 0749-6419) 172 (2024) 103863, http://dx.doi.org/10.1016/j.ijplas.2023.103863, URL https://www.sciencedirect.com/science/article/pii/S0749641923003479.

[16] D.J. Luscher, J.R. Mayeur, H.M. Mourad, A. Hunter, M.A. Kenamond, Coupling continuum dislocation transport with crystal plasticity for application to shock loading conditions, Int. J. Plast. (ISSN: 0749-6419) 76 (2016) 111–129, http://dx.doi.org/10.1016/j.ijplas.2015.07.007, URL https://www.sciencedirect.com/science/article/pii/S0749641915001254.

[17] M. Sudmanns, M. Stricker, D. Weygand, T. Hochrainer, K. Schulz, Dislocation multiplication by cross-slip and glissile reaction in a dislocation based continuum formulation of crystal plasticity, J. Mech. Phys. Solids (ISSN: 0022-5096) 132 (2019) 103695, http://dx.doi.org/10.1016/j.jmps.2019.103695, URL https://www.sciencedirect.com/science/article/pii/S0022509619306428.

[18] J.F. Nye, Some geometrical relations in dislocated crystals, Acta Metall. (ISSN: 0001-6160) 1 (2) (1953) 153–162, http://dx.doi.org/10.1016/0001-6160(53)90054-6, URL https://www.sciencedirect.com/science/article/pii/0001616053900546.

[19] E. Kröner, Kontinuumstheorie der versetzungen und eigenspannungen, 1958, http://dx.doi.org/10.1007/978-3-642-94719-3.

[20] A. Acharya, A model of crystal plasticity based on the theory of continuously distributed dislocations, J. Mech. Phys. Solids (ISSN: 0022-5096) 49 (4) (2001) 761–784, http://dx.doi.org/10.1016/S0022-5096(00)00060-0, URL https://www.sciencedirect.com/science/article/pii/S0022509600000600.

[21] A. Acharya, Constitutive analysis of finite deformation field dislocation mechanics, J. Mech. Phys. Solids (ISSN: 0022-5096) 52 (2) (2004) 301–316, http://dx.doi.org/10.1016/S0022-5096(03)00093-0, URL https://www.sciencedirect.com/science/article/pii/S0022509603000930.

[22] R. Arora, A. Acharya, Dislocation pattern formation in finite deformation crystal plasticity, Int. J. Solids Struct. (ISSN: 0020-7683) 184 (2020) 114–135, http://dx.doi.org/10.1016/j.ijsolstr.2019.02.013, URL https://www.sciencedirect.com/science/article/pii/S0020768319300927. Physics and Mechanics of Random Structures: From Morphology to Material Properties.

[23] I. Groma, Link between the microscopic and mesoscopic length-scale description of the collective behavior of dislocations, Phys. Rev. B 56 (1997) 5807–5813, http://dx.doi.org/10.1103/PhysRevB.56.5807, URL https://link.aps.org/doi/10.1103/PhysRevB.56.5807.

[24] I. Groma, F. Csikor, M. Zaiser, Spatial correlations and higher-order gradient terms in a continuum description of dislocation dynamics, Acta Mater. (ISSN: 1359-6454) 51 (5) (2003) 1271–1281, http://dx.doi.org/10.1016/S1359-6454(02)00517-7, URL https://www.sciencedirect.com/science/article/pii/S1359645402005177.

[25] M. Zaiser, T. Hochrainer, Some steps towards a continuum representation of 3D dislocation systems, Scr. Mater. (ISSN: 1359-6462) 54 (5) (2006) 717–721, http://dx.doi.org/10.1016/j.scriptamat.2005.10.060, URL https://www.sciencedirect.com/science/article/pii/S1359646205007049.

[26] A. El-Azab, Statistical mechanics treatment of the evolution of dislocation distributions in single crystals, Phys. Rev. B 61 (2000) 11956–11966, http://dx.doi.org/10.1103/PhysRevB.61.11956, URL https://link.aps.org/doi/10.1103/PhysRevB.61.11956.

[27] S. Xia, A. El-Azab, Computational modelling of mesoscale dislocation patterning and plastic deformation of single crystals, Modelling Simul. Mater. Sci. Eng. 23 (5) (2015) 055009, http://dx.doi.org/10.1088/0965-0393/23/5/055009.

[28] K. Starkey, A. El-Azab, Total Lagrange implementation of a finite-deformation continuum dislocation dynamics model of mesoscale plasticity, Int. J. Plast. (ISSN: 0749-6419) 155 (2022) 103332, http://dx.doi.org/10.1016/j.ijplas.2022.103332, URL https://www.sciencedirect.com/science/article/pii/S0749641922001139.

[29] T. Hochrainer, M. Zaiser, P. Gumbsch, A three-dimensional continuum theory of dislocation systems: kinematics and mean-field formulation, Phil. Mag. 87 (8–9) (2007) 1261–1282, http://dx.doi.org/10.1080/14786430600930218.

[30] T. Hochrainer, S. Sandfeld, M. Zaiser, P. Gumbsch, Continuum dislocation dynamics: Towards a physical theory of crystal plasticity, J. Mech. Phys. Solids (ISSN: 0022-5096) 63 (2014) 167–178, http://dx.doi.org/10.1016/j.jmps.2013.09.012, URL https://www.sciencedirect.com/science/article/pii/S0022509613001877.

[31] T. Hochrainer, Multipole expansion of continuum dislocations dynamics in terms of alignment tensors, Phil. Mag. 95 (12) (2015) 1321–1367, http://dx.doi.org/10.1080/14786435.2015.1026297.

[32] T. Hochrainer, Thermodynamically consistent continuum dislocation dynamics, J. Mech. Phys. Solids (ISSN: 0022-5096) 88 (2016) 12–22, http://dx.doi.org/10.1016/j.jmps.2015.12.015, URL https://www.sciencedirect.com/science/article/pii/S002250961530048X.

[33] M. Monavari, M. Zaiser, Annihilation and sources in continuum dislocation dynamics, Mater. Theory 2 (1) (2018) 3, http://dx.doi.org/10.1186/s41313-018-0010-z.

[34] C. Reuber, P. Eisenlohr, F. Roters, D. Raabe, Dislocation density distribution around an indent in single-crystalline nickel: Comparing nonlocal crystal plasticity finite-element predictions with experiments, Acta Mater. (ISSN: 1359-6454) 71 (2014) 333–348, http://dx.doi.org/10.1016/j.actamat.2014.03.012, URL https://www.sciencedirect.com/science/article/pii/S1359645414001591.

[35] S. Sandfeld, E. Thawinan, C. Wieners, A link between microstructure evolution and macroscopic response in elasto-plasticity: Formulation and numerical approximation of the higher-dimensional continuum dislocation dynamics theory, Int. J. Plast. (ISSN: 0749-6419) 72 (2015) 1–20, http://dx.doi.org/10.1016/j.ijplas.2015.05.001, URL https://www.sciencedirect.com/science/article/pii/S0749641915000704.

[36] K. Schulz, L. Wagner, C. Wieners, A mesoscale continuum approach of dislocation dynamics and the approximation by a Runge-Kutta discontinuous Galerkin method, Int. J. Plast. (ISSN: 0749-6419) 120 (2019) 248–261, http://dx.doi.org/10.1016/j.ijplas.2019.05.003, URL https://www.sciencedirect.com/science/article/pii/S0749641919301688.

[37] X. Luo, M. Zaiser, A computationally efficient implementation of continuum dislocation dynamics: Formulation and application to ultrafine-grained Mg polycrystals, J. Mech. Phys. Solids (ISSN: 0022-5096) 172 (2023) 105166, http://dx.doi.org/10.1016/j.jmps.2022.105166, URL https://www.sciencedirect.com/science/article/pii/S0022509622003428.

[38] C. Wieners, D. Corallo, D. Schneiderhan, L. Stengel, H.D.N. Pham, N. Baumgarten, MPP 3.6.0, 2026, Software release, version 3.6.0.

[39] N. Baumgarten, C. Wieners, The parallel finite element system M++ with integrated multilevel preconditioning and multilevel Monte Carlo methods, Comput. Math. Appl. (ISSN: 0898-1221) 81 (2021) 391–406, http://dx.doi.org/10.1016/j.camwa.2020.03.004, 4189816.

[40] N. Baumgarten, A Fully Parallelized and Budgeted Multi-level Monte Carlo Framework for Partial Differential Equations: From Mathematical Theory to Automated Large-Scale Computations (Ph.D. thesis), Dissertation, Karlsruhe, Karlsruher Institut für Technologie (KIT), 2023.

[41] N. Baumgarten, S. Krumscheid, C. Wieners, A fully parallelized and budgeted multilevel Monte Carlo method and the application to acoustic waves, SIAM/ASA J. Uncertain. Quantif. 12 (3) (2024) 901–931, http://dx.doi.org/10.1137/23M1588354.

[42] N. Baumgarten, D. Schneiderhan, Multilevel stochastic gradient descent for optimal control under uncertainty, 2025, URL https://arxiv.org/abs/2506.02647.

[43] N. Baumgarten, R. Kutri, R. Scheichl, A budgeted multi-level Monte Carlo method for full field estimates of multi-PDE problems, 2025, URL https://arxiv.org/abs/2506.01644.

[44] A. Ibrahimbegovic, Nonlinear Solid Mechanics: Theoretical Formulations and Finite Element Solution Methods, vol. 160, Springer Science & Business Media, 2009.

[45] E.H. Lee, Elastic-plastic deformation at finite strains, J. Appl. Mech. (ISSN: 0021-8936) 36 (1) (1969) 1–6, http://dx.doi.org/10.1115/1.3564580, arXiv:https://asmedigitalcollection.asme.org/appliedmechanics/article-pdf/36/1/1/5449476/1_1.pdf.

[46] F. Roters, P. Eisenlohr, T.R. Bieler, D. Raabe, Crystal Plasticity Finite Element Methods: in Materials Science and Engineering, vol. 1, Wiley Online Library, 2010.

[47] J. Bonet, R.D. Wood, Nonlinear Continuum Mechanics for Finite Element Analysis, Cambridge University Press, 1997.

[48] J.F. Nye, Physical Properties of Crystals: Their Representation by Tensors and Matrices, Clarendon Press, Oxford, 1957.

[49] J. Diebel, et al., Representing attitude: Euler angles, unit quaternions, and rotation vectors, Matrix 58 (15–16) (2006) 1–35.

[50] R.M. Brannon, Rotation, Reflection, and Frame Changes: Orthogonal Tensors in Computational Engineering Mechanics, IOP Publishing, 2018.

[51] E.A. de Souza Neto, D. Perić, D.R.J. Owen, Computational Methods for Plasticity: Theory and Applications, John Wiley & Sons, Chichester, 2008, http://dx.doi.org/10.1002/9780470694626, ISBN 978-0-470-06098-3.

[52] L.P. Kubin, G. Canova, M. Condat, B. Devincre, V. Pontikis, Y. Bréchet, Dislocation microstructures and plastic flow: a 3D simulation, Solid State Phenom. 23 (1992) 455–472.

[53] S. Sandfeld, M. Monavari, M. Zaiser, From systems of discrete dislocations to a continuous field description: stresses and averaging aspects, Modelling Simul. Mater. Sci. Eng. 21 (8) (2013) 085006, http://dx.doi.org/10.1088/0965-0393/21/8/085006.

[54] S. Schmitt, P. Gumbsch, K. Schulz, Internal stresses in a homogenized representation of dislocation microstructures, J. Mech. Phys. Solids (ISSN: 0022-5096) 84 (2015) 528–544, http://dx.doi.org/10.1016/j.jmps.2015.08.012, URL https://www.sciencedirect.com/science/article/pii/S0022509615300946.

[55] S.-H. Lee, K. Schulz, A data-based derivation of the internal stress in the discrete-continuum transition regime of dislocation based plasticity, Int. J. Plast. (ISSN: 0749-6419) 170 (2023) 103771, http://dx.doi.org/10.1016/j.ijplas.2023.103771, URL https://www.sciencedirect.com/science/article/pii/S0749641923002553.

[56] G.I. Taylor, The mechanism of plastic deformation of crystals. Part I.—Theoretical, Proc. R. Soc. Lond. A (ISSN: 0950-1207) 145 (855) (1934) 362–387, http://dx.doi.org/10.1098/rspa.1934.0106.

[57] L. Wagner, A Discontinuous Galerkin Method for Continuum Dislocation Dynamics in a Fully-Coupled Elastoplasticity Model (Ph.D. thesis), Dissertation, Karlsruhe, Karlsruher Institut für Technologie (KIT), 2019.

[58] X. Zhang, J. Xiong, H. Fan, M. Zaiser, Microplasticity and yielding in crystals with heterogeneous dislocation distribution, Modelling Simul. Mater. Sci. Eng. 27 (7) (2019) 074003, http://dx.doi.org/10.1088/1361-651X/ab2851.

[59] K. Zoller, K. Schulz, Analysis of single crystalline microwires under torsion using a dislocation-based continuum formulation, Acta Mater. (ISSN: 1359-6454) 191 (2020) 198–210, http://dx.doi.org/10.1016/j.actamat.2020.03.057, URL https://www.sciencedirect.com/science/article/pii/S1359645420302548.

[60] M. Sudmanns, J. Bach, D. Weygand, K. Schulz, Data-driven exploration and continuum modeling of dislocation networks, Modelling Simul. Mater. Sci. Eng. 28 (6) (2020) 065001, http://dx.doi.org/10.1088/1361-651X/ab97ef.

[61] V. Vivekanandan, B. Anglin, A. El-Azab, A data driven approach for cross-slip modelling in continuum dislocation dynamics, Int. J. Plast. (ISSN: 0749-6419) 164 (2023) 103597, http://dx.doi.org/10.1016/j.ijplas.2023.103597, URL https://www.sciencedirect.com/science/article/pii/S0749641923000839.

[62] J.C. Simo, T.J.R. Hughes, Computational Inelasticity, Interdisciplinary Applied Mathematics, vol. 7, Springer, New York, ISBN: 978-0-387-98490-2, 1998, http://dx.doi.org/10.1007/978-1-4612-1186-6.

[63] Y. Saad, M.H. Schultz, GMRES: A generalized minimal residual algorithm for solving nonsymmetric linear systems, SIAM J. Sci. Stat. Comput. 7 (3) (1986) 856–869, http://dx.doi.org/10.1137/0907058.

[64] S.-H. Lee, C. Wieners, K. Schulz, Continuum modeling of dislocation microstructures under tribological loading, Tribol. Int. (ISSN: 0301-679X) 209 (2025) 110731, http://dx.doi.org/10.1016/j.triboint.2025.110731, URL https://www.sciencedirect.com/science/article/pii/S0301679X25002269.

[65] J.S. Hesthaven, T. Warburton, Nodal Discontinuous Galerkin Methods: Algorithms, Analysis, and Applications, Springer, 2008.

[66] S. Sandfeld, M. Zaiser, Pattern formation in a minimal model of continuum dislocation plasticity, Modelling Simul. Mater. Sci. Eng. 23 (6) (2015) 065005, http://dx.doi.org/10.1088/0965-0393/23/6/065005.

[67] H.M. Ledbetter, E.R. Naimon, Elastic properties of metals and alloys. II. Copper, J. Phys. Chem. Ref. Data 3 (4) (1974) 897–935, http://dx.doi.org/10.1063/1.3253150.

[68] E.H.F. Date, K.W. Andrews, Anisotropic and composition effects in the elastic properties of polycrystalline metals, J. Phys. D: Appl. Phys. 2 (10) (1969) 1373, http://dx.doi.org/10.1088/0022-3727/2/10/303.

[69] L. Kubin, B. Devincre, T. Hoc, Modeling dislocation storage rates and mean free paths in face-centered cubic crystals, Acta Mater. (ISSN: 1359-6454) 56 (20) (2008) 6040–6049, http://dx.doi.org/10.1016/j.actamat.2008.08.012, URL https://www.sciencedirect.com/science/article/pii/S1359645408005788.

[70] W.P. Davey, Precision measurements of the lattice constants of twelve common metals, Phys. Rev. 25 (1925) 753–761, http://dx.doi.org/10.1103/PhysRev.25.753, URL https://link.aps.org/doi/10.1103/PhysRev.25.753.

[71] R. Wu, D. Tüzes, P.D. Ispánovity, I. Groma, T. Hochrainer, M. Zaiser, Instability of dislocation fluxes in a single slip: Deterministic and stochastic models of dislocation patterning, Phys. Rev. B 98 (2018) 054110, http://dx.doi.org/10.1103/PhysRevB.98.054110, URL https://link.aps.org/doi/10.1103/PhysRevB.98.054110.

[72] R. Wu, M. Zaiser, Cell structure formation in a two-dimensional density-based dislocation dynamics model, Mater. Theory 5 (1) (2021) 3, http://dx.doi.org/10.1186/s41313-020-00025-x.

[73] P. Lin, A. El-Azab, Implementation of annihilation and junction reactions in vector density-based continuum dislocation dynamics, Modelling Simul. Mater. Sci. Eng. 28 (4) (2020) 045003, http://dx.doi.org/10.1088/1361-651X/ab7d90.

[74] N. Grilli, K.G.F. Janssens, H. Van Swygenhoven, Crystal plasticity finite element modelling of low cycle fatigue in fcc metals, J. Mech. Phys. Solids (ISSN: 0022-5096) 84 (2015) 424–435, http://dx.doi.org/10.1016/j.jmps.2015.08.007, URL https://www.sciencedirect.com/science/article/pii/S0022509615300727.

[75] N. Grilli, K.G.F. Janssens, J. Nellessen, S. Sandlöbes, D. Raabe, Multiple slip dislocation patterning in a dislocation-based crystal plasticity finite element method, Int. J. Plast. (ISSN: 0749-6419) 100 (2018) 104–121, http://dx.doi.org/10.1016/j.ijplas.2017.09.015, URL https://www.sciencedirect.com/science/article/pii/S0749641917305570.

[76] C.A. Bronkhorst, S.R. Kalidindi, L. Anand, Polycrystalline plasticity and the evolution of crystallographic texture in FCC metals, Philos. Trans. R. Soc. Lond. A (ISSN: 0962-8428) 341 (1662) (1992) 443–477, http://dx.doi.org/10.1098/rsta.1992.0111.

[77] C. Miehe, J. Schröder, J. Schotte, Computational homogenization analysis in finite plasticity simulation of texture development in polycrystalline materials, Comput. Methods Appl. Mech. Engrg. (ISSN: 0045-7825) 171 (3) (1999) 387–418, http://dx.doi.org/10.1016/S0045-7825(98)00218-7, URL https://www.sciencedirect.com/science/article/pii/S0045782598002187.

[78] C. Miehe, Numerical computation of algorithmic (consistent) tangent moduli in large-strain computational inelasticity, Comput. Methods Appl. Mech. Engrg. (ISSN: 0045-7825) 134 (3) (1996) 223–240, http://dx.doi.org/10.1016/0045-7825(96)01019-5, URL https://www.sciencedirect.com/science/article/pii/0045782596010195.

[79] E.A. de Souza Neto, The exact derivative of the exponential of an unsymmetric tensor, Comput. Methods Appl. Mech. Engrg. (ISSN: 0045-7825) 190 (18) (2001) 2377–2383, http://dx.doi.org/10.1016/S0045-7825(00)00241-3, URL https://www.sciencedirect.com/science/article/pii/S0045782500002413.

[80] A.H. Al-Mohy, N.J. Higham, Computing the Fréchet derivative of the matrix exponential, with an application to condition number estimation, SIAM J. Matrix Anal. Appl. 30 (4) (2009) 1639–1657, http://dx.doi.org/10.1137/080716426.